

Control of spiral wave dynamics in active media

vorgelegt von
Diplom-Physiker
Jan Schlesner
aus Köln

von der Fakultät II – Mathematik und Naturwissenschaften
der Technischen Universität Berlin
zur Erlangung des akademischen Grades
Doktor der Naturwissenschaften
– Dr. rer. nat. –
genehmigte Dissertation

Promotionsausschuss:

Vorsitzender: Prof. Dr. D. Breitschwerdt
Berichter/Gutachter: Prof. Dr. H. Engel
Berichter/Gutachter: Prof. Dr. L. Schimansky–Geier

Tag der wissenschaftlichen Aussprache: 28.11.2014

Berlin 2015
D 83

Zusammenfassung

Gegenstand der vorliegenden Dissertation ist die Dynamik und die Kontrolle von Spiralwellen in erregbaren Medien, wobei hier zwischen externen Störungen und rückkoppelungs-gesteuerter Kontrolle unterschieden werden muss.

Als Kontrolle mit externen Störungen wurden laufende Erregungswellen verwendet. Es wurde vorhergesagt, dass eine synchronisierte Driftbewegung des Spiralwellenzentrums innerhalb eines gewissen Frequenzbereichs der Erregungswellen stattfinden könnte. Dieses konnte im Rahmen dieser Arbeit anhand von Experimenten mit der lichtempfindlichen Belousov-Zhabotinsky-Reaktion (BZR) als auch mit Hilfe von numerischen Simulationen mit dem Oregonator- und dem FitzHugh-Nagumo-Modell bestätigt werden. Außerdem wurde gezeigt, dass dieses auch für mäandernde Spiralwellen gilt.

Als rückkoppelungs-gesteuerte Kontrollen wurden verschiedenen Methoden betrachtet. Zum einem wurde der Abstand der Spiralspitze zu einem festgelegten Punkt verwendet, um mit Hilfe proportionaler und zeitverzögerter Rückkopplung instabile periodische Orbits — in diesem Fall kreisförmig rotierende Spiralwellen — zu stabilisieren. Diese Verfahren können u.a. dazu dienen, Lösungen auf instabilen Bifurkationsästen zu stabilisieren und diese zu charakterisieren. Außerdem wurde im Rahmen dieser Arbeit die Robustheit dieser beiden Verfahren gegenüber Zeitverzögerungen in der Kontrollschleife, die in realen Systemen fast immer auftreten, untersucht.

Zum anderen konnte gezeigt werden, daß mit Hilfe eines rückkoppelungs-gesteuerten Kontrollverfahrens der Kern von Spiralwellen in einem zweidimensionalen Medium entlang eines eindimensionalen Detektors bewegt werden kann. Neben experimentellen und numerischen Untersuchungen wurde eine Theorie entwickelt, die die Beschreibung der Spiralwellenbewegung auf eine iterierte Abbildung für das Drift-Geschwindigkeits-Feld reduziert. Des Weiteren wurden Instabilitäten untersucht, die durch hohe Kontrollamplituden oder längere Verzögerungszeiten auftreten.

Bei der Untersuchung der einzelnen Kontrollverfahren wurden immer sowohl theoretische, numerische als auch experimentelle Resultate miteinander verglichen. Insbesondere zur experimentellen Untersuchung von raum-zeitlichen Kontrollen wurde hierfür ein neuer Versuchsaufbau für die licht-empfindliche BZR entwickelt.

Abstract

This thesis deals with the dynamics and control of spiral waves in active media. Regarding the control, we have to distinguish between external forcing and feedback-mediated control.

For control with external forcing, we used traveling wave modulation. Under traveling wave modulation, synchronized drift of the spiral wave core was predicted within a certain frequency range. We were able to verify this prediction with results from experiments with the light-sensitive Belousov-Zhabotinsky-Reaction (BZR) as well as with numerical results from simulations of the Oregonator and the FitzHugh-Nagumo-model. Additionally, we have shown that this is not only true for rigidly rotating but also for meandering spiral waves.

For feedback-mediated control we used different control methods. On the one hand we used the distance between the spiral wave tip and a chosen point to generate a control force, using proportional feedback control (PFC) and time delay autosynchronization (TDAS). With these methods we stabilized unstable periodic orbits (UPOs), specifically the unstable rigidly rotating movement of a spiral wave tip within the meandering regime. These methods can be used to stabilize unstable branches in the bifurcation tree and in so doing, identify the characteristics of unstable solutions. We also studied the robustness of both methods regarding the appearance of control loop latencies (CLL), since in almost every real control system control loop latencies can be found.

On the other hand, we present a feedback-mediated control method with which the spiral wave core in a two-dimensional medium can be moved along or parallel to a one-dimensional detector. Aside from our experimental and numerical studies, we elaborated a theory. In this theory, the movement of the spiral wave core can be described by an iterated map. Additionally, we investigated instabilities induced by high control amplitudes or longer control loop latencies.

In our studies of the different control methods, we always compared theoretical, numerical and experimental results and especially in our experimental studies of spatio-temporal control methods, we have a new experimental setup for the light-sensitive BZR.

Contents

1	Introduction	6
1.1	Dynamics and control of spiral waves	6
1.1.1	Spiral waves	6
1.1.2	Control of spiral waves	9
1.2	Structure of this thesis	10
2	Spiral waves in reaction–diffusion systems	12
2.1	The Oregonator model	13
2.2	The FitzHugh–Nagumo model	16
3	Simulation methods	18
3.1	Numerical methods to solve reaction diffusion–systems	18
3.1.1	Forward–Euler–Method	18
3.1.2	Spatial discretization and approximation of the diffusion	19
3.1.3	Boundary conditions	20
3.2	Initial conditions to generate spiral waves	21
3.3	Detection of the tip position	22
3.4	Co–moving simulation area	25
3.5	Simulation parameters	25
4	Experimental setup	27
4.1	The light–sensitive Belousov–Zhabotinsky reaction in an open gel reactor	27
4.2	Experimental setup for uniform applied light intensity	30
4.3	Experimental setup for space and time dependent applied light intensity	32
4.3.1	Visualization technique	33
4.3.2	Separation of the optical channels	34
4.3.3	Light sources	34

4.3.4	Experimental setup	36
5	Spiral wave dynamics under traveling wave modulation	40
5.1	Traveling wave modulation	40
5.2	Experimental observations	43
5.3	Numerical verification	45
6	Feedback-mediated stabilization of unstable rigid rotation	49
6.1	Proportional Feedback Control	50
6.1.1	PFC without control loop latency	50
6.1.2	PFC with control loop latency effects	57
6.2	Time Delay Autosynchronization	61
6.2.1	TDAS without control loop latencies	61
6.2.2	TDAS and control loop latency	65
6.3	Comparison of PFC and TDAS	66
7	Control of spiral wave location by detector-line feedback	68
7.1	Introduction to feedback-induced resonant drift of spiral waves	68
7.2	Theoretical description of spiral waves under detector-line feedback	70
7.2.1	Single-pulse feedback	71
7.2.2	Double-pulse feedback	83
7.3	Numerical simulation of spiral core drift in reaction-diffusion systems	86
7.3.1	Spiral core drift in the Oregonator model	87
7.3.2	Spiral core drift in the FHN model	91
7.4	Experimental observation of feedback induced drift	92
8	Summary	96
8.1	Control of spiral wave dynamics	96
8.1.1	External forcing by traveling wave modulation	96
8.1.2	Feedback-mediated control	97
8.2	Experimental setup	99
	Bibliography	101
	Acknowledgement	110

1 Introduction

1.1 Dynamics and control of spiral waves

1.1.1 Spiral waves

In general the presented work deals with the dynamics and control of spatio-temporal self-organization patterns, in particular of spiral waves, in non-equilibrium systems. Such a spiral wave is shown in Fig. 1.1, which is here a spiral wave in a light-sensitive Belousov-Zhabotinsky (BZ) medium in a petri dish.

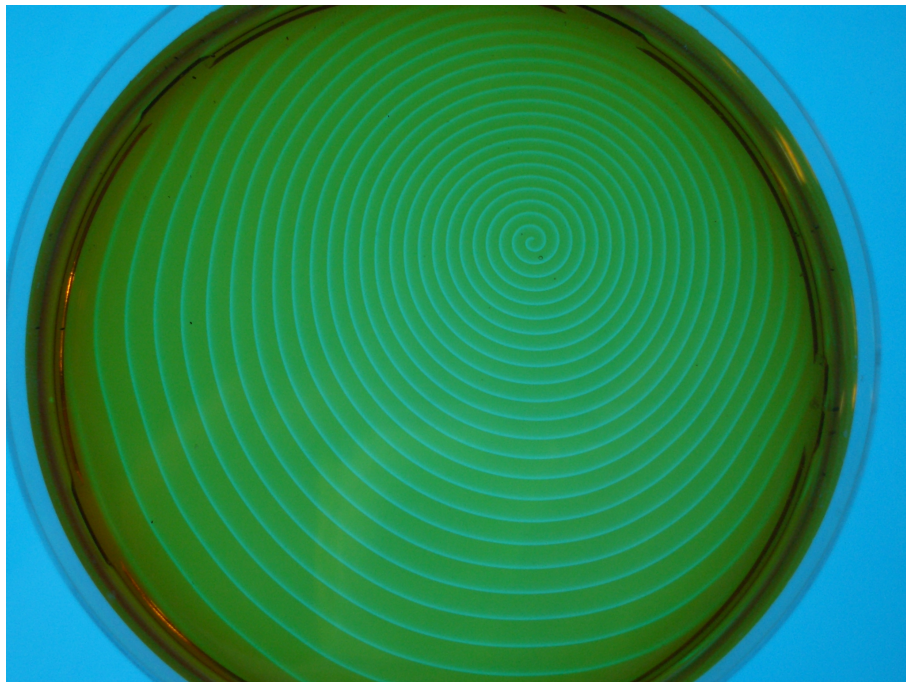


Figure 1.1: Spiral wave in a light-sensitive Belousov-Zhabotinsky medium in a petri dish. The brightness of the BZ medium is proportional to the concentration of the oxidized form of the catalyst.

The BZ reaction is the oxidation of an organic compound, like malonic acid, by bromide ions in a strongly acidic solution and in the presence of a catalyst (Zaikin & Zhabotinsky 1970, Winfree 1972, Zhabotinsky & Zaikin 1973). This reaction was the first oscillating reaction to be discovered. Before this discovery only reactions with exponential convergency to an equilibrium were known. Due to the fact that the BZ reaction is well-known and controllable, it is often used in experiments to observe pattern formation such as spiral waves.

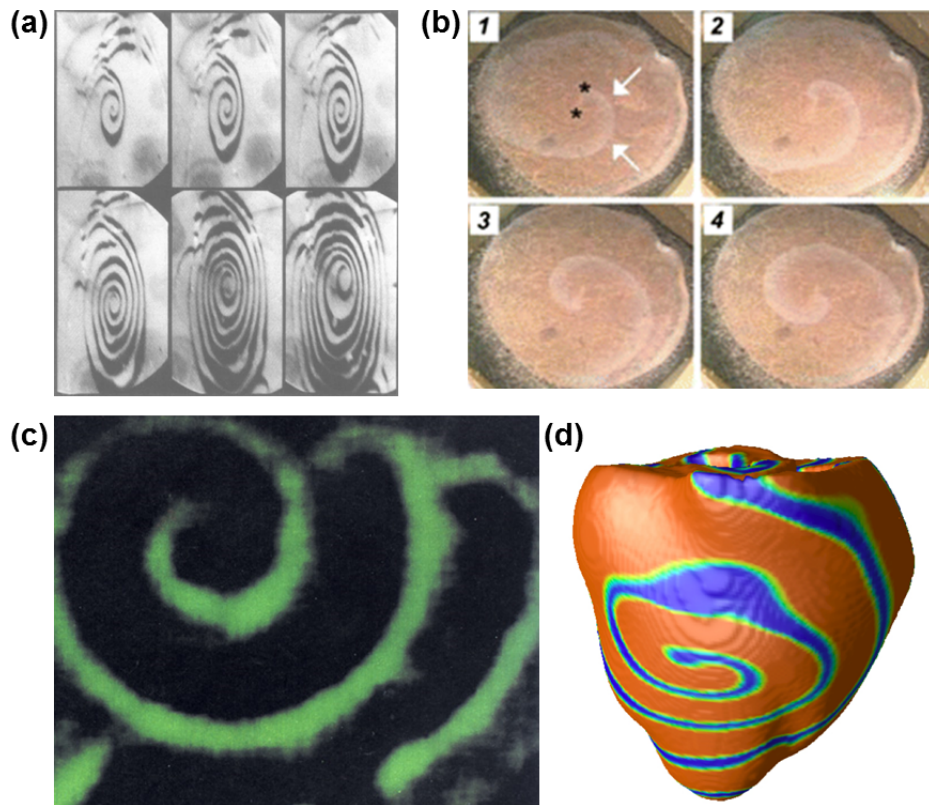


Figure 1.2: Examples of spiral waves in different systems: (a) catalytic surface reaction of carbon monoxide on platinum single crystal surface¹, (b) Spreading depression waves in ex vivo normoxic chicken retina², (c) Calcium waves in *Xenopus laevis* oocytes³, (d) Electrical potential waves in a computational model of rabbit ventricles⁴

Spiral waves represent common examples of spatio-temporal patterns, because they occur not only in the BZ medium but also in a huge number of very different systems (Kapral & Showalter 1995) such as in other chemical reactions (Mikhailov & Showalter 2006) like the catalytic surface reaction of carbon monoxide on a platinum single crystal surface (Jakubith, Rotermund, Engel, von Oertzen & Ertl 1990).

Along with many chemical reactions spiral waves can also be observed in different biological systems. In Fig. 1.2(b) chicken retinas are shown, where spiral waves can occur as waves of spreading depression of electrical activity. They were primarily observed around retinal obstacles (Martins-Ferreira, Castro, Struchiner & Rodrigues 1974) and later also in intact retinas of eyes (Gorelova & Bures 1983).

Another biological system, in which spiral waves appear, are aggregating cells in the slime mold *Dictyostelium discoideum* (Gerisch 1971, Siegert & Weijer 1989). These cells are attracted to each other chemotactically by cyclic adenosine monophosphate (cAMP) signals and can converge to form clusters of about 10^5 cells. In this case, spiral waves are observed optically in the aggregation field as dark-field waves. Spiral waves can even be found in frogs eggs. In *Xenopus laevis* oocytes spiral calcium waves can appear (Lechleiter, Girard, Peralta & Clapham 1991) as shown in Fig. 1.2(c).

One of the most prominent examples of spiral waves in nature are excitation spiral waves in cardiac muscles. The first time that the existence of spiral waves in heart tissue was proposed was in (McWilliam 1887) and later experimentally observed in rabbit atrial muscle (Allessie, Bonke & Schopman 1973). Spiral waves in cardiac muscles can cause arrhythmia such as ventricular tachycardia and fibrillation (Davidenko, Pertsov, Salomonsz, Baxter & Jalife 1992). Due to the fatal risk

¹Reprint from *Phys. Rev. Lett.* **65**(24), S. Jakubith, H. H. Rotermund, W. Engel, A. von Oertzen and G. Ertl, Spatiotemporal concentration patterns in a surface reaction: Propagating and standing waves, rotating spirals, and turbulence, 3013–3016, Copyright (1990), with permission from APS

²Reprint from *PNAS* **109**(7), Y. Yu, L. M. Santos, L. A. Mattiace, M. L. Costa, L. C. Ferreira, K. Benabou, A. H. Kim, J. Abrahams, M. V. L. Bennett, and R. Rozentall, Reentrant spiral waves of spreading depression cause macular degeneration in hypoglycemic chicken retina, 2585–2589, Copyright (2012) by National Academy of Sciences, USA, with permission from NAS

³Reprint from *Cell* **69**(2), J. D. Lechleiter and D. E. Clapham, Molecular mechanisms of intracellular calcium excitability in *X. laevis* oocytes, 283–294, Copyright (1992), with permission from Elsevier

⁴Reprint from *Projects in Scientific Computing*, F. Fenton and E. Cherry, New understanding of when we're at risk for ventricular fibrillation, Copyright (2003), with permission from PSC

associated with cardiac arrhythmia, the dynamics and control of spiral waves are of special interest.

Many results regarding spiral wave dynamics obtained in specific systems can be transferred qualitatively to other systems. Due to the manageability and homogeneity of chemical systems, they are often used to study the general behavior of waves, patterns and turbulences experimentally. A good overview of this is given in (Mikhailov & Showalter 2006).

This thesis is limited to 2-dimensional media and spiral waves. But 3-dimensional effects have become more and more important in recent years and have been studied in experiments with the BZ reaction e.g. scroll waves have been studied (Totz, Engel & Steinbock 2014, Nakouzi, Jiménez, Biktashev & Steinbock 2014, Jiménez & Steinbock 2012, Bánsági & Steinbock 2006, Vinson, Mironov, Mulvey & Pertsov 1997, Maselko & Showalter 1989).

1.1.2 Control of spiral waves

In discussing control methods one has to distinguish between external forcing and feedback-mediated control.

External forcing is characterized by the fact that the control force applied does not depend on the state of the observed system. One example for spatio-temporal external forcing is traveling wave modulation, which is able to significantly change pattern formation processes in different systems. The dynamics of Turing patterns under this modulation have been studied in (Rüdiger, Miguez, Munuzuri, Sagues & Casademunt 2003) and a theory of pattern-forming systems under traveling-wave modulation on the basis of generic amplitude equations was presented in (Rüdiger, Nicola, Casademunt & Kramer 2007). The behavior of spiral waves under traveling wave modulation has also been studied in (Zykov, Zykov & Davydov 2006, Ning-Jie, Jun, Jing-an & He-Ping 2008).

In feedback-mediated control a feedback signal is used to generate or to trigger the control force. Often the system can be regarded as a black box where only a small number of parameters are used to generate the control force (as in a real system the full state and dynamics of the system are not available). Feedback-mediated control can be split up further into invasive and non-invasive control methods. By applying invasive control methods the dynamics of the system are influenced in such a way

that the resulting state is not longer a solution of the unperturbed system. Invasive control methods are of high interest for controlling the motion of spiral waves. For example, the control of the motion of spiral waves induced by a modulation of medium excitability is important for many applications such as for the low-voltage defibrillation of cardiac tissue (Biktashev & Holden 1994, Panfilov, Müller, Zykov & Keener 2000, Christini & Glass 2002).

In contrast to invasive control methods, non-invasive control methods only have an impact on the stability of solutions and not on the solutions themselves. With non-invasive control methods unstable solutions can be stabilized. In this thesis proportional feedback control (PFC) and time delay autosynchronization were used to stabilize unstable periodic solutions (Schlesner, Zykov, Engel & Schöll 2006).

1.2 Structure of this thesis

Following this introductory chapter we present in Chapter Two and Three the numerical models and methods used in this thesis. For the numerical simulations we focused on reaction-diffusion systems, which are introduced in Chapter Two. Due to the fact that we performed our experiments with a light-sensitive version of the Belousov-Zhabotinsky reaction (BZR) we carried out the majority of our simulations with the Oregonator model, which is derived from the chemical reaction steps of the BZR under several assumptions and reductions. To verify the results obtained from our simulations with the Oregonator model we also performed simulations with a more general model, the FitzHugh-Nagumo (FHN) model (Winfree 1991, FitzHugh 1961, Nagumo, Arimoto & Yoshizawa. 1962). In Chapter Three we introduce the numerical methods such as the integration methods, the boundary conditions and the computational organization of the simulation area, its adaptation and the numerical parameters used to obtain the results in this thesis.

After the numerical techniques are presented, we discuss the experimental methods for the light-sensitive BZ reaction in Chapter Four. To get experimentally reproducible results we need experimental setups with controlled experimental conditions. For this thesis we performed experiments with two different experimental setups. The first one is a very commonly used experimental setup, which can be used to perform experiments with global control. This means that the control force is spa-

tially homogeneous. Most of the experiments presented in this thesis are performed with this experimental setup. Due to the fact that for some control mechanism it is necessary to change the light intensity spatio-temporally and that the existing experimental setups that can control the light intensity in this way have significant disadvantages, we have developed a new experimental setup. This setup is a powerful tool for studying pattern formation in light-sensitive chemical reactions, since a broad range of control methods can be applied to the two-dimensional gel layer.

To demonstrate the capacities of this experimental setup we performed experiments with a spatially non-homogeneous and time-dependent control method. The results obtained from experiments with the developed experimental setup by applying traveling wave modulation are demonstrated in Chapter Five.

In Chapter Six we investigate the stabilization of unstable rotation regimes of spiral waves. By varying a bifurcation parameter it is possible to move from one rotation regime to another one. We observe one bifurcation in particular, which is a Hopf-bifurcation. At the bifurcation point a rotation regime (called rigid rotation) becomes unstable but still exists. We stabilize this unstable solution by using different non-invasive control methods. and we demonstrate that these methods can be used to trace unstable branches of rotation regimes and determine their characteristics.

In Chapter Seven we focus on a feedback method which allows us to guide a spiral wave core through a two-dimensional medium along a virtual line-detector. We develop a theory that reduces the description of the spiral wave drift to an iterated map from which the drift velocity field of the motion of the spiral core can be obtained. This drift velocity field predicts both the transient as well as the stationary trajectories of the drifting spiral waves consistent with experimental and numerical results.

Finally in the last chapter we briefly summarize all of the methods developed in this thesis as well as the results obtained by their application.

2 Spiral waves in reaction–diffusion systems

The focus of this thesis is the control of spiral waves in excitable media, in particular in reaction–diffusion systems. This chapter gives an overview of the theoretical models used, all of which belong to the group ‘reaction–diffusion systems’. Since our experiments were performed with a light–sensitive version of the Belousov–Zhabotinsky reaction (BZR) we mainly accomplished simulations with the Oregonator model, which is derived from the chemical reaction–steps of the BZR. To verify and potentially generalize the results obtained, simulations with a more general model, the FitzHugh–Nagumo (FHN) model (Winfrey 1991, FitzHugh 1961, Nagumo et al. 1962), were performed as well.

After the introduction of each model, the dynamics of spiral waves and particularly the spiral wave tips within this model are presented. Bifurcation scenarios concerning the movement of spiral wave tips are shown, as the dynamics of a spiral wave are primarily determined by the dynamics of its tip. In this regard the different rotation regimes of spiral waves are introduced, which can be characterized by the trajectory described by the spiral tip (Jahnke, Skaggs & Winfree 1989, Li, Ouyang, Petrov & Swinney 1996). The simplest case is a periodic regime called rigid rotation with a tip moving along a circle. Rigidly rotating spiral waves have constant shape and rotate uniformly, but much more complicated regimes also exist. These regimes are introduced as soon as the bifurcation scenarios for the models have been presented.

2.1 The Oregonator model

The light-sensitive BZ medium is a prominent example of a medium in which propagation of spiral waves occurs. Many experimental studies devoted to the control of spiral wave dynamics have been performed within this system. Since we also use the BZR for our experiments, we accomplish simulations with the Oregonator model as well. For our numerical simulations we use the modified two-variable Oregonator model for the light-sensitive version of the BZ reaction given by the equations

$$\frac{\partial u}{\partial t} = \frac{1}{\epsilon} \left(u - u^2 - (fv + \phi) \frac{u - q}{u + q} \right) + D_u \Delta u, \quad (2.1)$$

$$\frac{\partial v}{\partial t} = u - v + D_v \Delta v. \quad (2.2)$$

Here, $u(x, y, t)$ and $v(x, y, t)$ represent the dimensionless concentrations of the activator bromous acid $HBrO_2$ and the oxidized form of the catalyst, respectively, q , f , and $\epsilon \ll 1$ are scaling parameters, and D_u and D_v denote the diffusion constants (Keener & Tyson 1986, Krug, Pohlmann & Kuhnert 1990). The photochemically induced bromide flow ϕ is assumed to be proportional to the applied light intensity. Below, ϕ is considered the main bifurcation parameter steering the transition to the different spiral wave rotating regimes.

Different parameters in the Oregonator model (2.1) and (2.2) result in different regimes such as rigidly rotating, meandering or hypermeandering spiral wave solutions (Jahnke & Winfree 1991, Kapral & Showalter 1995). For fixed values of q , f , ϵ , D_u , and D_v , the regime of rotation is uniquely defined by the parameter ϕ . The bifurcation scenario obtained under variation of ϕ for parameter set O1 (please refer to section 3.5 for the parameter sets used in this thesis) is shown in Figure 2.1. At $\phi = 0.035$ the spiral is in the simplest regime called rigid rotation. Under certain conditions a transition from one-frequency periodic to two-frequency quasi-periodic motions occurs where the spiral tip meanders rather than follows a circular orbit. Meandering spiral waves appear in two types called outward and inward meandering, depending on whether their tip trajectory forms a flower-like orbit with loops pointing outwards or inwards respectively. By increasing ϕ from $\phi = 0.035$, at $\phi = \phi_{cr1} \approx 0.047$ a supercritical Hopf bifurcation occurs and rigid rotation is replaced by outward meandering. When ϕ grows further, the regime

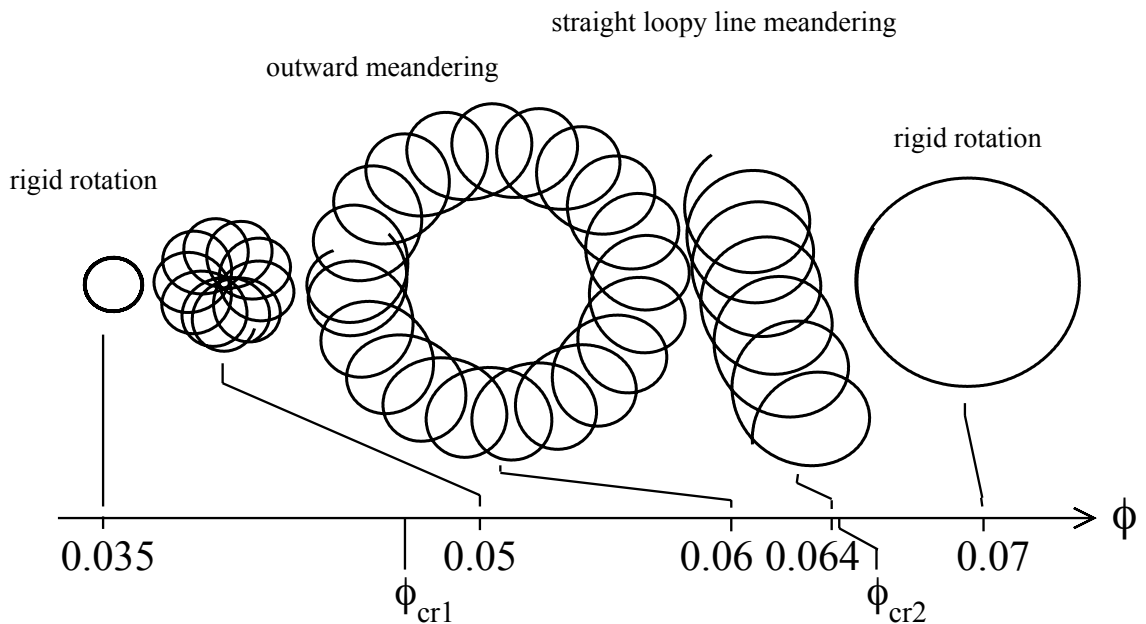


Figure 2.1: Tip path patterns obtained under variation of the bifurcation parameter ϕ . In the meandering regime $\phi_{cr1} < \phi < \phi_{cr2}$, rigidly rotating spiral waves are unstable. Simulation performed with the Oregonator model (2.1) and (2.2) and parameter set O1.

of outward meandering transforms to inward meandering. But in the depicted bifurcation scenario the regime of inward meandering is quite small. Both types of meandering are separated by the straight loopy line meandering, which is characterized by the fact that one radius is infinity. Finally, after crossing the threshold $\phi_{cr2} \approx 0.0643$ of a second supercritical Hopf bifurcation, rigid rotation is recovered again.

Following (Skinner & Swinney 1991) the tip path in the meander regime can be represented as a superposition of two circular motions with radii r_1 , r_2 , and frequencies ω_1 , ω_2 . In this representation the tip coordinates are given by

$$x(t) = r_1 \sin(\omega_1 t + \phi_1) + r_2 \sin(\omega_2 t + \phi_2) + c_1, \quad (2.3)$$

$$y(t) = r_1 \cos(\omega_1 t + \phi_1) + r_2 \cos(\omega_2 t + \phi_2) + c_2. \quad (2.4)$$

This superposition of the two circular motions is illustrated in Figure 2.2, where the blue line shows the path of an outward meandering spiral wave and the black circles represent the individual circular motions.

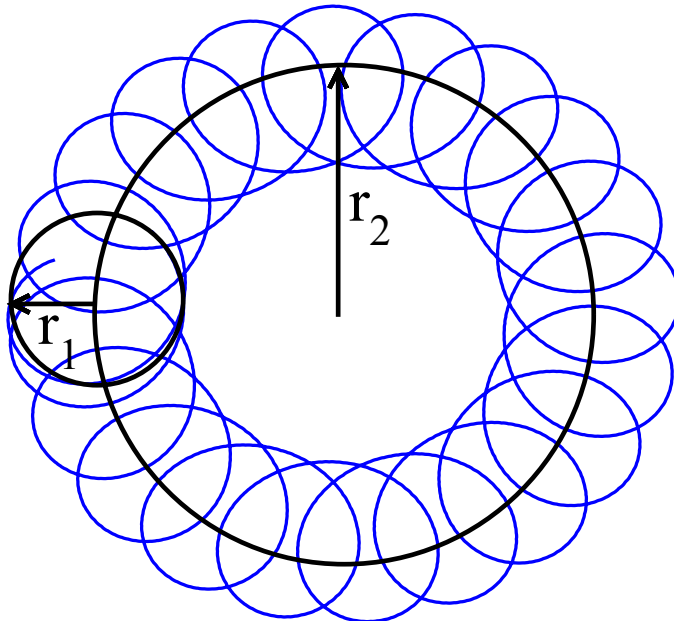


Figure 2.2: Illustration of the superposition of two circular motions in the meandering regime. The blue line denotes the trajectory of an outward meandering spiral wave tip and the black circles denote the individual circular motions.

A detailed analysis performed in (Plesser & Müller 1995, Skinner & Swinney 1991) demonstrates the validity and high accuracy of this representation near the Hopf bifurcation.

In our analyses we have fitted our numerical and experimental data for the tip trajectories to the equations (2.3) and (2.4). For rigid rotation only one circular motion exists hence we put $r_2 = 0$ for rigidly rotating spiral waves. In the analyses the parameters r_1 , r_2 , ω_1 , and ω_2 , in contrast to the constant parameters ϕ_1 , ϕ_2 , c_1 , and c_2 , change under variation of ϕ . The results obtained from our data are presented in Chapter 6.

More complicated hypermeandering motion has been reported, which includes at least three incommensurate frequencies (Plesser & Müller 1995). Such a bifurcation scenario with hypermeandering is presented in the next section in the FitzHugh–Nagumo model. However, the existence of chaotic dynamics cannot be excluded (Zhang & Patel 1995).

2.2 The FitzHugh–Nagumo model

The FitzHugh–Nagumo model (Winfree 1991, FitzHugh 1961, Nagumo et al. 1962) is another prominent example of a reaction–diffusion system that supports rotating spiral waves. The model is given by the equations

$$\frac{\partial u}{\partial t} = \frac{1}{\epsilon} \left(u - \frac{u^3}{3} - v - F(t) \right) + D_u \Delta u, \quad (2.5)$$

$$\frac{\partial v}{\partial t} = \epsilon (u + \beta - \chi v). \quad (2.6)$$

Here, $u(x, y, t)$ and $v(x, y, t)$ represent the dimensionless concentrations of the activator and the inhibitor, respectively, β , χ , and $\epsilon \ll 1$ are given parameters, and D_u denotes the diffusion constant of the activator. The term $F(t)$ specifies a parametric forcing applied to the medium.

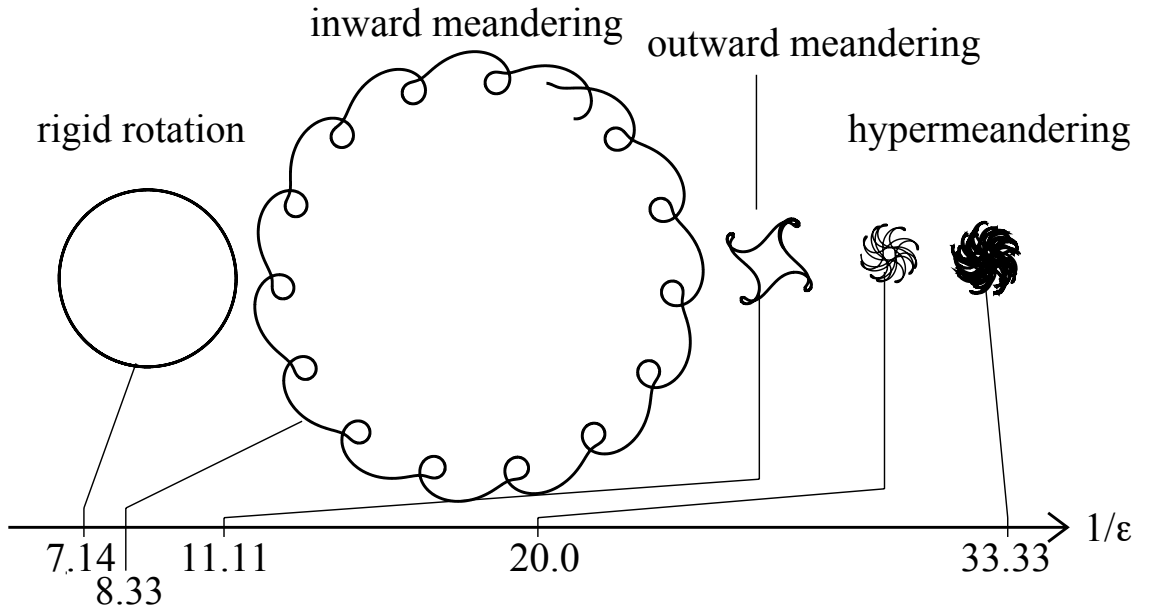


Figure 2.3: Trajectories of spiral wave tips obtained under variation of the bifurcation parameter ϵ . Simulation performed with the FitzHugh–Nagumo model (2.5) and (2.6) and parameter set F1. Figure taken from (Schlesner, Zykov & Engel 2008)

Different parameters in the FitzHugh–Nagumo model (2.5) and (2.6) result in rigidly rotating, meandering or hypermeandering spiral wave solutions (Winfree 1991). For fixed values of χ , β , and D_u , the regime of rotation is uniquely defined

by the parameter ϵ , which is considered the main bifurcation parameter in this thesis. The bifurcation scenario obtained under variation of ϵ is shown in Figure 2.3 for the parameter set F1 (please refer to section 3.5). At $\epsilon = 0.14$ ($1/\epsilon = 7.14$), the spiral is in the rigid rotation regime. Decreasing ϵ , a supercritical Hopf bifurcation occurs at a certain threshold and rigid rotation is replaced by inward meandering. When ϵ decreases further, inward meandering transforms to outward meandering. Finally, after crossing a second threshold the hypermeandering regime is established.

Due to the fact that in the hypermeandering regime more than two frequencies exist, the different frequencies cannot be identified by using the method described above, but rather Fourier–transformations.

3 Simulation methods

To perform simulations using the above mentioned models, one has to select numerical methods. In this section the numerical methods used for this thesis are introduced. Not only the integration methods, but also the determination of the position of the spiral wave tip as well as the initial conditions are described.

3.1 Numerical methods to solve reaction diffusion–systems

3.1.1 Forward–Euler–Method

All of the numerical results presented in this thesis were obtained by using the explicit Forward–Euler–method. This method is an explicit integration method for solving differential equations and can be used when the solution of the differential equation $\dot{y} = f(y, t)$ should be calculated for a given initial condition (t_0, y_0) . By using a constant time step Δt the solution for y at the time $t_i = t_0 + i \cdot \Delta t$ is denoted by y_i and can be calculated using the Forward–Euler–method from the preceding time–step:

$$y_i = y_{i-1} + \Delta t \cdot f(y_{i-1}, t_{i-1}). \quad (3.1)$$

Approximation methods with a higher order than the Forward–Euler–method, like the Runge–Kutta–method, have the advantage of being more precise and therefore the time step Δt selected can be larger. In this case, less time steps are necessary and calculation can be faster. On the other hand the calculation of each time step is more complicated and more time–consuming so that the acceleration effect can be shortened or compensated for completely.

By using the Runge–Kutta–method, no acceleration of our simulations could be detected, and so we decided to use the Forward–Euler–method after all.

3.1.2 Spatial discretization and approximation of the diffusion

For our simulation we used equidistant grids. This implies that we used the same step size in x - and y -directions, so that

$$\Delta x = \Delta y = h$$

with

$$\Delta x = x_i - x_{i-1} \quad (i \in \{1, N - 1\}) \quad \text{and}$$

$$\Delta y = y_j - y_{j-1} \quad (j \in \{1, M - 1\}),$$

where N, M are the numbers of grid points in x - and y -directions.

The aim was then to find an approximation for the diffusion terms $\Delta u(x, y)$ and $\Delta v(x, y)$. This could be achieved by using the Taylor Expansion for the terms $u(x \pm h, y = \text{const})$ and $u(x = \text{const}, y \pm h)$. These results can be used to express the diffusion term Δu :

$$-h^2 \Delta u_{ij} = -u_{i-1j} - u_{ij-1} + 4u_{ij} - u_{i+1j} - u_{ij+1} + \mathcal{O}(h^4), \quad (3.2)$$

where the notation $u_{ij} := u(x_i, y_j)$ is used for simplification.

In an analogous manner an approximation of the diffusion term can be calculated, which takes into account additional neighbouring points. This yields to

$$\begin{aligned} -12h^2 \Delta u_{ij} = & u_{i-2j} + u_{ij-2} - 16(u_{i-1j} + u_{ij-1}) + 60u_{ij} \\ & - 16(u_{i+1j} + u_{ij+1}) + u_{i+2j} + u_{ij+2} + \mathcal{O}(h^6). \end{aligned} \quad (3.3)$$

By neglecting the terms $\mathcal{O}(h^4)$ and $\mathcal{O}(h^6)$ (h has to be small) the five–point finite–difference representation

$$\Delta u_{ij} \approx \frac{u_{i-1j} + u_{ij-1} - 4u_{ij} + u_{i+1j} + u_{ij+1}}{h^2}$$

and the nine-point finite-difference representation of the Laplacian

$$\Delta u_{ij} \approx \frac{-u_{i-2j} - u_{ij-2} + 16(u_{i-1j} + u_{ij-1}) - 60u_{ij} + 16(u_{i+1j} + u_{ij+1}) - u_{i+2j} - u_{ij+2}}{12 \cdot h^2}$$

are obtained. Both approximations were used for our simulations. Due to higher consistency order of the nine-point approximation in comparison to the five-point approximation the spatial spacing can be larger using this approximation, but the calculation of each step is more complicated. In some test simulations no positive acceleration effect for the simulations could be observed and so we used the five-point finite-difference representation of the Laplacian for the majority of our simulations.

3.1.3 Boundary conditions

The boundaries in our experiments were non-flux-boundaries, so that we used the same boundaries for our simulations. These boundary conditions are called Neumann-Boundary-Conditions. For the five-point finite-difference approximations of the Laplacian this leads to

$$\Delta u_{i,j=0} = \frac{1}{h^2} (u_{i+10} + u_{i-10} + u_{i1} - 3 \cdot u_{i0}) \quad (i \in \{1, N-2\}) \quad (3.4)$$

for a boundary and to

$$\Delta u_{i=0,j=0} = \frac{1}{h^2} (u_{01} + u_{10} - 2u_{00}) \quad (3.5)$$

for an edge of the simulation area. The formulas for the other boundaries and edges are equivalent and are therefore not stated separately.

In our simulations with the nine-point finite-difference approximation of the Laplacian we used the above mentioned conditions for the direct boundaries. For the grid points only one point away from the boundary, we used the five-point finite-difference approximation.

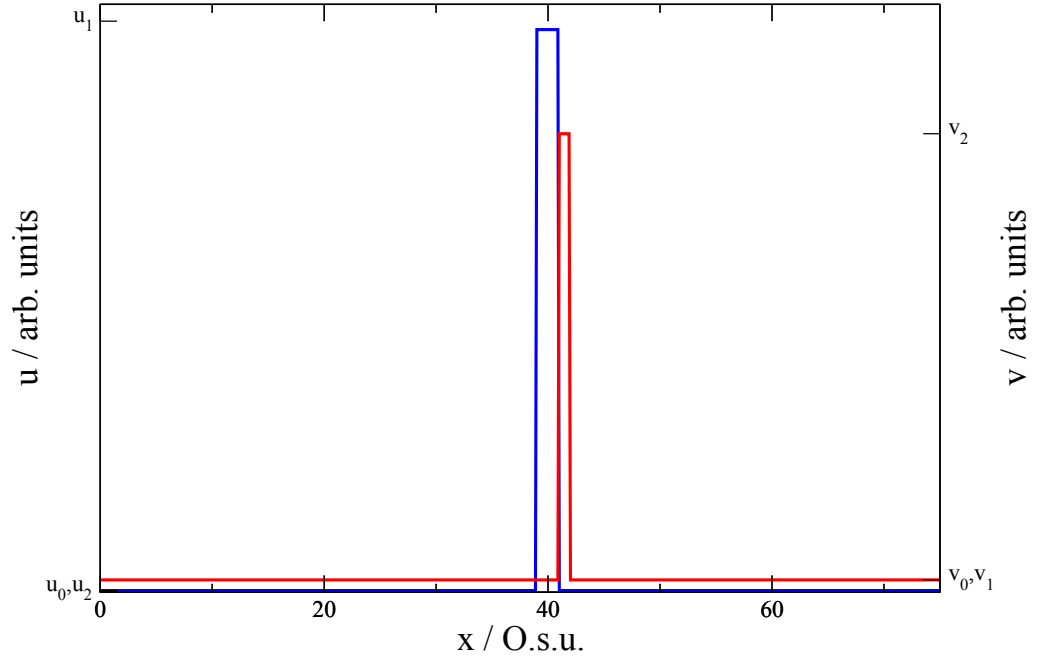


Figure 3.1: Initial condition to generate a wave in 1–dimensional Oregonator medium with parameter set O1 and $\phi = 0.045$. The blue line denotes the u –field and the red line the v –field. (For more details please refer to the text)

3.2 Initial conditions to generate spiral waves

To obtain spiral wave solutions of the Oregonator and FHN model, appropriate initial conditions have to be chosen as described in (Jahnke et al. 1989) or in (Schebesch 1999).

In our simulations we utilized the fact that the free end of a wave spirals in, finally forming a spiral wave. To do so we determined proper initial conditions to generate a wave front in a 1–dimensional medium. These initial conditions are then used to set up a wave with a free end in a 2–dimensional medium, which develops into a spiral wave.

To determine the appropriate initial conditions we used 1–dimensional simulations with periodic boundaries. The initial conditions to form a pulse in a 1–dimensional Oregonator medium are exemplified in Figure 3.1. Here parameter set O1 with $\phi = 0.045$ is used (please refer to section 3.5 for more details).

To generate a pulse we divided the x –axis into four parts and initialized the fields

with constant values within these parts. In Figure 3.1 we use the values $u_0 = 0.002$ and $v_0 = 0.0042$ for the first part ($x < x_0 = 39.0$ *O.s.u.*), $u_1 = 0.67$ and $v_1 = 0.0042$ for the second part ($x_0 \leq x < x_1 = 41.0$ *O.s.u.*), $u_2 = 0.002$ and $v_2 = 0.156$ for the third part ($x_1 \leq x < x_2 = 42.0$ *O.s.u.*) and again u_0 and v_0 for the final part ($x_2 \leq x$).

These determined initial conditions were used to initialize a wave front with a free end. For all $y < y_0$ we set up the field as described above constant in y -direction and for $y_0 \leq y$ we used the constant values u_0 and v_0 .

In Figure 3.2 the described generation for a spiral wave in a 2-dimensional Oregonator medium is illustrated. The initial conditions at $t = 0.0$ *O.t.u.* (Oregonator time units) for the u -field as well as for the v -field are shown at the top, while different developing steps of the spiral wave are depicted along the bottom. For this simulation the same parameters as for the pulse generation above were used. The simulation area had a size of 600×600 pixels.

To accelerate the simulations we added the possibility to save all fields at the end of a simulation and to use these saved states as initial states again. This is even possible when that the size of the simulation area is different. When the saved state size is larger, one can choose which part of the saved state is used for the initialization. In the case that the saved state is smaller than the size of the simulation area, the position where the saved state is located can be determined. All field values at the boundaries are copied to initialize all grid points which have not yet been initialized.

3.3 Detection of the tip position

There are different methods to detect the position of the spiral wave tip (Schebesch 1999). The method chosen for our simulation is based on the existence of a point close to the tip which does not move. We determine the shape of the spiral wave at two consecutive time steps and locate this non-moving point. The shape of the spiral wave is given by iso-concentration lines within the fields as shown in Figure 3.3(a) for the u - and v -field for an Oregonator medium.

The spiral wave rotates clockwise and the spiral wave tip moves with constant velocity along the boundary of the circular core shown by the dashed line. Since

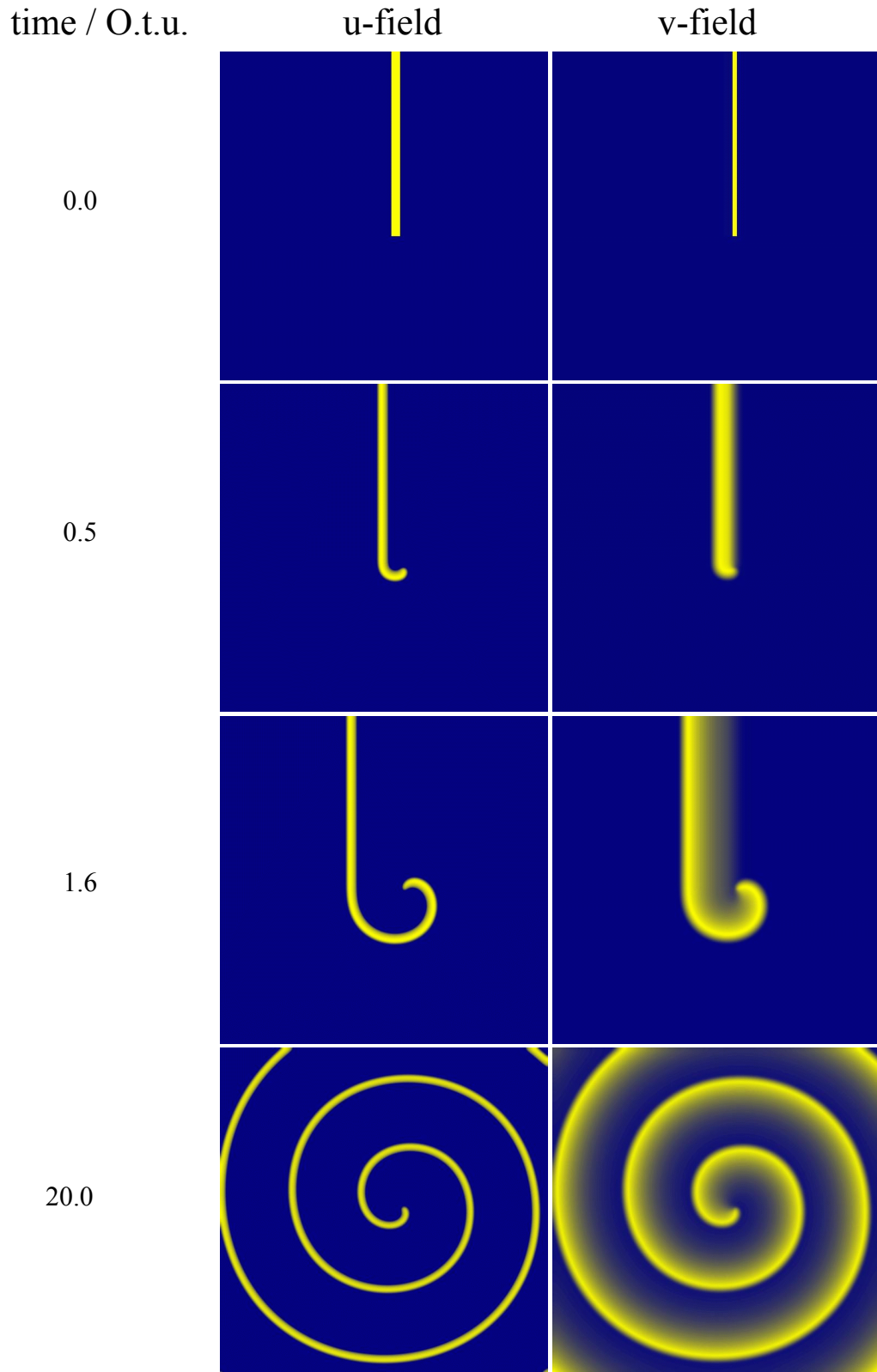


Figure 3.2: Spiral wave developing from a plane wave with a free end. Simulations are performed with the Oregonator model (2.1) and (2.2), parameter set O1, $\phi = 0.045$ and a simulation grid of 600×600 pixels.

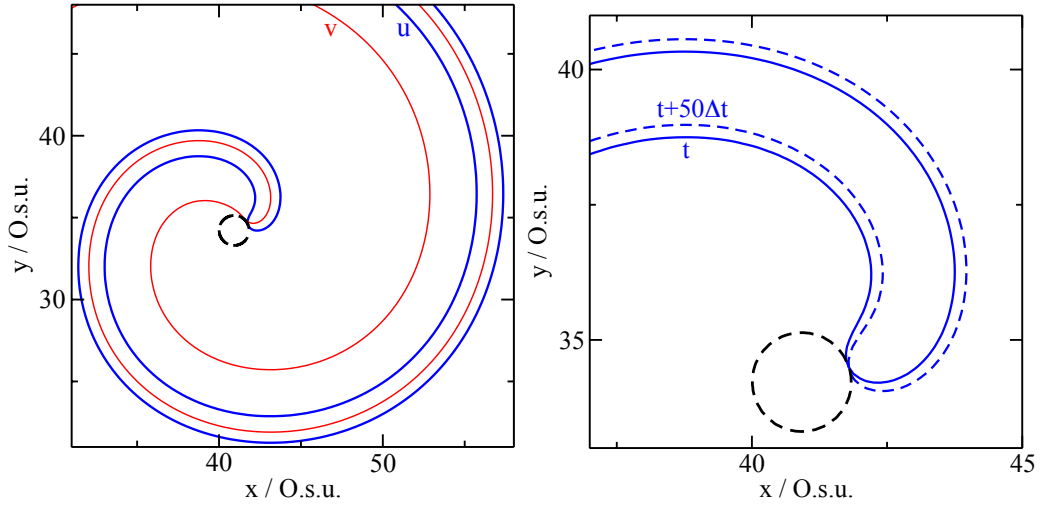


Figure 3.3: (a) Iso-concentration lines of the u - (blue line) and v -field (red line) of a rigidly rotating spiral wave. The tip follows the dashed circular trajectory. (b) Tip coordinates are obtained from the intersection between two iso-concentration lines of the u -field corresponding to time t (blue solid line) and time $t + 50 \cdot \Delta t$ (blue dashed line).

For both diagrams simulations are performed with the Oregonator model (2.1) and (2.2), parameter set O1, $\phi = 0.045$ and iso-concentration lines of the u -field at $u_c = 0.35$ and of the v -field at $v_c = 0.11$.

the velocity of the tip in the normal direction to the core boundary is equal to zero, we can define the tip coordinates from the intersection between iso-concentration lines corresponding to two neighboring time instants t and $t + \Delta t$, as illustrated in Figure 3.3(b).

For a more exact detection of the tip position we use linear interpolation of the fields and the positions of the intersection points between the relevant iso-concentration lines. However, since the detection of the iso-concentration lines is very costly, only the iso-concentration lines in the vicinity of tip position at the preceding time step are determined. This is possible because the tip position moves only slightly between two time steps. If the tip position cannot be located within this area, the search area is expanded to the entire simulation grid.

Name	q	f	ϵ	D_u	D_v	$\Delta t / O.t.u.$	$\Delta x / O.s.u.$
O1	0.002	1.4	0.02	1.0	0.6	0.00125	0.125
O2	0.002	1.4	0.02	1.0	0.0	0.00125	0.125
O3	0.002	2.0	0.1	1.0	0.0	0.002	0.2

Table 3.1: Parameter sets for the Oregonator model (2.1) and (2.2)

Name	β	χ	ϵ	D_u	Δt	Δx
F1	1.2	0.5	bif. parameter	1.0	0.002	0.1
F2	1.2	0.5	0.14	1.0	0.02	0.5

Table 3.2: Parameter sets for the FitzHugh–Nagumo model (2.5) and (2.6)

3.4 Co-moving simulation area

Especially when moving spiral waves (e.g. those caused by a control method) are studied, the use of co-moving simulation areas can reduce the computational effort significantly because a smaller simulation area can be chosen.

Here it is important to point out that we are not interested in boundary effects, that is, in interactions between the spiral wave and the boundaries. So it is essential that the tip does not lie close to the boundaries (Paulau, Löber & Engel 2013). For this reason we moved the simulation area in such a manner that the spiral wave tip was always in the middle of the simulation area. For our simulations in Chapter 7, where a detector line was used, we used the co-moving of the simulation area only for one axis (parallel to the detector line).

3.5 Simulation parameters

In this section all parameter sets for the simulations used in this thesis are stated. The parameter sets for the Oregonator model (2.1) and (2.2) are named by an 'O' followed by a number. The parameter sets for the FHN model (2.5) and (2.6) are named in the same manner, but with a leading 'F' instead of an 'O'. The parameter sets are stated in Tables 3.1 and 3.2 respectively. All model parameters as well as the normally used parameters for the numerical methods can be found there. The majority of our simulations were performed by the explicit Euler method, the five–

point finite-difference representation of the Laplacian and the parameters named in Tables 3.1 and 3.2. Where other numerical methods or parameters were used, it is pointed out in the text.

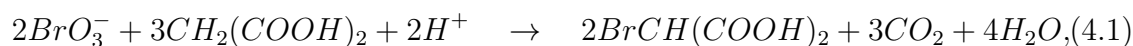
4 Experimental setup

In this chapter we introduce the light-sensitive BZ reaction briefly, the open gel reactor and two different experimental setups used for all of our experiments. We especially discuss the new experimental setup, that we have developed for experiments in which the light intensity has to be controlled spatio-temporally. The light-intensity was used as control force in our experiments.

4.1 The light-sensitive Belousov–Zhabotinsky reaction in an open gel reactor

Before the BZ reaction was discovered, the understanding of chemical reactions was that all chemical reactions proceed in such a way that the concentrations of all components go steadily towards the equilibrium state. Belousov discovered that during the oxidation of citric acid (in the presence of a catalyst) the concentrations of the components oscillated. At this time, such results were considered unbelievable to most scientists, which is why it took a long time before the results were confirmed by Zhabotinsky.

Today citric acid is usually replaced by other organic acids. In the majority of cases the oxidation of malonic acid ($CH_2(COOH)_2$) by bromate ions (BrO_3^-) is used. This reaction consists of many substeps and until now, not all of these substeps have been completely identified. Summarized this leads to



which means that the oxidation of malonic acid by bromate ions results in bromo-malonic acid ($BrCH(COOH)_2$), carbon dioxide (CO_2), and water (H_2O) (Field & Burger 1985, Schebesch 1999). Research groups like those of K. Showalter, O.

4.1. THE LIGHT-SENSITIVE BELOUSOV-ZHABOTINSKY REACTION IN AN OPEN GEL REACTOR

Steinbock, I. R. Epstein, V. K. Vanag, A. Munuzuri and M. Markus use this reaction for experiments.

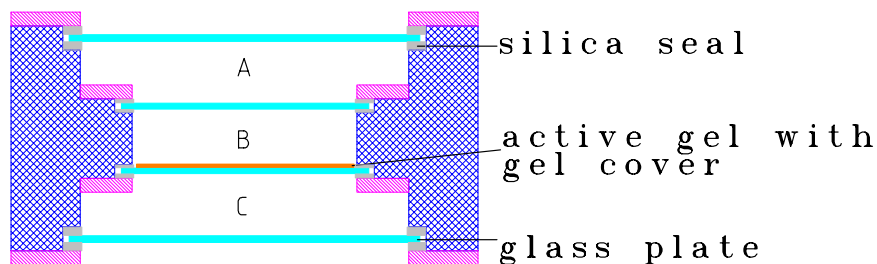
Since we are interested in studying control methods it is essential that global as well as local control forces can be applied to the observed medium. By using a light-sensitive catalyst and varying the light intensity, this condition is fulfilled. The light-sensitive catalyst utilized in the experiments was the catalytic complex Ruthenium-4, 4'-dimethyl-2, 2'-bipyrydyl.

To perform spiral wave experiments with the light-sensitive Belousov-Zhabotinsky reaction three major challenges have to be overcome. The first one is to maintain stationary non-equilibrium conditions; the second is to suppress instabilities or patterns induced by convective flow of the reactants, and the third one is to separate the actinic from the measuring light. To solve the first and second issues we used an open gel reactor, where the catalyst is fixed in a thin gel layer. This is described later in this section. In Chapter 4.3 we will discuss the third point.

The open gel reactor that we used in our experiments is similar to the reactor described in (Brandtstädter, Braune, Schebesch & Engel 2000). In Figure 4.1 the schematic representation of the reactor is depicted. The catalyst is immobilized in a silica hydrogel layer (orange layer) prepared on a plate of depolished glass (cyan layer). This ensures that convective-flow-induced patterns do not appear. To maintain stationary non-equilibrium conditions, the premixed feeding solution is pumped continuously, at a rate of 100 ml h^{-1} , through the Chamber B of the reactor (volume 60 ml). A magnetic stirrer provides spatially uniform conditions in the chamber. Chamber B is located between two further chambers, A and C, filled with water which circulates through a thermostat to maintain the temperature at 25.0°C . There are other experimental setups, where petri dishes containing the layer (Müller, Plessner & Hess 1987) are used, for example. The use of an open gel reactor instead of a petri dish maintains stationary non-equilibrium conditions significantly better. This facilitates the experiments, since it is not necessary to pause the experiments to change the gel and chemical solutions as often. Nevertheless even in the open gel reactor parameter drift does occur, caused by the aging of the gel with the catalyst. But this parameter drift is slow in comparison to that in petri dishes.

The catalytic complex Ruthenium-4, 4'-dimethyl-2, 2'-bipyrydyl is fixed in the silica hydrogel layer of 0.24 mm thickness. The active layer loaded with the cat-

cross section



front view

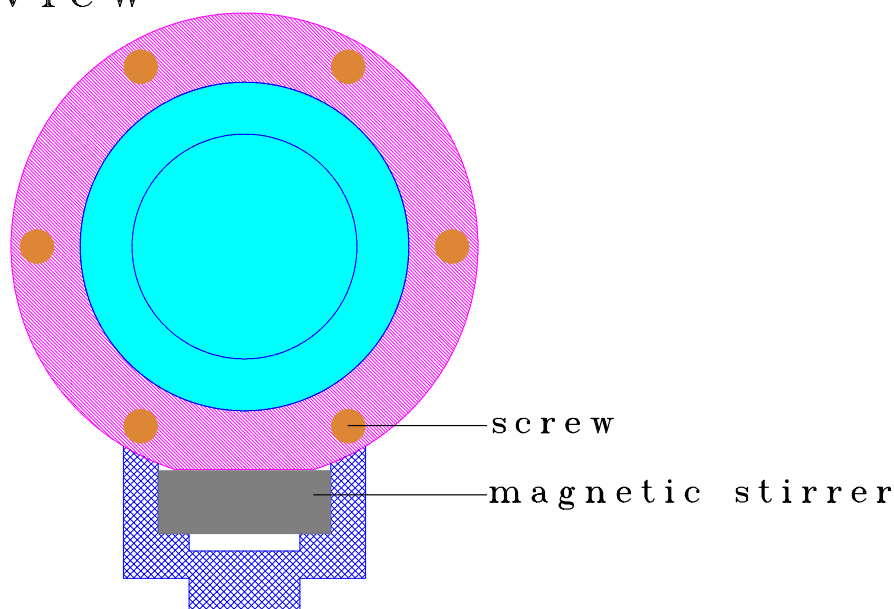


Figure 4.1: Open gel reactor. See text for details.

alyst (final concentration $[Ru(dmbpy)_3^{2+}] = 2.3 \times 10^{-3}M$) is in diffusive contact with a feeding solution prepared from stock solutions containing $[NaBrO_3]_0 = 2.1 \times 10^{-1}M$ (Aldrich, 99%), $[H_2SO_4]_0 = 3.1 \times 10^{-1}M$ (Aldrich, 95 – 98%), malonic acid $[CH_2(COOH)_2]_0 = 1.9 \times 10^{-1}M$ (Aldrich, 99%), and $[NaBr]_0 = 4.1 \times 10^{-2}M$ (Fluka, 99%). The active gel layer is covered by a gel layer of 0.24 mm thickness that is not loaded with the catalyst to protect the active layer from stirring effects.

Independent of the experimental setup, these experimental conditions were used for all of our experiments presented in this thesis. A single spiral wave, which constitutes the initial condition for the experiments, is created near the center of

the gel disk by breaking a wave front with an intense light spot. For the chosen concentrations and at a steady level of light intensity (0.36 mW cm^2) the spiral wavelength is $\lambda_0 \approx 2.0 \text{ mm}$. Far from the core center the rotation period is $T_\infty \approx 40 \text{ s}$.

To determine the tip coordinates in the experiments we used the same method as described for the numerical simulations (please refer to Chapter 3.3). Thus the location of the spiral wave tip is defined online as the intersection point of contour lines (here: $0.6 \times$ amplitude) extracted from two digitalized images taken with a time interval of 2.0 s. For the chosen conditions and in the absence of feedback, the spiral tip describes a four-petal trajectory.

4.2 Experimental setup for uniform applied light intensity

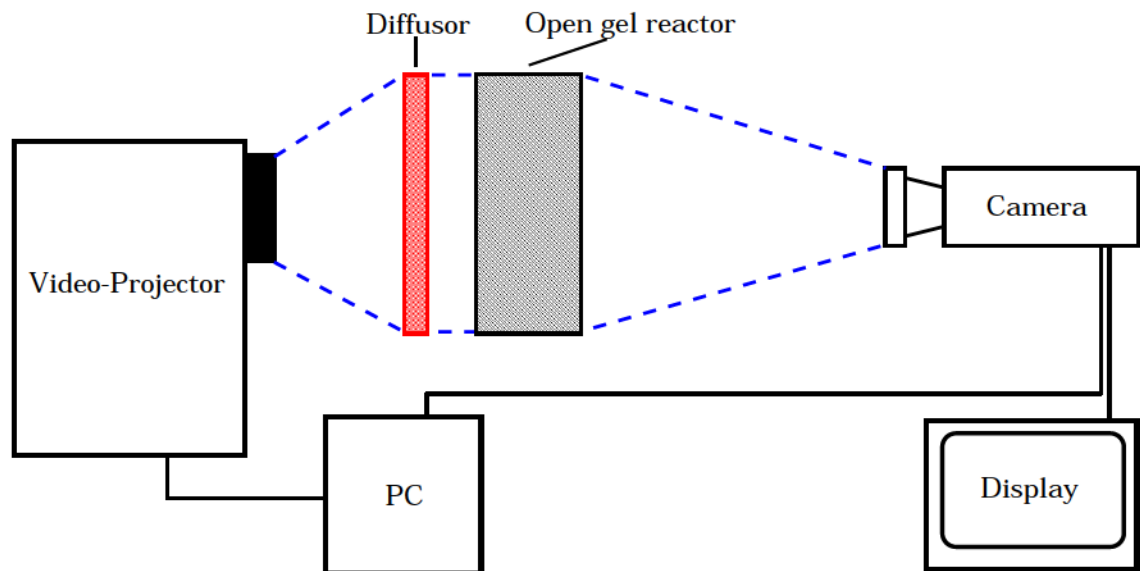


Figure 4.2: Schematic illustration of the experimental setup used for the experiments with uniform applied light intensity. The gel layer in the open reactor is illuminated by the homogenized light from the video projector. The light intensity is changed by the computer (PC) in accordance with the feedback algorithm and the pictures taken by the CCD camera. The blue lines are guides for the eyes to illustrate the optical path.

4.2. EXPERIMENTAL SETUP FOR UNIFORM APPLIED LIGHT INTENSITY

In this section the experimental setup used for experiments with uniform applied light intensity is presented. In Figure 4.2 this setup is illustrated schematically. The blue lines are guides for the eyes to illustrate the optical path of the control light. The active layer in the open gel reactor is illuminated by a video projector (Liesegang dv560flex) and the intensity is controlled by a computer (PC). The video projector is connected to the computer like a normal computer display. The software which steers the experiment spatially homogeneously changes the light intensity of the projector. Of course similar techniques such as the use of a computer-controlled power supply connected to the light source, can be used as well (Braune & Engel 2000). The light is filtered with a band pass filter (BG6, 310 - 530 nm) and additionally homogenized by the diffuser (red). This is necessary because the picture produced by the projector is not sufficiently homogenous. Normally, pictures produced by projectors are brighter in the middle and have decreasing intensity in the direction of the boundaries.

For feedback experiments the computer determines the global light intensity depending on the state of the chemical reaction. To do this, an image of oxidation waves appearing in the gel layer are detected in transmitted light by a CCD camera (Sony AVC D7CE) every second and digitalized with a frame grabber (Data Translation, DT 3155) for immediate processing by the computer. In the same time step the light intensity generated by the projector can be changed in accordance with the feedback algorithm.

So that the control does not influence the observation of the chemical reaction, it is essential that the control and monitoring lights are separated. Since both channels cannot be separated spatially in this setup, they are separated temporally. So we used a stroboscopic separation, which means that every time an image is taken by the CCD camera, the light intensity is set to the fixed background illumination. Of course, such a stroboscopic separation can influence the chemical reaction. But due to the fact that the light intensity is set to the fixed background illumination only for a short instant and that the period of the stroboscopic switching is very small (1s) in comparison to the period of the observed spiral waves (about 30 – 40s), the influence is minimized and can be ignored in most cases.

The most important disadvantage of this setup is that the light intensity cannot change spatially. So for control mechanisms with spatial-temporal control forces,

another experimental setup is required. Different possibilities, especially our newly developed experimental setup, are presented in the following section.

4.3 Experimental setup for space and time dependent applied light intensity

Here we are interested in spatio-temporal control in such a manner that the light-intensity can be changed temporal-dynamically as well as spatio-dynamically. In the case that the brightness of an inhomogeneous light pattern should only be varied temporally and not the light pattern itself, the experimental setup presented in the last section with an additional filter which generates the light pattern can be used. A more sophisticated experimental setup designed for global control with the initial light pattern is described in (Vanag, Yang, Dolnik, Zhabotinsky & Epstein 2000).

As video projectors are able to produce spatio-temporally changing pictures, they can be applied to experiments with spatio-temporal control as well. Obviously, in such a case the diffuser has to be removed, which leads to one of the major disadvantages of these setups. Since video projectors are typically inhomogeneous and the removed diffuser acts as homogenizer, the applied control force becomes inhomogeneous. The second disadvantage is that the optical systems of projectors are designed to produce a huge picture, while the gel layer normally has a size of only a few centimeters. So the optical system has to be adjusted either by placing other optical components in front of the system or by replacing the entire system. In (Mihaliuk, Sakurai, Chirila & Showalter 2002a) the optical system of the video projector was replaced by one that suits this application and the light intensity was homogenized to avoid both disadvantages.

In addition to the disadvantages mentioned above, a third major disadvantage exists. The light sources used in video projectors are not optimal for this application. In video projectors white light sources are used but the absorption band and the band of actinic light from the catalyst are located in the blue range. Another disadvantage of the projector lamps is their limited life-time, over which the light intensity decreases. This can lead to the incomparability of results measured at the beginning and at the end of their life-time.

To sum up, the use of both the optics and the light source of a video projec-

tor implicate several difficulties. They are not suitable for control light-sensitive chemical reactions. However until now the application of video projectors has been one of the most frequently used methods of controlling the light intensity spatio-temporally since some of the disadvantages can be avoided by reconstructing parts of the projectors.

Our aim, however, was not to adapt the components to fit the function, but rather to use only components which are optimal and specifically designed for this application and to develop a new setup for the light-sensitive BZ reaction. To do so we had to make three major decisions concerning the components and techniques used:

1. visualization technique,
2. separation technique of the controlling and observation channel, and
3. light sources.

Before the full experimental setup is presented, these three major points are discussed separately in the next subsection.

4.3.1 Visualization technique

Of course, the decision concerning the visualization technique used has a huge impact on every other decision. The optical system and the light source as well as separation techniques have to be aligned with the visualization technique.

Compared to the experimental set-up described in (Brandtstädter et al. 2000) we replaced the video beamer with a computer-controlled spatial light modulator (SLM 'LC2002', Holoeye Photonics AG) (Reményi, Várhegyi, Domján, Koppa & oke Lőrincz 2003, Hermerschmidt, Quiram, Kallmeyer & Eichler 2007). The SLM is a translucent liquid crystal display that can be connected to a computer like a monitor. The physical resolution of the display is 832×624 pixels. 800×600 of these pixels can be addressed with 8bit VGA signal resulting in 256 brightness levels for an intensity ratio around 3000 : 1. The main advantages of the SLM are its small panel size ($19.2 \times 25.6 \text{ mm}^2$), which facilitates the integration into the optical system and, an improved uniformity of illumination in the working area of the gel layer.

4.3.2 Separation of the optical channels

To prevent the effects of the spatio-temporal control light on the observations, there are three separation methods. The first one is to separate by time, the second by wave length and the third by polarization.

To separate the control and observation lights by time means to use stroboscopic separation (Grill, Zykov & Müller 1995, Kádár, Wang & Showalter 1998) as described above. Whenever an image is taken, the light is switched to a uniform brightness level for a short moment. Of course, this periodic variation in light intensity can lead to synchronization effects. However, because of the very short time scale of the stroboscopic separation in comparison to the intrinsic time scale of the system, these effects are normally estimated as negligible. Nevertheless we decided not to use stroboscopic separation to avoid this effect entirely.

For the second separation method, that is, by wavelengths, you have to apply two light sources with different wavelengths and place an interference filter in front of the camera. A significant difference between the absorption coefficients of the two catalyst states is observed for wavelengths larger than 600 nm which would provide a sufficiently large wavelength difference in comparison to the 470 nm wavelength region for the spectral filtering to work. However, the absolute value of the absorption is considerably lower than in the 470 nm wavelength region, therefore it is very difficult to obtain high-contrast images. This disadvantage can be suppressed by adding ferroin, as ferroin has a different absorption range (Toiya, Vanag & Epstein 2008).

The third possibility is to use polarization for the separation of both light channels, as done for global feedback in (Vanag et al. 2000). We employed this method to achieve spatio-temporal control of light intensity and simultaneous observation of chemical patterns. The constant background illumination of the observation light has to be taken into account as an offset in addition to the control light.

4.3.3 Light sources

The last major decision concerns the light sources used. Due to the fact that we used the polarization technique to separate both optical channels, we needed two different light sources: one for the control channel (major light source) and one for the observation channel, with different requirements.

Major light source

The major light source has to be optimal for the projection systems and so due to the image sharpness, the dimensions of the emitting area have to be small. On the other hand, the light source has to be bright as well. These two conditions are contrary, so it was necessary to find a compromise.

In the end we decided to use a blue HighPower-LED (Luminus PhlatLight PT120) which has been developed specifically for application in projection systems. Typically, the luminous flux Φ_V is 400 *lm* at the recommended continuous drive current $I_F = 18A$, however, this current can be increased up to $I_{F_{max}} = 36A$ with an expected luminous flux of approximately 600 *lm*. The LED PT120 emits light with the dominant wavelength of $\lambda_d = 463 \text{ nm}$ and the spectral bandwidth at 50% of the luminous flux of $\Delta\lambda_d = 25 \text{ nm}$. The emitted light is located in the same absorption band as the catalyst.

The advantages of LEDs in general are that they only emit light in a small spectral bandwidth and that they are very long-lasting without parameter drifts. In addition, the light emitted by a PT120 has an extremely high luminous flux, especially in comparison to other HighPower-LEDs, while the emitting area is very small ($4.6 \text{ mm} \times 2.6 \text{ mm}$).

At first we didn't take surface-emitting diodes into account. So we tested mainly the HighPower-LEDs Cree X-Lamp, Luxeon K2 and Luxeon Rebel. The tests with the Luxeon Rebel (LXML-PB01-0030) with a typically luminous flux of 58 *lm* at the drive current $I_F = 700 \text{ mA}$ and the dominant wavelength of 470 *nm* showed especially promising results. A couple of experiments went very well, but these HighPower-LEDs were not bright enough. For example, it is certainly not possible to erase patterns on a BZ medium with these LEDs. For this reason we tested surface-emitting diodes like the Luminus PhlatLight PT120 as well. Due to the fact that images generated with the PT120 are very sharp and the emitted light brightness is more than sufficient, we decided to use the PT120.

Background illumination

The light source for the observation light channel has to meet different requirements. In addition to the requirement that the gel layer has to be illuminated homogeneously, the CCD camera has to observe the light source as a constant back-

ground. Even by using shallow depths of field, it is very difficult to fulfill the second requirement if the light source is small.

Since the surface of electroluminescent foils shines extremely homogeneously, we first investigated the application of these foils, however, it turned out that their brightness was too low. By applying electroluminescent foils the computer could not detect the spiral waves reliably. However, should brighter electroluminescent foils be developed in the future, they could be a very good alternative.

In the end the application of normal, blue HighPower-LEDs like the Luxeon Rebel or K2 produced the best results. Since a homogeneously shining background is needed, the LEDs were used to illuminate a diffuser, which acted as this homogenous background (for more details please refer to the next subsection).

4.3.4 Experimental setup

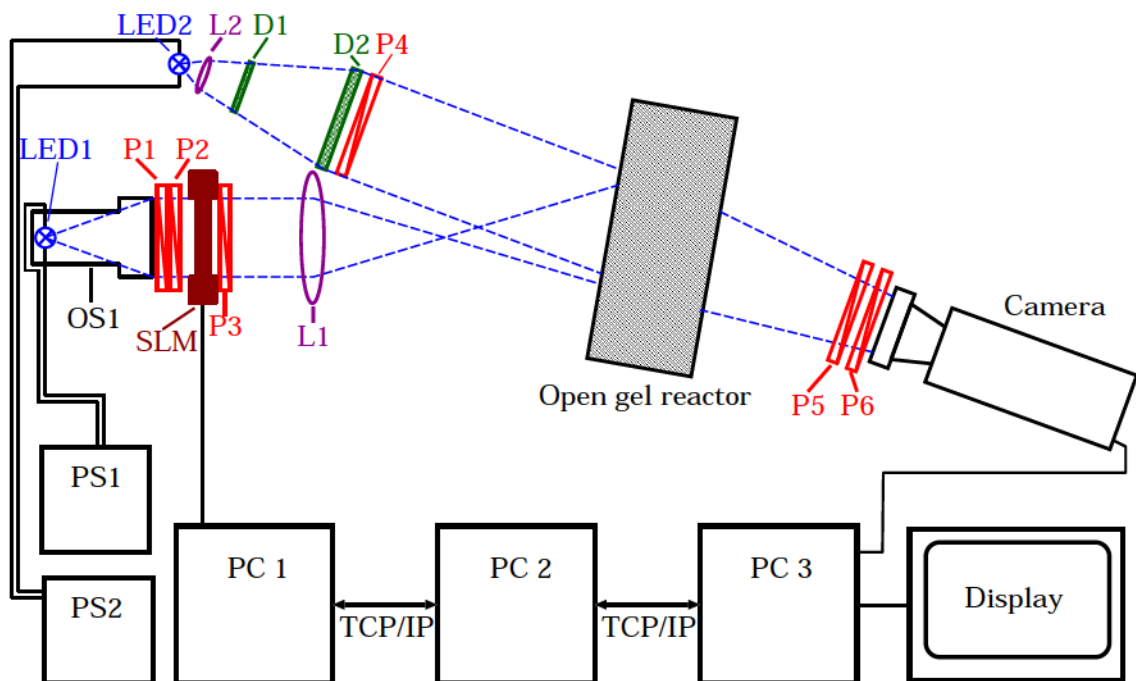


Figure 4.3: Experimental setup. See text for details.

In Figure 4.3 the schematic illustration of the experimental setup with both optical channels, the monitoring and the control channels, is shown. The optical control channel consists of a HighPower LED (LED1) with the optical system OS1 (SillOp-

4.3. EXPERIMENTAL SETUP FOR SPACE AND TIME DEPENDENT APPLIED LIGHT INTENSITY

tics Correctal TC 55, focal length 76 mm) which is adapted for the LED used, three polarizers (P1–P3), a lens (L1) and a spatial light modulator (SLM). The control light from the HighPower LED (LED1) is parallelized by the optical system OS1 and, after passing the polarizers P1 and P2, illuminates the SLM homogeneously. The SLM can be controlled by the computer PC1 like a normal display. The modulator modifies the linear polarization of the control light created by P2 depending on the gray level of each individual pixel. This modulation of the polarization is transformed by the polarizer P3 to an amplitude modulation of the light intensity of each pixel. The resulting image is mapped by the lens L1 onto the gel layer in the reactor. The intensity of the control light can be controlled by the power supply PS1 generating the current J_c and additionally by the orientation of polarizer P1 with respect to P2. Since the dependence of the light intensity on the current is not exactly linear, the intensity can be regulated more precisely by using the polarizer P1 than by the power supply PS1. The polarizers P2 and P3 have fixed orientations parallel to each other.

On the monitoring channel, the analyzing light from a HighPower LED (LED2) passes through a lens (L2), two diffusers (D1 and D2), a polarizer (P4), the open gel reactor, two polarizers (P5 and P6) and is then recorded by the camera. The diffusers provide homogeneous background illumination. The polarizers P4 and P5 are oriented in the same direction. Polarizers P3–P4 and P3–P5 are crossed to separate the optical channels for the control and analyzing lights emitted by light sources LED1 and LED2 respectively. By using the same pathway for the monitoring and the control channels the CCD camera records an inhomogeneous image as the lens L1 creates a bright circle on the image. Therefore both pathways are slightly rotated to prevent this effect. The applied control pattern can be visualized on a monitor but it is removed from the field of view of the CCD camera which monitors pattern formation within the gel layer. The brightness of the camera light can be controlled by the polarizer P6 and the power supply PS2. The camera used is the CCD monochrome camera DMK 41BU02.H with a resolution of 1280x960 pixels and is connected to the computer PC3 via a USB-interface.

In Figure 4.4 a photo of the new experimental setup is shown. When the picture was taken the polarizers P2 and P6 were not installed. The main light source LED1 is integrated into the optical system OS1 and is therefore not depicted.

4.3. EXPERIMENTAL SETUP FOR SPACE AND TIME DEPENDENT APPLIED LIGHT INTENSITY

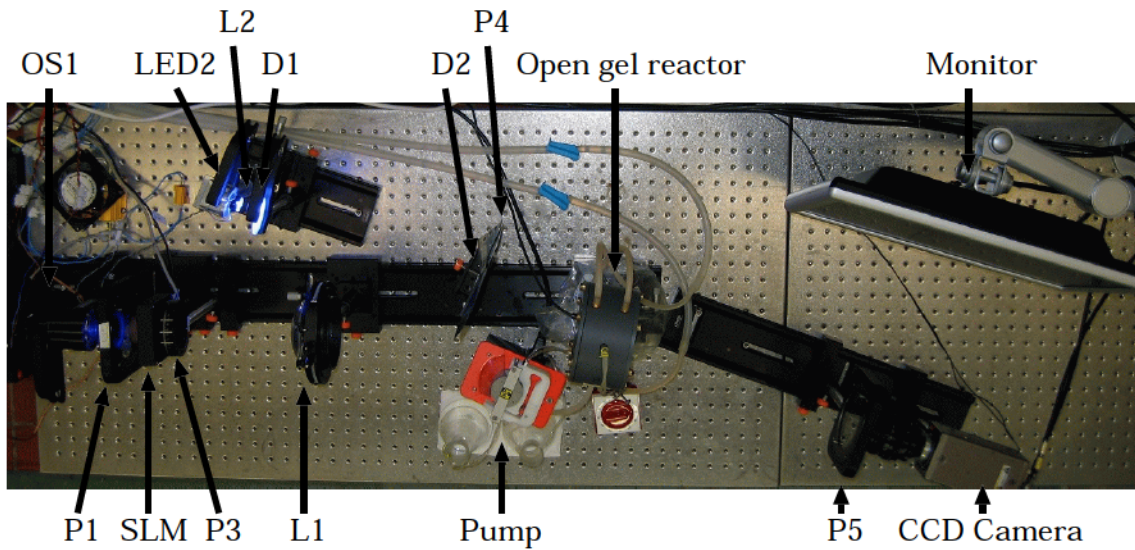


Figure 4.4: Photo of the new experimental setup. In comparison to the schematic illustration in Figure 4.3 the polarisers P2 and P6 are not installed.

The control software is a LabView-program which consists of three modules: the main module, the camera module, and the display module. The display module and the camera module control the displays and the cameras respectively. They are designed in such a way that they are able to control several displays and cameras for different experimental setups and for different main modules. For every experimental setup a main module has to run on its own. The main module provides a variety of different routines to control the experiments, to analyze and to visualize the data. With the use of well defined interfaces for the routines, the modules can be extended easily.

The three modules can run on different computers and communicate with each other through the network via TCP/IP. In the illustration in Figure 4.3 the main module is running on the computer PC2, the display module on the computer PC1, and the camera module on computer PC3. The display on PC3 shows the images, which are taken by the camera. This display is located directly next to the experimental setup and acts as a reference during the adjustment.

In our case, the camera module and the display module were running on the same computer. This computer can control up to eight displays. We needed a display interface for every SLM or projector, for the user interface display, and for

the displays which show the camera images. Additionally, the computer is equipped with two 1Gbit-network-cards, which support the link aggregation control protocol (LACP). The link aggregation, or IEEE 802.3ad, is a mechanism which allows us to bundle multiple physical network ports together in one single virtual port with a greater bandwidth than a normal port. Of course, the 3Com Baseline Switch 2924-SFP Plus used supports LACP as well.

5 Spiral wave dynamics under traveling wave modulation

As some of the first experiments with our new experimental setup that we have introduced in the last chapter, we performed experiments with traveling wave modulations. The behavior of spiral waves under traveling wave modulation has recently been studied in (Zykov et al. 2006, Ning-Jie et al. 2008, Wu, Gao, Ma & Ying 2012). Our aim was to verify the results regarding the synchronized drift of spiral waves and to demonstrate the capabilities of the new experimental setup. In the next section, the traveling wave modulation is introduced as well as the behavior of spiral waves under their application. Our experimental and numerical results are presented afterwards.

5.1 Traveling wave modulation

In this section the traveling wave modulation and the known behavior of spiral waves under such modulation are introduced. We refer mainly to the results from (Zykov et al. 2006).

Figure 5.1 illustrates the control procedure used in our reaction–diffusion simulations as well as in our experiments. In Figure 5.1(a) an unperturbed spiral wave and the trajectory of its spiral tip (red line) are depicted. A spiral wave in a Belousov–Zhabotinsky medium is shown, where the gray level is proportional to the concentration of the oxidized form of the catalyst used. Both axes are scaled in units of the unperturbed wavelength λ_0 .

The plot below illustrates a snapshot of the applied control pattern. Figure 5.1(b) shows the spatial dependence of the light intensity in the x –direction. The light intensity $I(x, y, t)$ is homogeneous in the y –direction and travels to the right, which

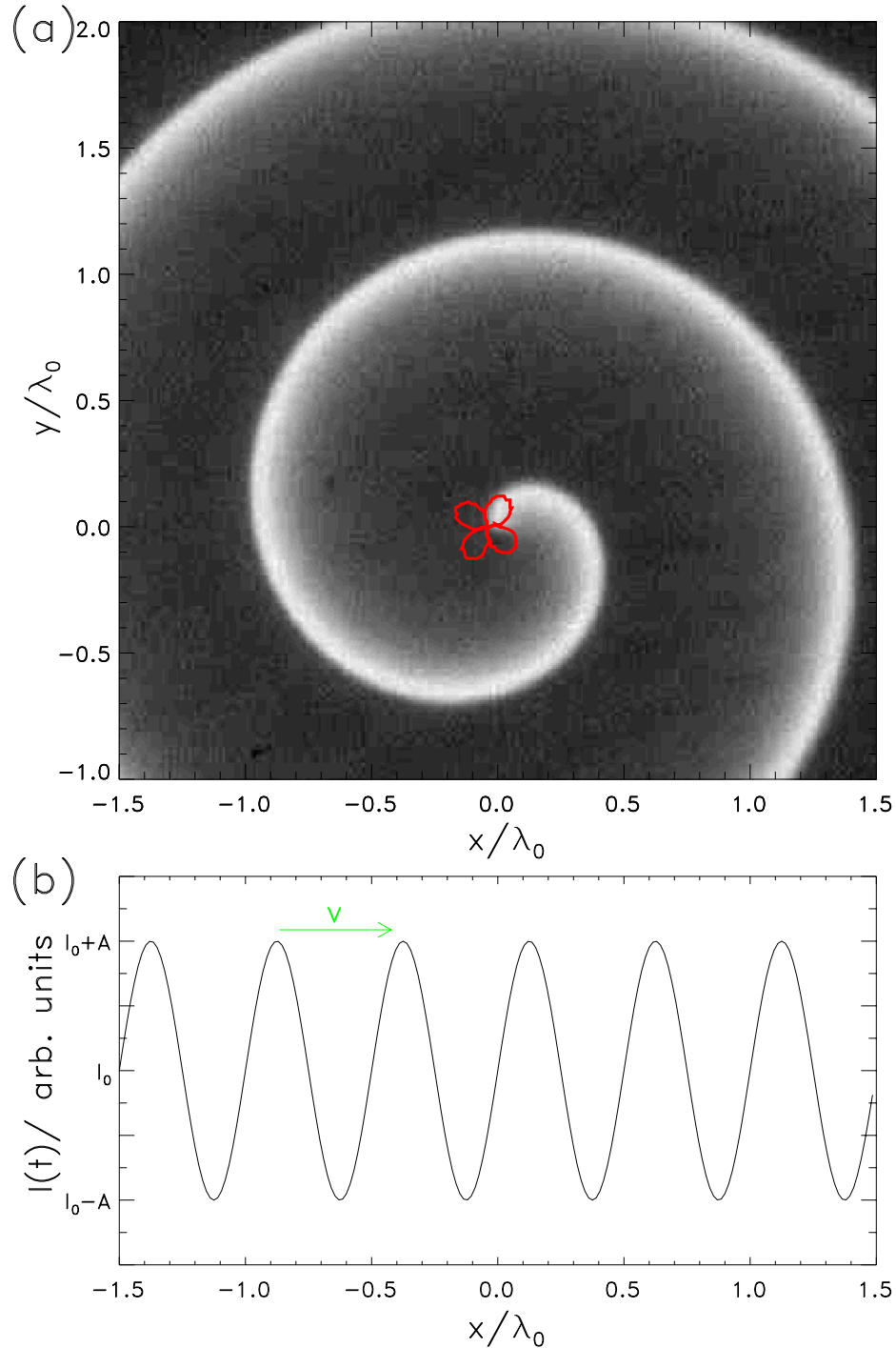


Figure 5.1: (a) An unperturbed spiral wave and the trajectory of its spiral tip (red) in the BZ reaction. The gray level is proportional to the concentration of the oxidized form of the catalyst. The spatial coordinates are depicted in units of the unperturbed wavelength λ_0 . (b) Snapshot of the applied light pattern, which travels from left to right with a velocity of $v = \omega_m/k_m$ (green arrow).

is indicated by the green arrow. The applied control pattern is given by

$$\begin{aligned} I(x, y, t) &= I_0 + A \sin(\omega_m t - k_m x) \\ &= I_0 + A \sin\left(\frac{2\pi}{T_m} t - \frac{2\pi}{\lambda_m} x\right), \end{aligned} \quad (5.1)$$

with the period of the light modulation T_m , its wavelength λ_m and the background illumination I_0 .



Figure 5.2: Trajectories of spiral wave tip under traveling-wave modulation computed for the kinematical model with different ratios $\frac{\omega_m}{\omega_0}$. Fig. from (Zkyov et al 2006).

In numerical simulations with the Oregonator model a resonant drift of the spiral

core within an interval of modulation periods, T_m , close to the period of rigid rotation, T_0 , has been predicted. The actual drift direction was found to be determined by the ratio T_m/T_0 . This is illustrated in Figure 5.2, which is taken from (Zykov et al. 2006). A closer analysis of a simplified kinematical model for the spiral core motion revealed that a condition for a synchronized drift is given by

$$\omega_0 = \omega_m \left(1 + \frac{v_d}{v} \sin \beta \right), \quad (5.2)$$

where $v = \omega_m/k_m$ is the velocity of the applied wave pattern, v_d is the drift velocity of the spiral wave tip, which is proportional to the modulation amplitude A , and β determines the drift direction (Zykov et al. 2006). Here it is assumed that the average rotation frequency is not influenced by the applied traveling wave modulation and is therefore equal to the rotation frequency ω_0 of the unperturbed spiral wave. In reality this is not quite correct, but the small resulting effect can be neglected here.

Equation (5.2) shows that in contrast to normal synchronization, no frequency locking is necessary for synchronized drift. This is caused by the motion of the spiral core, which induces a Doppler-shift of the modulation frequency. In addition, the synchronized drift occurs not only at a fixed value of modulation frequency ω_m , but also in a synchronization range. This is due to the fact that the direction of the spiral core motion is not fixed and can align itself to fulfill the synchronization condition. By taking into account that $-1 \leq \sin \beta \leq 1$ the synchronization range can be specified as

$$1 - \frac{v_d}{v} \leq \frac{\omega_0}{\omega_m} \leq 1 + \frac{v_d}{v}. \quad (5.3)$$

(Zykov et al. 2006).

5.2 Experimental observations

To verify the results from (Zykov et al. 2006) experimentally we used our new experimental setup, applying traveling wave modulation.

For the chosen experimental conditions (please refer to Chapter 4 for more details) the rotation period measured far from the core center was $T_\infty \approx 34$ s and the wave-

T_m/T_∞	0.95	0.96	0.97	0.98	0.99	1.00	1.01
$\alpha(\pm 5^\circ)$	342°	335°	338°	333°	330°	328°	164°!
T_m/T_∞	1.02	1.03	1.04	1.05	1.06	1.07	1.08
$\alpha(\pm 5^\circ)$	305°	280°	235°	162°!	-!	199°	162°

Table 5.1: Angle of the drift direction α in dependence on the ratio between the modulation period T_m and the rotation period of the unperturbed spiral wave T_∞

length was $\lambda_0 \approx 2.0 \text{ mm}$. By using the intersection point of contour lines extracted from two consecutive images taken with the time interval 1.0 s, we determined the location of the spiral wave tip online.

In Figure 5.1(a) an unperturbed spiral wave and the trajectory of its spiral tip (red line) are depicted. In the absence of forcing, the spiral tip describes a four-petal hypocycloid-like trajectory in contrast to the rigidly rotating spiral wave observed in (Zykov et al. 2006). Here, outward meandering waves are exposed to traveling wave modulations. Often the behavior of meandering and rigidly rotating spirals under external control is qualitatively similar (Zykov & Engel 2004). So we expected to observe comparable results to those obtained for the rigidly rotating spirals mentioned above. However, in the conditions for resonant drift the period of rigid rotation has to be replaced by the period of rotation far from the core, T_∞ .

The fixed control parameters are the control amplitude $A = 125$, the background illumination $I_0 = 125$ and a modulation wavelength $\lambda_m = 0.5 \cdot \lambda_0$.

In Figure 5.3 the trajectories of spiral wave tips (green line) and the trajectories of the core centers (dark blue lines) for different initial locations, $T_m/T_\infty = 1.01$ and $J_c = 5.0 A$ are depicted. Obviously, after a short transient, both spiral waves drift in the same direction. Similar to the case of a rigidly rotating spiral analyzed in (Zykov et al. 2006) the drift direction depends on the ratio T_m/T_∞ as shown in Figure 5.4. The trajectory of the spiral wave tip (green line) and the trajectory of its core center at the top of Figure 5.4 illustrate the relation between both trajectories. The trajectories of core centers (dark blue lines) underneath, show the drift directions for different ratios T_m/T_∞ . These results are in qualitative agreement with the data obtained in (Zykov et al. 2006), however there are also some differences in the results. In Table 5.1 the angles of the drift direction α , dependent on the ratio T_m/T_∞ are

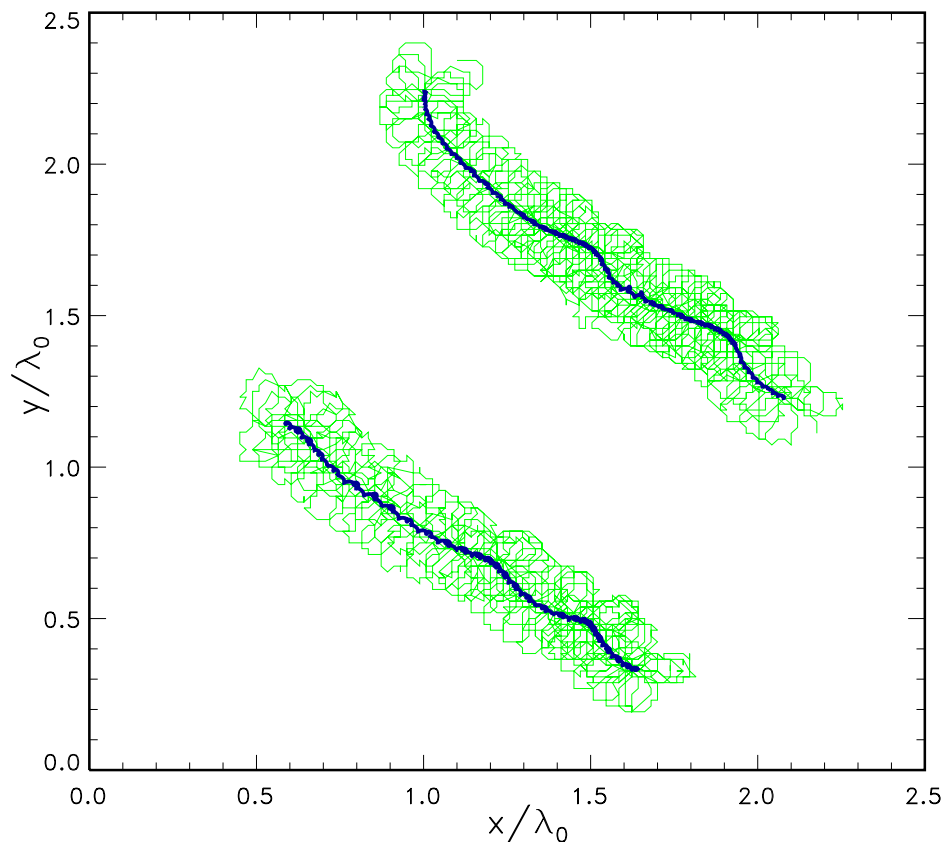


Figure 5.3: Trajectories of spiral waves (green line) and trajectories of its core centers (dark blue line) for different initial conditions, $T_m/T_\infty = 1.01$, and $J_c = 5.0 A$ in the BZ reaction (please refer to Chapter 4 for more details).

indicated. The results, which deviate from the expected values, are tagged with exclamation marks. In the case of $T_m/T_\infty = 1.06$ we were not able to identify a uniform drift direction. This can be caused by synchronization effects with other intrinsic periods of the meandering spiral wave.

5.3 Numerical verification

In addition to illustrating the qualitative agreement of the results with those obtained in (Zykov et al. 2006), our aim was to verify this experimental data by numerical simulations of meandering spiral waves. For our simulations we used the modified two-component Oregonator model (2.1) and (2.2) with the parameter set

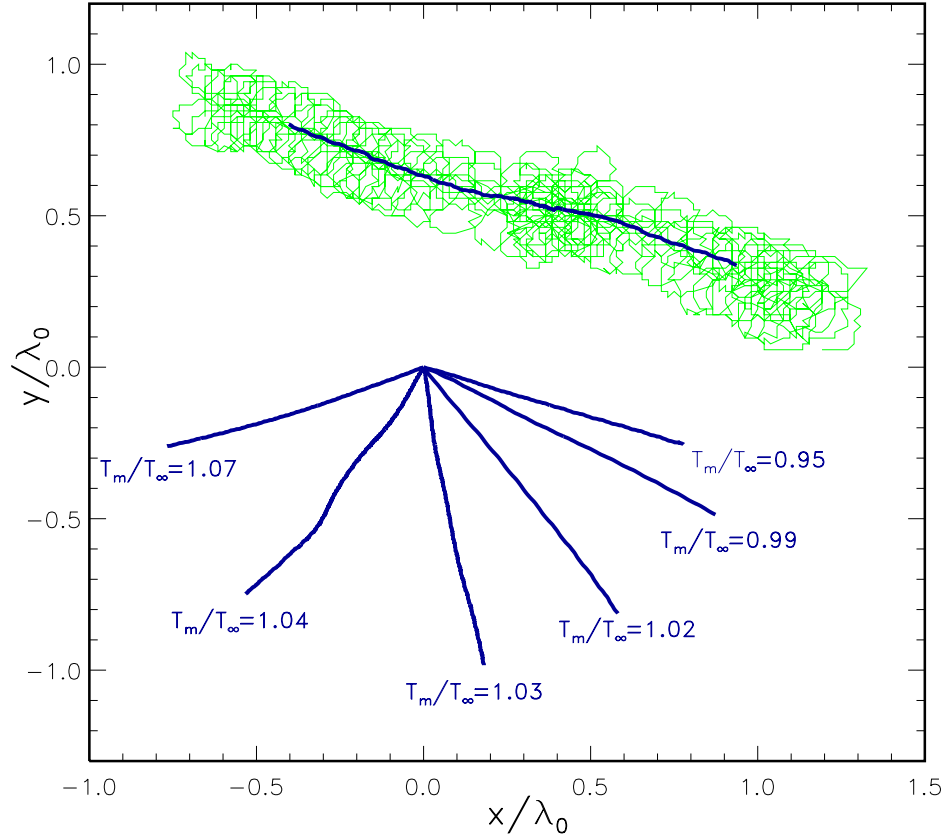


Figure 5.4: Spiral wave tip and core movement in the BZ reaction. Top: trajectory of a spiral wave tip (green line) and trajectory of its core center (dark blue line) for $T_m/T_\infty = 0.95$. Below: trajectories of core centers (dark blue lines) for different values of the ratio T_m/T_∞ , and $J_c = 7.0 A$ in the BZ reaction (please refer to Chapter 4 for more details).

O2.

The results of these numerical simulations under traveling wave modulation (5.2) obtained for $I_0 = 0.055$, $A = 0.0002$, and different ratios of T_m/T_∞ are depicted in Figure 5.5. At the top, the trajectory of the spiral (green line) and of its core center (dark blue line) for $T_m/T_\infty = 0.984$ are shown. Below, the trajectories of core centers for different values of the ratio T_m/T_∞ are presented.

The results depicted in Figure 5.4 and 5.5 are in very good qualitative agreement with each other. Both the experimental and the numerical observations show spiral wave drift under traveling-wave modulation. These drifts occur in a range

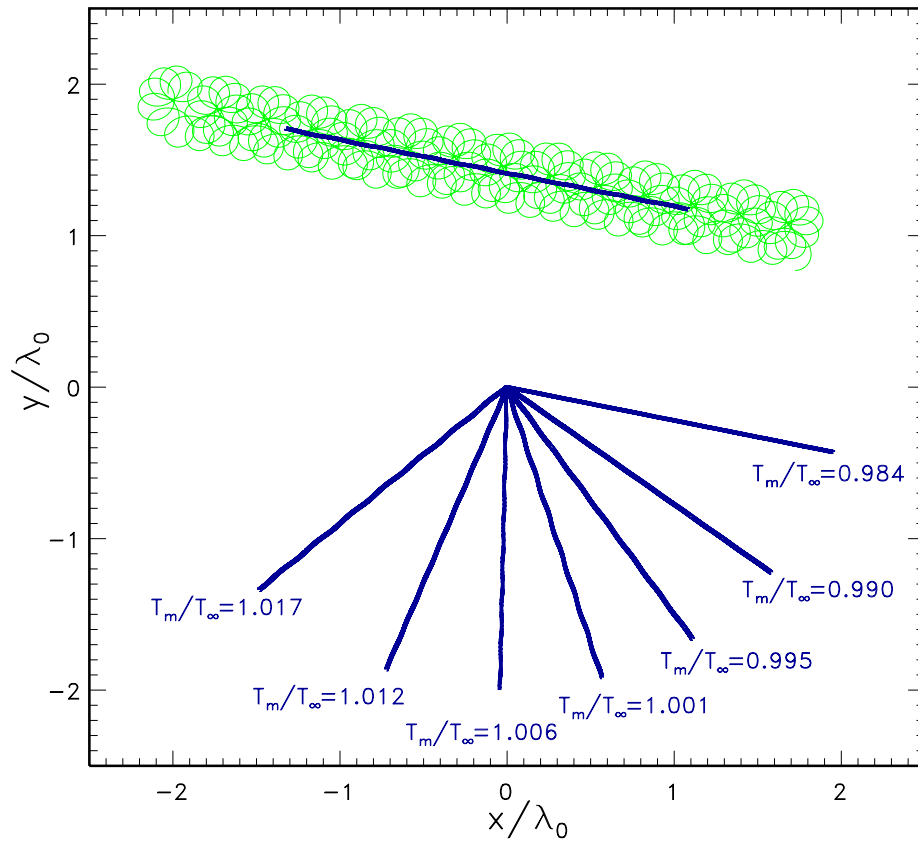


Figure 5.5: Top: trajectory of a spiral wave tip (green line) and trajectory of its core center (dark blue line) for $T_m/T_\infty = 0.984$. Below: trajectories of core centers (dark blue lines) for different ratios T_m/T_∞ . (For the simulations, the modified two-component Oregonator model (2.1) and (2.2) with the parameter set O2 were used – please refer to Chapter 3.5 for more details).

of the ratio T_m/T_∞ around 1.0. Moreover, the drift direction also depends on this ratio. Even the asymmetry towards greater values of T_m/T_∞ appears in both the experiments and the numerical simulations. Since the drift direction depends on the control amplitude A , the exact dependence of the direction on the ratio T_m/T_∞ is not as quantitatively comparable as expected.

6 Feedback–mediated stabilization of unstable rigid rotation

The theory of spiral waves has been intensively studied over recent years (Aranson, Aranson, Kramer & Weber 1992, Barkley 1992, Mikhailov, Davydov & Zykov 1994, Hakim & Karma 1999, Kessler, Levine & Reynolds 1994, Barkley, Kness & Tuckerman 1990, Barkley 1994, Fiedler, Sandstede, Scheel & Wulff 1996, Golubitsky, LeBlanc & Melbourne 1997, Sandstede, Scheel & Wulff 1997, Margerit & Barkley 2002, Wheeler & Barkley 2006, Löber & Engel 2013) but is still far from being complete. It has been shown that the transition from rigid rotation to meandering motion is a supercritical Hopf bifurcation. Beyond the bifurcation point, rigidly rotating spiral waves are still a solution of the underlying equations which is, however, unstable. As with any complicated nonlinear system, a very important step in the analysis of spiral dynamics is to determine the parameters of rigidly rotating spirals considered as steady states in a co-rotating reference frame. These parameters, for example their rotation frequency and their core radius, can be computed using standard procedures if the underlying model equations are known (Barkley 1992, Barkley 1994, Kapral & Showalter 1995, Wheeler & Barkley 2006). However, so far no methods to identify the parameters of these unstable solutions in experimental systems exists. To determine these parameters, an unstable two-dimensional spatio-temporal pattern has to be stabilized by using a non-invasive control method. Here the term *non-invasive* refers to the fact that the intrinsic unstable solution is not changed by the control term, and the control force vanishes when the orbit is reached.

Stabilization of strongly meandering spiral waves can also have a practical meaning, since such spirals break down, producing new interactive vortices that evolve into spatio-temporal irregularity, e.g. cardiac arrhythmia (Zhang & Patel 1995).

In this chapter, we study feedback–mediated stabilization of rigidly rotating spiral

waves in a parameter regime where, in the absence of feedback, rigid rotation is unstable and meandering spiral waves are observed. For stabilization, we use the two non-invasive methods proportional feedback control (PFC) and time delayed feedback control (TDAS), and demonstrate their successful operation when applied to spiral wave solutions obtained numerically from the Oregonator model for the light-sensitive BZ medium and from the FitzHugh–Nagumo model (Schlesner et al. 2006). The latter has been used widely to test feedback-mediated methods for the control of spiral wave dynamics (Mikhailov et al. 1994, Zykov, Bordiougov, Brandtstädter, Gerdes & Engel 2003, Zykov, Bordiougov, Brandtstädter, Gerdes & Engel 2004).

For both methods, not only the method and its application are discussed but also the application and the problems arising in real systems. As a rule, some control loop latency (CLL) is unavoidable when working with real systems and can strongly influence the operation of the control algorithm (Just, Reckwerth, Reibold & Benner 1999, Hövel & Socolar 2003). The problem is that control loop latencies can affect the system in such a way that the applied control methods are no longer able to stabilize unstable rigid rotation solutions. An example in which PFC fails to successfully control rigid rotation caused by control loop latencies will be shown and a method where this unwanted effect can be suppressed will be proposed. At the end of this chapter, both control methods will be compared, particularly in terms of their robustness.

6.1 Proportional Feedback Control

6.1.1 PFC without control loop latency

Proportional feedback control (PFC) has been successfully applied to stabilize wave segments propagating in a two-dimensional excitable medium (Mihaliuk, Sakurai, Chirila & Showalter 2002*b*). In a circular domain, PFC can force a rigidly rotating spiral wave to move towards the domain center (Zykov, Mikhailov & Müller 1997). Recently, rigid rotation of spiral waves was stabilized by PFC in a parameter range where it performed meandering or hypermeandering motion in the absence of feedback (Schlesner et al. 2006, Schlesner, Zykov & Engel 2008).

As already mentioned, one characteristic for rigid rotation is a constant distance

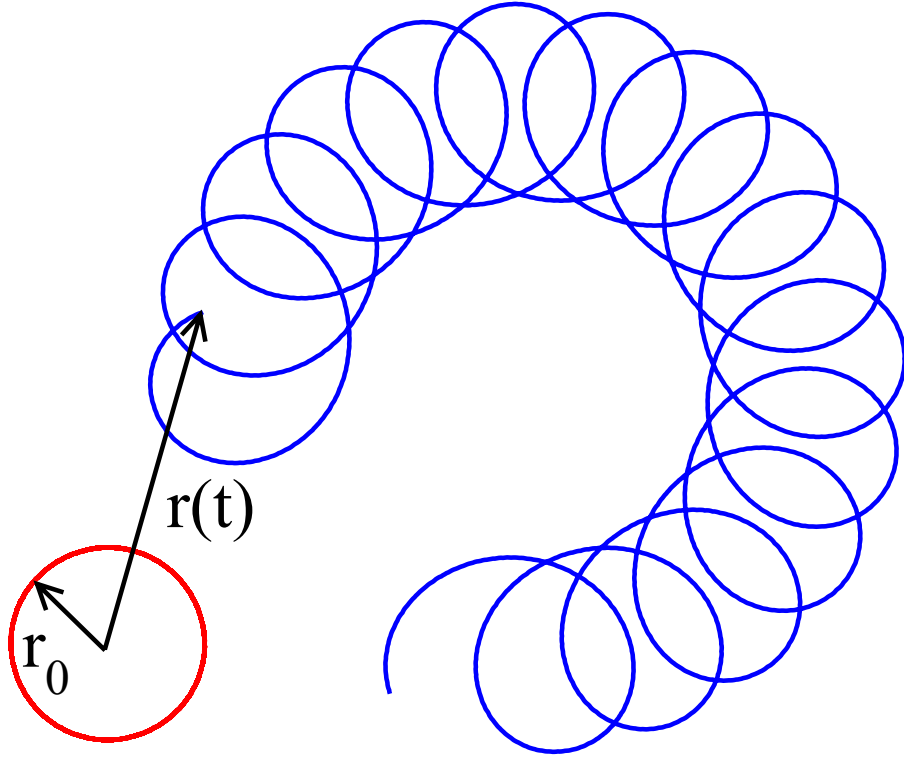


Figure 6.1: Illustration of proportional feedback control. The control force is proportional to the difference between the constant radius between the tip and the core center of a rigidly rotating spiral wave, r_0 , and the distance between the actual tip position and a chosen reference point, $r(t)$.

r_0 between the tip and the core center of the spiral wave. To suppress the meandering instability, we proposed applying a control force proportional to the difference between the actual distance from an arbitrarily chosen reference point, $r(t)$, and the desired radius r_0 according to

$$F(t) = K[r_0 - r(t)]. \quad (6.1)$$

Here, $F(t)$ denotes the control force and K is the feedback strength. In Figure 6.1 both distances r_0 and $r(t)$, the tip trajectories of an uncontrolled meandering spiral wave and a controlled rigidly rotating spiral wave are illustrated. The blue line represents the uncontrolled tip trajectory of an outward meandering spiral wave (please refer to the bifurcation diagram 2.1 at $\phi = 0.06$ as well), where at the end of this trajectory the distance between the actual tip location and the chosen reference

point, $r(t)$, is plotted. The red line represents the tip trajectory of the spiral wave with successful control of unstable rigid rotation. The arrow r_0 shows the radius of the rigidly rotating tip trajectory, which is the distance between the core center and the spiral wave tip location.

In experiments with the light-sensitive BZ medium, this feedback loop can be realized by changing the intensity of globally applied illumination; in this case the control force F is added to some fixed background illumination ϕ_0 :

$$\phi(t) = \phi_0 + F(t). \quad (6.2)$$

Of course, in our numerical simulations with the modified Oregonator model (2.1) and (2.2) we applied the feedback loop in the same manner, but for simulations with the FitzHugh–Nagumo model (2.5) and (2.6), we used the control force F directly, without constant offset.

Before we can apply PFC, the reference radius r_0 must be known. To determine r_0 simultaneously with the model equations, we solve simple relaxation dynamics according to

$$\frac{dr_0}{dt} = \frac{1}{\epsilon'} (r(t) - r_0). \quad (6.3)$$

Provided r_0 changes on a characteristic time scale much larger than the rotation period of the spiral wave, i.e., $\epsilon' \gg T$, this additional equation ensures that r_0 is adapted automatically during feedback-mediated stabilization. In the limit $t \rightarrow \infty$, $r_0(t)$ approaches the previously unknown value r_0 . After the reference radius r_0 is determined, we check that the additional Equation 6.3 does not influence the system dynamics by performing simulations or experiments with the determined fixed reference radius.

Figure 6.2(a) displays the tip trajectory calculated from the Oregonator model (2.1) and (2.2) in the presence of PFC given by Equations (6.1), (6.2), and (6.3) with the parameter set O1, $\phi_0 = 0.06$, $K = 0.005$ and $u_c = 0.35$. The cross marks the reference point. Initially, when the feedback strength is zero, the tip follows a path characteristic for outward meandering (blue line). At $t = 25$ *O.t.u.* the feedback is switched on. Now the tip moves along the red line demonstrating that, after a short transient, the tip becomes attracted to a circular orbit of radius r_0 centered at the

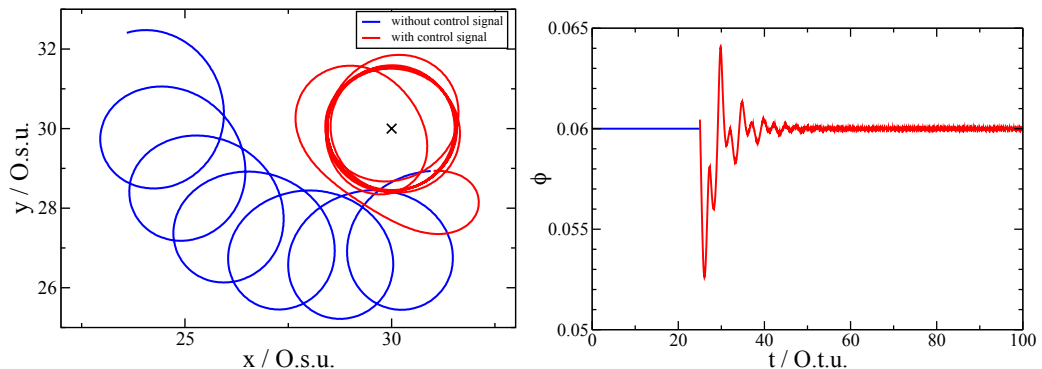


Figure 6.2: Stabilization of rigid rotation under proportional feedback control with tip coordinates defined from the u -field (Oregonator model (2.1) and (2.2) with PFC (6.1) and (6.2) and parameter set O1, $u_c = 0.35$, $\phi_0 = 0.06$). (a) Trajectory of the spiral tip without feedback ($K = 0$, blue line) and under feedback control ($K = 0.005$, red line) which is switched on at $t = 25$ O.t.u.. The cross marks the reference point. (b) Control parameter $\phi(t)$ as a function of time; in the stabilized regime the control force $F(t)$ vanishes.

reference point. Thus, rigid rotation is stabilized in a parameter regime where it is unstable in the absence of feedback. In the stabilized regime the control force vanishes: compare Figure 6.2(b). Hence, the proposed control method stabilizes an existing unstable periodic orbit (UPO) and does not induce a new periodic solution.

We performed such stabilization for different values of the control parameter ϕ_0 within the meandering regime $\phi_{cr1} < \phi < \phi_{cr2}$. The dashed line in Figure 6.3 represents the results obtained for the core radius and the rotation frequency in the feedback-stabilized regime. A quantitative analysis of the simulation data shows that in the whole meandering regime the radius of the stabilized trajectory is equal to r_1 and that its frequency coincides with ω_1 .

In order to show that PFC can be successfully applied to stabilize unstable rigid rotation in general and furthermore to demonstrate that rigid rotation can be successfully stabilized by PFC in the hypermeandering regime, we additionally performed numerical simulations with the FHN model 2.5 and 2.6 with the parameter set F1.

The spiral wave tip trajectory in the regime of inward meandering ($\epsilon = 0.12$) under PFC is depicted in Figure 6.4(a). Again, the cross marks the reference point, the

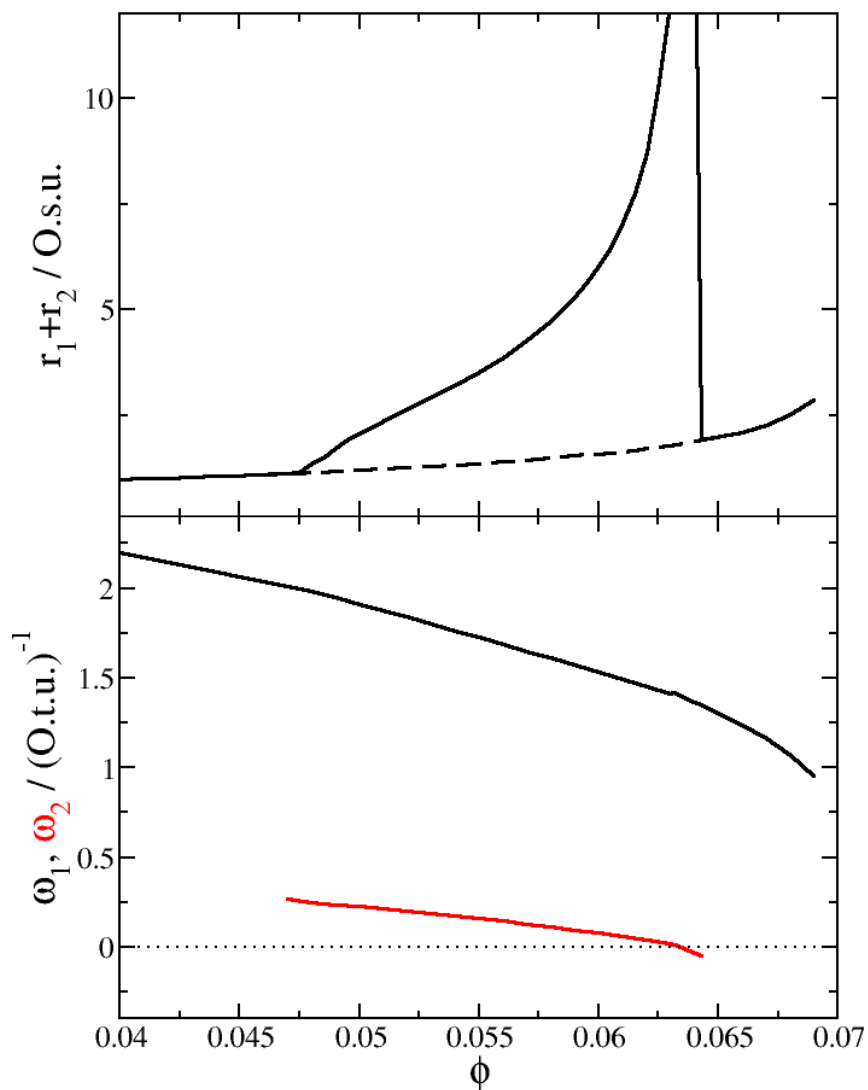


Figure 6.3: (a) The sum of the radii of a meandering tip trajectory $r_1 + r_2$ vs. the control parameter ϕ . The dashed line denotes the radius r_1 of unstable rigid rotation in the meandering regime. (b) Dependence of the frequencies ω_1 (black line) and ω_2 (red line) on ϕ . The vertical lines illustrate the two Hopf bifurcations and so the meandering regime in which rigid rotation is unstable. (Oregonator model (2.1) and (2.2) with PFC (6.1) and (6.2) and parameter set O1)

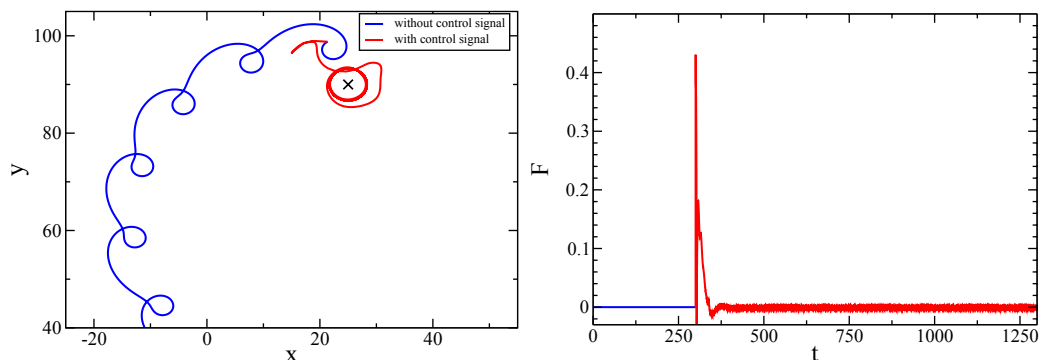


Figure 6.4: Successful stabilization of rigid rotation in the inward meandering regime. Simulations performed in the FHN model (2.5) and (2.6) with PFC (6.1), the parameter set F1, and $\epsilon = 0.12$. (a) Trajectory of the spiral wave tip without feedback (blue line) and under PFC (red line). The cross marks the reference point. (b) Control force $F(t)$ as a function of time. At $t = 300$ the feedback control was switched on. After successful stabilization of rigid rotation the control force vanishes.

blue line the tip trajectory without feedback and the red line the tip trajectory under PFC. The form of the blue line shows the characteristic form of a tip trajectory for outward meandering spiral waves (please refer to the bifurcation scenario introduced in Figure 2.3 as well). At $t = 300$ the PFC is switched on, the tip is attracted by the reference point, and shortly afterwards the unstable rigid rotation is successfully stabilized. In Figure 6.4(b) the control force $F(t)$ as a function of the time t is displayed. When the rigidly rotating motion of the spiral wave tip is stabilized, the control force vanishes.

We expected that for a greater distance from the Hopf bifurcation at which the rigid rotation becomes unstable, it is more difficult to stabilize the unstable rigid rotation solution. This expectation was confirmed by the fact that at $\epsilon = 0.03$ (in the hypermeandering regime) it took more effort to stabilize rigid rotation by PFC, but by starting in the vicinity of the unstable periodic orbit (UPO) stabilization of the rigid rotation was easier and faster. Figure 6.5(a) displays the tip trajectory of successfully stabilized rigid rotation. Under PFC the spiral tip becomes attracted to a circular orbit (red line) of radius r_0 centered at the reference point (black cross). When the feedback is switched off the tip leaves the circular orbit and after a short transient, follows a path which is characteristic for a hypermeandering spiral wave

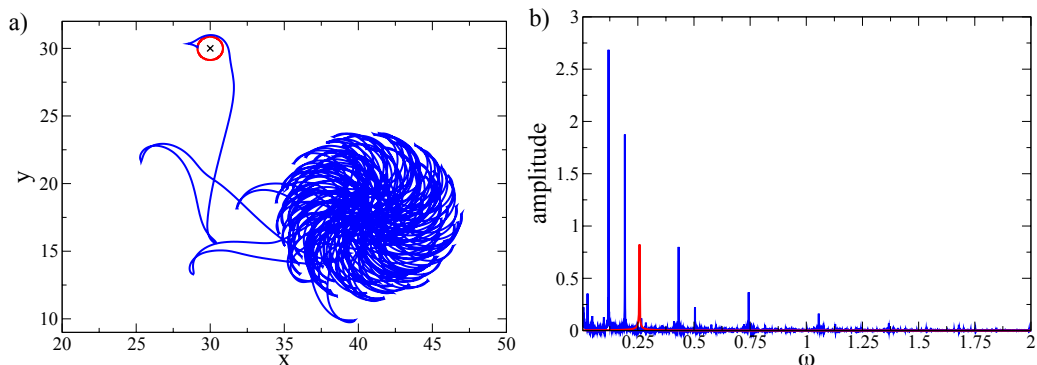


Figure 6.5: (a) Rigid rotation of a spiral wave in the hypermeandering regime stabilized by PFC (red line). At time $t = 2000$, the feedback force is switched off, and the spiral tip moves along the blue line characteristic for hypermeandering. Simulations performed with the FHN model (2.5) and (2.6) with PFC (6.1), parameter set F1, $u_c = 0.2$, $\epsilon = 0.03$, and $\epsilon' = 200$. (b) Fourier spectra of controlled (red) and uncontrolled (blue) tip motion. Figures from (Schlesner, Zykov & Engel 2008)

(blue line).

In Figure 6.5(b) the Fourier spectra of the controlled (red) and uncontrolled (blue) tip motion is displayed. In the case of the uncontrolled hypermeandering tip motion, more than two basic frequencies exist (as in the inward and outward meandering regime) on a continuous background. Under feedback, this complicated motion is replaced by the stabilized periodic orbit with a characteristic one-frequency spectrum, from which radius $r_0(\epsilon)$ and frequency $\omega(\epsilon)$ were taken to determine the properties of the unstable rigid rotation in dependence on the bifurcation parameter ϵ . The amplitude $r_0(\epsilon)$ and the frequency $\omega(\epsilon)$ of the rigid rotation branch are plotted in Figure 6.6(a) and (b) respectively.

To speed up the numerical calculations, activator and inhibitor field of a rigidly rotating spiral wave stabilized at a certain ϵ value are used as an initial condition for feedback-mediated stabilization at a slightly changed value $\epsilon + \delta\epsilon$. Sometimes it is not possible to stabilize a UPO at certain parameters starting from stable solution. In this case, this method can additionally facilitate further tracking of the UPO.

The results obtained from simulations with the Oregonator as well as the FHN model demonstrate that it is possible to suppress both the transition to meandering as well as the hypermeandering non-invasively by means of global PFC. In the

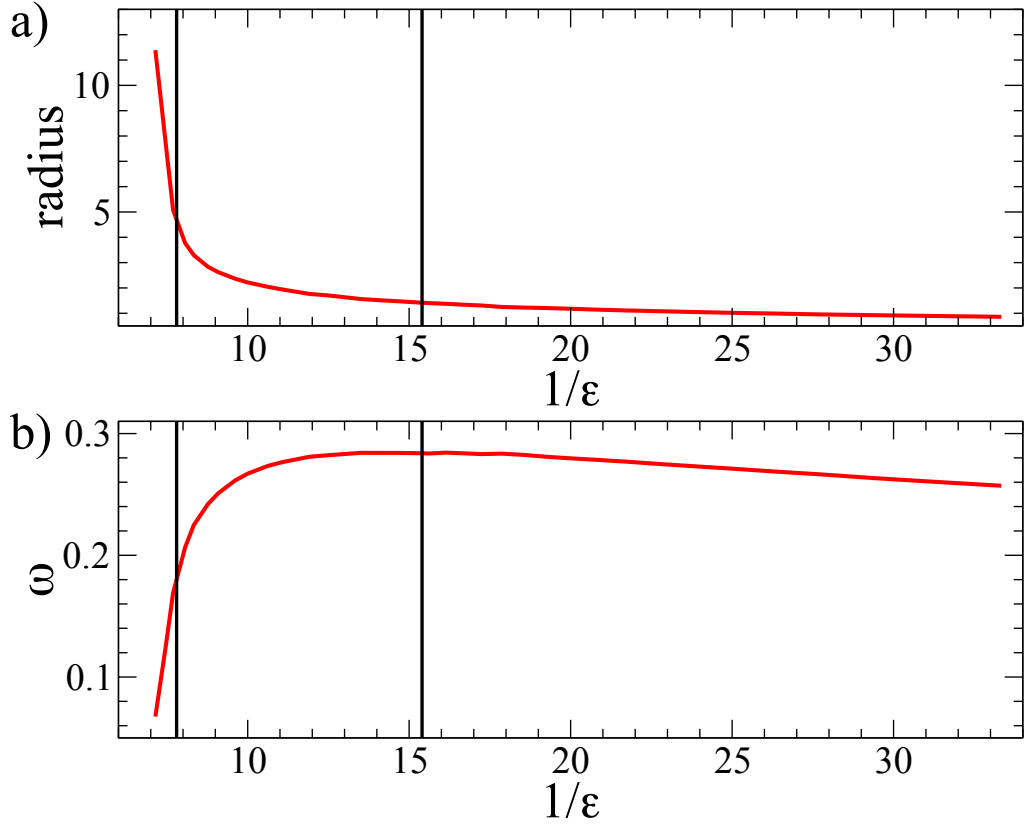


Figure 6.6: Core radius (a) and rotation frequency (b) of feedback-stabilized rigid rotation vs. the bifurcation parameter ϵ for the FHN model (2.5) and (2.6) with PFC (6.1) and parameter set F1. Left and right vertical lines mark the transition to meandering and hypermeandering in the absence of feedback. Figures from (Schlesner, Zykov & Engel 2008)

stabilized regime, the whole medium oscillates periodically at the rotation frequency of the spiral wave. Finally, we emphasize that application of non-invasive PFC can stabilize a periodic two-dimensional pattern in a broader parameter range with quite irregular autonomous spatio-temporal dynamics.

6.1.2 PFC with control loop latency effects

In light-sensitive BZ media, the experimentally accessible variable is v instead of u . Since v is proportional to the oxidized catalytic complex, which has a lower absorption coefficient than the reduced complex, areas with high (low) v concentration appear bright (dark) in transmitted light. Consequently, in experiments with

the BZ medium the coordinates of the spiral tip have to be determined from the measured data for the v -field.

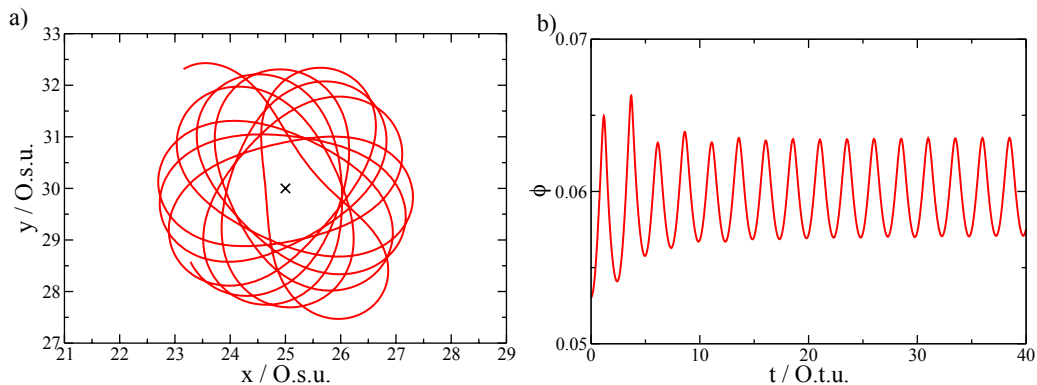


Figure 6.7: (a) Tip trajectory under proportional feedback control with tip coordinates defined from the v -field. The tip moves to the neighborhood of the reference point (black cross), however rigid rotation cannot be stabilized. (b) Undamped oscillations of the control force are observed in the asymptotic state. (Oregonator model (2.1) and (2.2) with PFC (6.1) and (6.2) and parameter set O1). Figures taken from (Schlesner et al. 2006)

We checked how this modification affects the operation of the feedback algorithm. Figure 6.7(a) shows the tip trajectory obtained for conditions identical to those used in Figure 6.2(a) with the exception that the tip coordinates are calculated from the iso-concentration lines of the v -field. Obviously, under these conditions it is impossible to stabilize rigid rotation in the meandering regime. Asymptotically, the trajectory traced out by the spiral tip is not a circle, although its symmetry center is located at the chosen reference point. Moreover, in the asymptotic state the control force does not vanish but exhibits undamped oscillations. Hence, the asymptotic trajectory represents a feedback-induced motion rather than a UPO of the unperturbed system. The same breakdown of the modified feedback algorithm has been observed for other values of the control parameter ϕ_0 within the meandering regime. Additional experiments confirm these findings. In the experiments, PFC is able to move the spiral wave tip towards the reference point but is not able to successfully stabilize the unstable rigid rotation.

To overcome this problem, we propose a simple method that allows approximation of the u -field approximately from the v -field. Taking into account that v is the slow

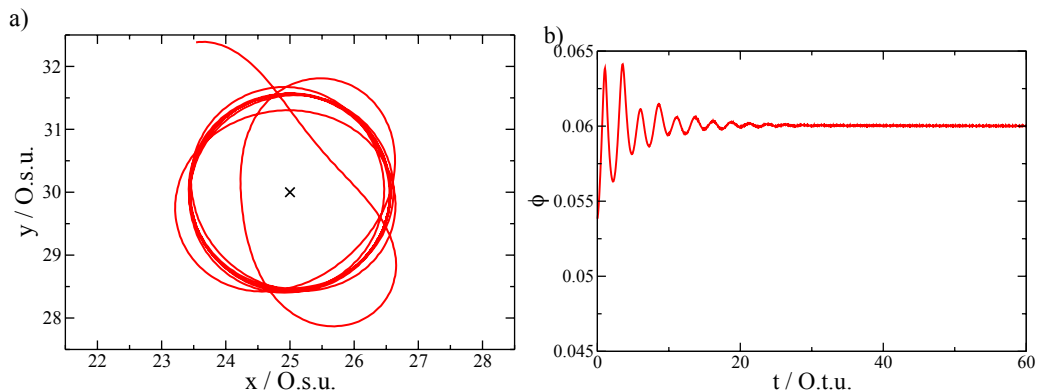


Figure 6.8: (a) Successful stabilization of rigid rotation by PFC defining the tip coordinates from the reconstructed activator field u_{re} (Equation (6.4) with $\mu = 0.05$). The cross denotes the reference point. (b) Time evolution of the control parameter $\phi(t)$ demonstrating the non-invasive character of the control. (Oregonator model (2.1) and (2.2) with PFC (6.1) and (6.2) and parameter set O1). Figures taken from (Schlesner et al. 2006)

variable, we neglect the diffusion term in Equation (2.2)

$$\frac{\partial v(x, y, t)}{\partial t} \approx \frac{v(x, y, t) - v(x, y, t - \mu)}{\mu} \approx u(x, y, t) - v(x, y, t) \quad \cancel{\mp D_v \Delta v}$$

and define the auxiliary field

$$u_{re}(x, y, t) = \frac{v(x, y, t) - v(x, y, t - \mu)}{\mu} + v(x, y, t). \quad (6.4)$$

We set the parameter μ equal to 0.05 *O.t.u.* which corresponds to a time interval of about one second between two consecutive pictures of the v -field taken in the experiment. As followed from Figure 6.8(a), we succeeded in stabilizing rigid rotation by proportional feedback, provided the tip coordinates were determined from the reconstructed field u_{re} . The control force vanishes in the stabilized state and ϕ becomes equal to ϕ_0 ; compare Figure 6.8(b).

A closer inspection revealed that latency effects might be responsible for the sensitivity of the control method to different procedures for the definition of the tip coordinates. Note that ϕ enters into Equation (2.1) for the activator field of the Oregonator model. Due to time scale separation, a perturbation in ϕ affects

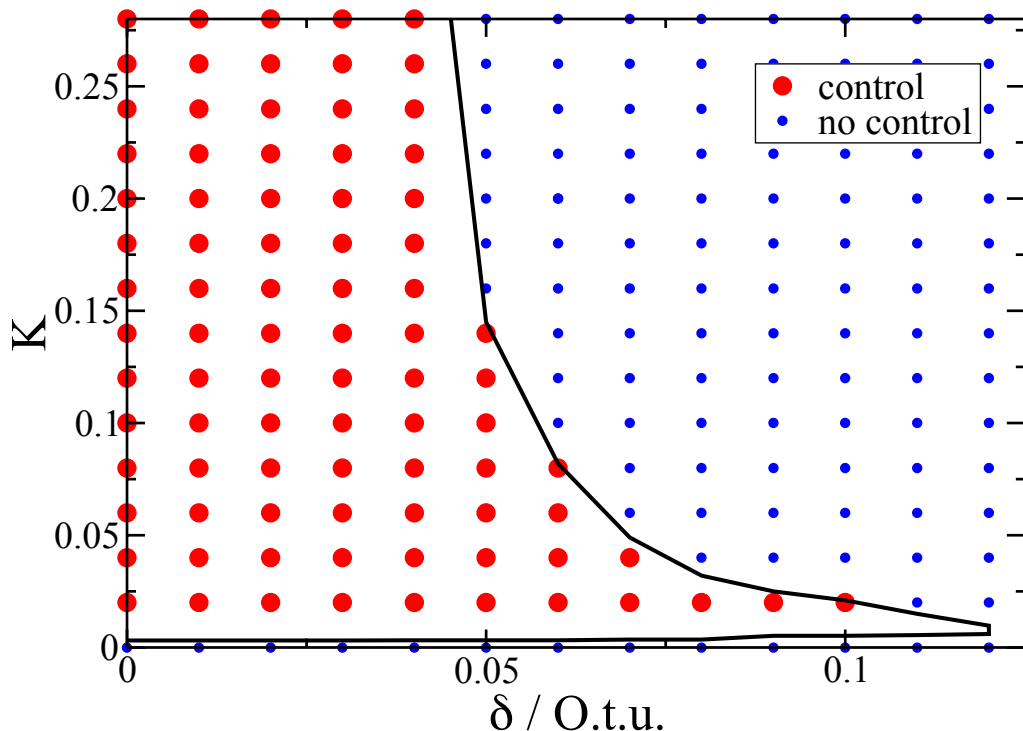


Figure 6.9: K - δ diagram for proportional feedback control for $\phi_0 = 0.06$ (Oregonator model (2.1) and (2.2) with PFC (6.1) and (6.2) and parameter set O1). Full red circles (small blue dots) denote successful stabilization (failure of stabilization), the boundary of the control domain determined with steps of 0.0005 in the parameter K is marked by the solid line. Tip definition is based on the u -field. Figure taken from (Schlesner et al. 2006)

the inhibitor field with a certain time delay. To give a rough estimate of the delay between u and v in response to a ϕ perturbation, we stabilize rigid rotation for a certain ϕ -value, say $\phi_0 = 0.06$. With $u_c = 0.35$ and $v_c = 0.085$ for the definition of the iso-concentration lines, the radii of the circular tip trajectory calculated from the u - and v -fields are equal. When we switch off the feedback and increase ϕ from 0.06 to 0.061, the tip leaves the circular orbit. Deviations from the circular orbit appear with some time delay and initially grow linearly with time. The trajectory determined from the v -field responds with a larger time delay. From the linear growth range we estimate a time delay between u and v equal to $\delta_{uv} \approx 0.13$.

To understand whether a control loop latency δ equal to δ_{uv} is large enough to cause a stabilization failure at $\phi_0 = 0.06$, we replace $F(t)$ in Equation (6.1) by $F(t - \delta)$. Figure 6.9 displays the control diagram in the parameter plane spanned

by the feedback strength K and the control loop latency δ . As expected the control domain shrinks with increasing latency time. An upper limit $\delta_{cr} = 0.12$ exists for successful stabilization which turns out to be smaller than $\delta_{uv} \approx 0.13$. This proves our conjecture that latency effects cause the breakdown of stabilization, as previously discussed.

6.2 Time Delay Autosynchronization

6.2.1 TDAS without control loop latencies

PFC is commonly used to stabilize unstable steady states, but the instability of rigid rotation can also be viewed as a transition from a stable to an unstable periodic orbit (UPO) (Barkley et al. 1990, Barkley 1992, Barkley 1994, Fiedler et al. 1996, Golubitsky et al. 1997, Sandstede et al. 1997). Non-invasive feedback methods like time delay autosynchronization (TDAS) (Pyragas 1992, Socolar, Sukow & Gauthier 1994) have been successfully employed to stabilize UPOs in dynamical systems (Kittel, Parisi & Pyragas 1995, Just, Reckwerth, Möckel, Reibold & Benner 1998). TDAS is efficient and well-studied theoretically, especially in cases where all dynamical variables can be observed and controlled simultaneously (Just, Bernard, Ostheimer, Reibold & Benner 1997).

In spatially extended media, the system variables are monitored only at a finite number of points, or spatially or temporally averaged variables are measured. Usually, the control signal is applied locally at a limited number of points or globally. In spite of these restrictions, there are many examples of successful control by TDAS in one-dimensional media (Bleich & Socolar 1996, Franceschini, Bose & Schöll 1999, Beck, Amann, Schöll, Socolar & Just 2002). In two- or three-dimensional systems, only a few examples for the stabilization of spatio-temporal patterns by TDAS are known (Schlesner et al. 2006, Schlesner, Zykov & Engel 2008, Lüthje, Wolff & Pfister 2001).

If the state of a whole system is denoted by $\mathbf{x}(t)$ and the variable that can be measured by $s(t)$, then the relation between the two is given by

$$s(t) = g[\mathbf{x}(t)], \tag{6.5}$$

where g is the function which describes the relation between both variables. To generate the control force, the temporal difference $s(t) - s(t - \tau)$ is used and for the delay time τ the period T of the periodic orbit $\xi(t)$ is chosen. Then the control force is given by

$$F(t) = K [s(t) - s(t - \tau)], \quad (6.6)$$

where K is a constant factor which determines the magnitude of the control force. If the UPO $\xi(t)$ is stabilized, the system $\mathbf{x}(t)$ as well as the variable $s(t)$ are periodic with the period T , which leads to the disappearance of the control force

$$F(t)|_{x=\xi} = K [g(\xi(t)) - g(\xi(t - \tau))] = 0. \quad (6.7)$$

This control method is known as time delay autosynchronization (TDAS) (Pyragas 1992) and was extended by Socolar to the so-called extended time delay autosynchronization (ETDAS) (Socolar et al. 1994). In contrast to TDAS ETDAS not only uses one period but any period is taken into account to generate the control force. To do so the memory factor R is introduced, which leads to

$$F(t) = K \sum_{\nu=0}^{\infty} R^{\nu} [s(t - \nu\tau) - s(t - (\nu + 1)\tau)] \quad (6.8)$$

$$= K [s(t) - s(t - \tau)] + RF(t - \tau). \quad (6.9)$$

So TDAS is a special case of ETDAS for $R = 0$.

For the stabilization of the spiral wave pattern the radius $r(t)$ can be used to generate the control force as done previously for PFC. In the framework of TDAS, the control force F is determined as:

$$F(t) = K [r(t) - r(t - \tau)] \quad (6.10)$$

and for ETDAS as

$$F(t) = K [r(t) - r(t - \tau)] + RF(t - \tau). \quad (6.11)$$

In the Oregonator model (2.1) and (2.2) the control force F is added to the fixed

background illumination ϕ_0 as for PFC:

$$\phi(t) = \phi_0 + F(t). \quad (6.12)$$

To stabilize an unstable periodic orbit with TDAS the time delay τ has to be equal to the period of the UPO. In our simulations we used the values for the rotation period of rigidly rotating spiral waves stabilized previously under PFC, but often the period is unknown. In this case, the branch of the UPO can be tracked by starting from the Hopf bifurcation where the periodic orbit becomes unstable and the period is known. By slight variation of the bifurcation parameter, the period changes slightly as well. So the period of the UPO T can be tracked by variation of the bifurcation parameter, here ϕ_0 (for the Oregonator model) and ϵ (for the FHN model).

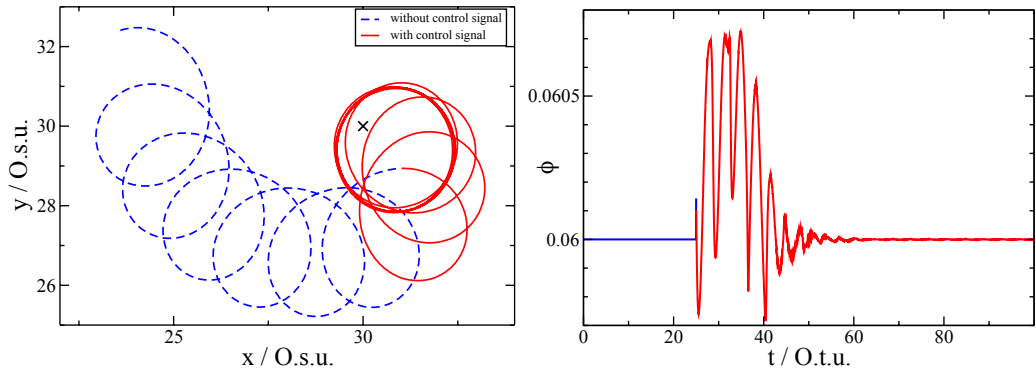


Figure 6.10: Stabilization of rigid rotation of a spiral wave applying TDAS with tip location defined from the u -field. Simulations performed with the Oregonator model (2.1) and (2.2), TDAS (6.10) and (6.12), parameter set O1, $\tau = 4.015$ O.t.u., $K = 0.001$, and $\phi_0 = 0.06$. (a) Trajectory of the spiral tip with and without feedback (dashed blue and full red line, respectively). The cross denotes the reference point. (b) Time evolution of the control parameter $\phi(t)$. Figure taken from (Schlesner et al. 2006)

One example of successful stabilization by TDAS is shown in Figure 6.10. The results are obtained by simulations with the Oregonator model (2.1) and (2.2), the control force (6.10) and (6.12), the parameter set O1, $\tau = 4.015$ O.t.u., $K = 0.001$, and $\phi_0 = 0.06$. As in Figure 6.2, the dashed line denotes the initial part of the simulation performed without control. After the control force is switched on at

$t = 25 \text{ O.t.u.}$, the spiral wave is forced into the regime of rigid rotation (full line). In contrast to PFC the center of rigid rotation differs from the chosen reference point, hence asymptotically the distance $r(t)$ is not a constant. Nevertheless, as with PFC, the control force vanishes in the stabilized regime because the actual distance $r(t)$ in Equation (6.10) oscillates with period $T \approx \tau$.

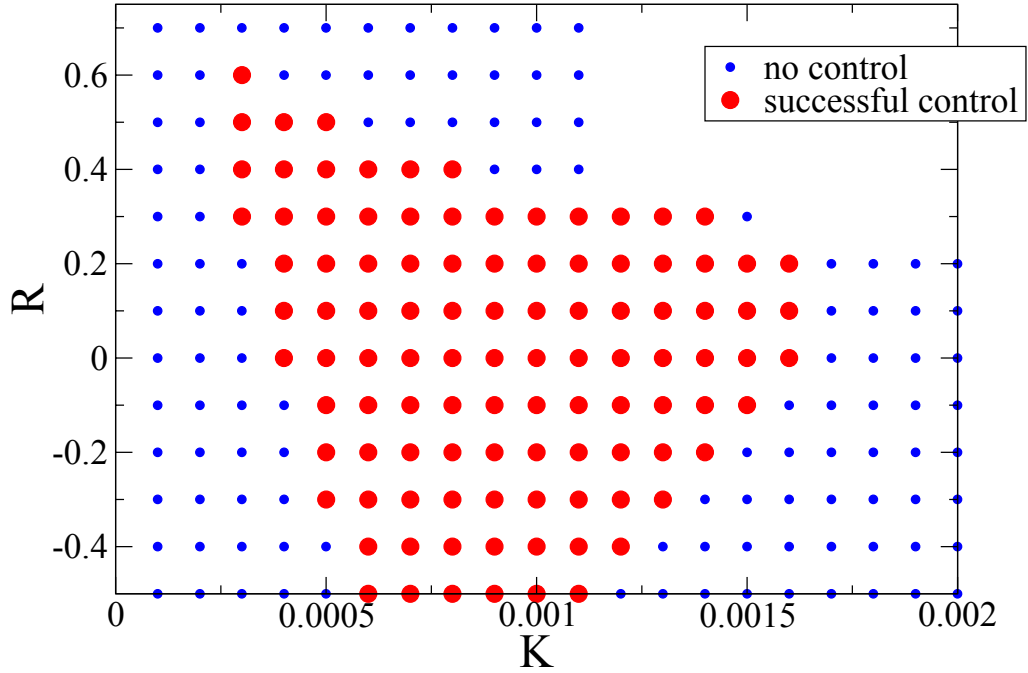


Figure 6.11: Control domain for ETDAS with tip location defined by the u -field. Simulations performed with the Oregonator model (2.1) and (2.2), ETDAS (6.11) and (6.12), and parameter set $O3$

In Figure 6.11 the control domain for ETDAS is depicted. The simulations are performed with the Oregonator model (2.1) and (2.2), the control force (6.11) and (6.12), and parameter set $O3$. The full red circles denote successful stabilization and the small blue dots denote failure of stabilization. By using ETDAS instead of TDAS the interval for K with successful stabilization is broadened, but only for a certain interval of memory factor R . Above a critical value of the memory factor R an additional bifurcation occurs and the stabilization fails.

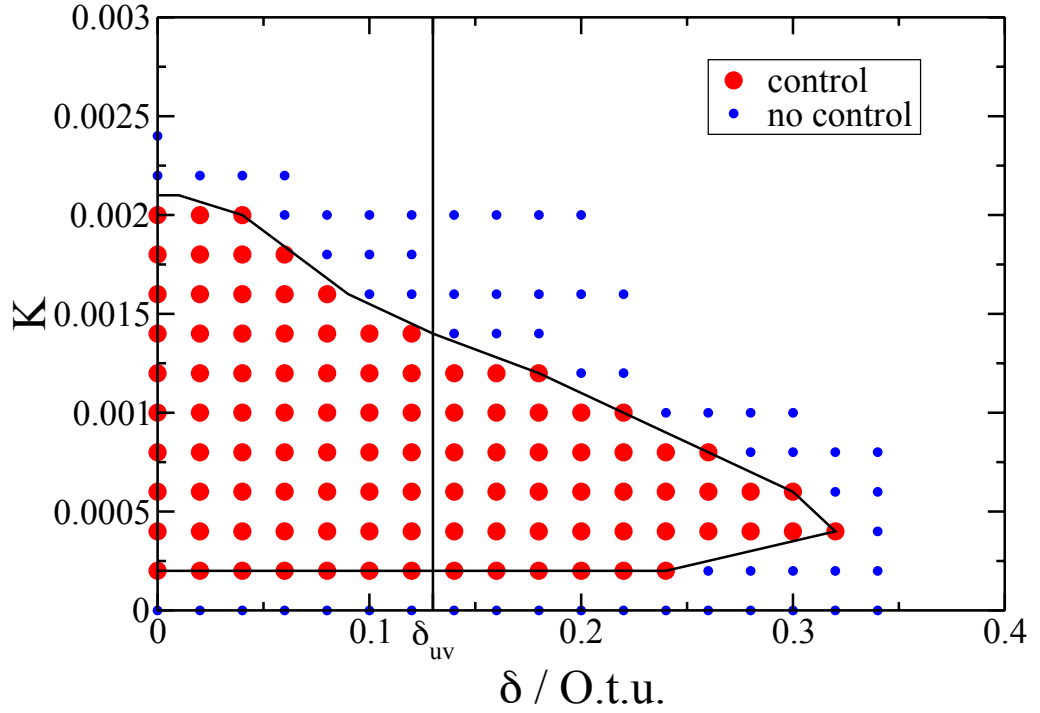


Figure 6.12: Control domain for TDAS with tip location defined by the u -field for the Oregonator model (2.1) and (2.2), TDAS (6.10) and (6.12), parameter set O1, $\phi_0 = 0.06$ and $\tau = 4.015 O.t.u.$. Full red circles denote successful stabilization; small blue dots denote failure of stabilization.

6.2.2 TDAS and control loop latency

To study the robustness of TDAS with respect to latency effects, we account for some latency time δ in the control loop replacing $F(t)$ in Equation (6.12) with $F(t - \delta)$. In Figure 6.12 the boundary of the control domain for the Oregonator model (2.1) and (2.2) subjected to TDAS is shown by the solid line. As for proportional feedback, the control domain shrinks with δ , but the critical latency δ_{cr} is larger. As $\delta_{cr} > \delta_{uv}$, it should be possible to stabilize rigid rotation with TDAS even when the tip coordinates are defined from the iso-concentration lines of the slower v -field. Our simulations confirmed this conjecture. For suitably chosen control strength, TDAS operates reliably as long as the effective latency $\delta + \delta_{uv}$ is smaller than the critical latency δ_{cr} , above which it breaks down.

6.3 Comparison of PFC and TDAS

So far we have demonstrated that both PFC and TDAS are able to stabilize rigid rotation of spiral waves in the meandering regime. Now we will summarize specific advantages and disadvantages of these two control methods.

In principle, the reference radius r_0 must be known to apply PFC. However, we can add simple relaxational dynamics for r_0 according to

$$\frac{dr_0}{dt} = \frac{1}{\epsilon'} (r(t) - r_0) \quad (6.13)$$

to the model (2.1) and (2.2) with feedback (6.1). Provided that r_0 changes on a characteristic time scale much larger than the rotation period of the spiral wave ($\epsilon' \gg T$), this additional equation ensures that r_0 is adapted automatically during feedback-mediated stabilization. In the limit $t \rightarrow \infty$, $r_0(t)$ approaches the previously unknown value r_0 . In all cases we have checked that the feedback algorithm (6.1) with the obtained value for r_0 as initial condition does not change the UPO.

Before we can apply TDAS, we have to identify the period of the UPO to be stabilized, i.e. the rotation period of the spiral wave. Again, τ can be determined by solving an additional equation equivalent to (6.13) when the control is applied. For the stabilization of rigidly rotating spiral waves, the determination of τ turned out to be numerically more intricate than the determination of r_0 .

As a comparison we present the control diagrams for PFC and TDAS in Figure 6.13, which do not overlap for the given value of the parameter ϕ_0 . Feedback strengths required for successful stabilization are smaller with TDAS. In return, the control range in K is larger for PFC. The possible range of control loop latencies was found to be larger for TDAS which in this respect turns out to be more robust than PFC. Therefore, we succeeded in stabilizing rigid rotation with TDAS using information from the slow v -field in calculating the tip coordinates, but we failed when applying PFC due to a control loop latency which was beyond the control boundary.

Note that in PFC the core center of the stabilized rigidly rotating spiral wave always coincides with the arbitrarily chosen reference point. In this respect, PFC is capable of moving a spiral core to a desired position in the medium.

The control force vanishes in PFC only if $r(t)$ asymptotically approaches a con-

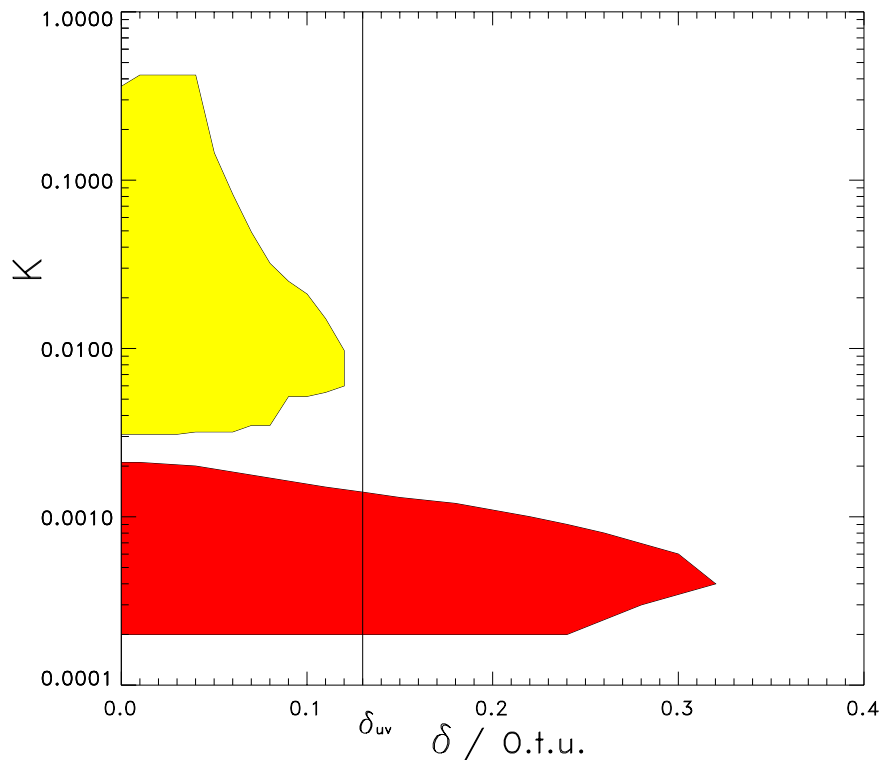


Figure 6.13: (Color online) Control domains for proportional feedback (brighter gray, yellow online) and the TDAS (darker gray, red online) for the Oregonator model (2.1) and (2.2), parameter set O1, $\phi_0 = 0.06$ and $\tau = 4.015$ *O.t.u.*. Half-logarithmic plot. Figure taken from (Schlesner et al. 2006)

stant value r_0 characteristic for rigid rotation. Contrastingly in TDAS, periodic oscillations of $r(t)$ are allowed in the stabilized state. Hence, it might be possible to stabilize more complicated rotational regimes of spiral waves with TDAS, for example: meandering spiral waves in the hypermeandering regime.

7 Control of spiral wave location by detector–line feedback

7.1 Introduction to feedback–induced resonant drift of spiral waves

Spatial or temporal modulation of excitability is actively used in many studies in order to clarify fundamental features of spiral wave dynamics and to create the basis for possible applications (Agladze, Davydov & Mikhailov 1987, Schütze, Steinbock & Müller 1992, Markus, Nagy-Ungvarai & Hess 1992, Fast & Pertsov 1992, Steinbock, Zykov & Müller 1993, Braune & Engel 1993, Sendina-Nadal, Alonso, Pérez-Munuzuri, Gómez-Gesteira, Pérez-Villar, Ramírez-Piscina, Casademunt, Sancho & Sagués 2000, Wu, Gao & Ying 2013). In particular, resonant drift of spiral waves induced by periodic temporal modulation of excitability has been proven to be a highly generic phenomenon in excitable media (Davydov, Zykov & Mikhailov 1991, Mantel & Barkley 1996, Sandstede, Scheel & Wulff 1999). Very promising control strategies rely on feedback–mediated parametric modulation. In this case, the modulation period always coincides exactly with the actual rotation period of the spiral wave. Moreover, when under external periodic forcing, the direction of resonant drift depends on the initial orientation of the spiral wave and the direction of feedback-induced resonant drift is solely determined by the location of the spiral wave core. Consequently, when using an Archimedean approximation for the spiral wave shape, the underlying reaction-diffusion model supplemented with terms accounting for the feedback loop can be reduced to an autonomous dynamical system for the coordinates of the spiral core. The corresponding velocity field of feedback-mediated resonant drift simplifies the analysis considerably. Attractors of this velocity field depend on experimentally accessible parameters in the control loop such as the

feedback strength or the delay time (Zykov & Engel 2004).

The most elaborate feedback algorithm to control spiral waves is so-called one-channel feedback (Biktashev & Holden 1994, Grill et al. 1995, Karma & Zykov 1999). In this case, a short perturbation of excitability is generated each time a spiral wave front passes through a particular measuring point of the medium, inducing the drift of the spiral wave core along a circle centered at the measuring point. Here we report experimental and theoretical results for a novel feedback algorithm which assumes that a short perturbation is generated each time a spiral wave front is tangent to a given curve or touches its open end. These results are supplemented and confirmed by numerical simulations of the underlying Oregonator model as well as the FitzHugh–Nagumo model.

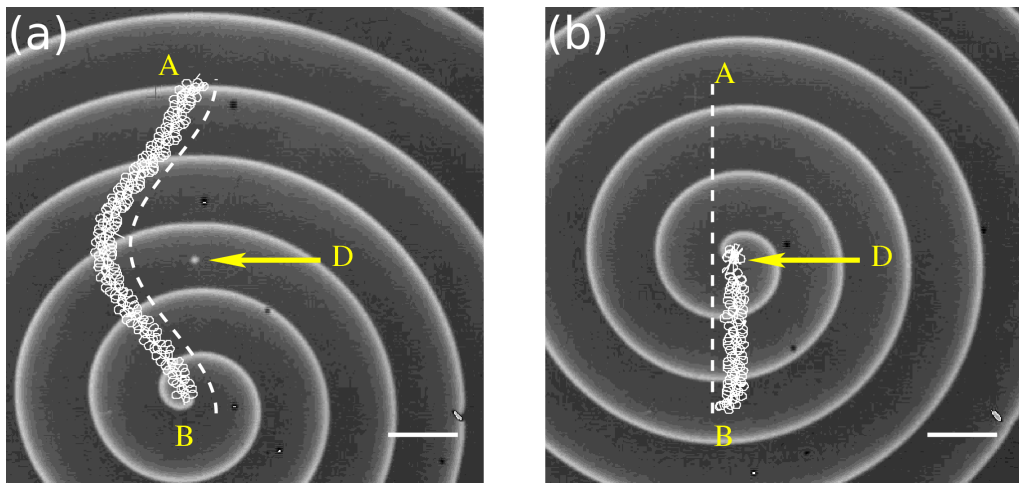


Figure 7.1: Feedback-induced drift of a spiral wave between points A and B in the presence of a defect D ($\tau = 0.71T_\infty$). (a) A curved detector allows for bypassing of the defect. (b) Capture of the spiral wave by the defect because the core trajectory comes to close to it. Figures taken from (Schlesner, Zykov, Brandstädter, Gerdes & Engel 2008)

The proposed feedback algorithm can be applied to shift the spiral wave core from a given point A to a desired position at another point B along a curved detector. This could be important in media with some defects. Indeed, let us assume that the direct route between A and B is blocked by a defect D, as shown in Figure 7.1. A spiral core moving along a straight line will get caught at the defect (see Figure 7.1(b)). However, applying a curved detector as illustrated in Figure 7.1(a), we can shift the

spiral wave core from A to B, avoiding its capture by the defect. In these experiments the controlling pulses are generated with a time delay τ after the moment when the spiral wave front touches the detector. This allows us to reduce the distance between the attractor line and the detector, and makes the control much more precise. This point is discussed in more detail below.

In this chapter our aim is to move the core of a freely rotating spiral wave as fast as possible along a chosen trajectory to any desired position. At first we present results for the so-called single-pulse feedback method, which are obtained by studying this method theoretically and numerically as well as experimentally. Unfortunately, the speed of the moving core is limited by an instability. To suppress this instability we proposed extending the feedback method to a double-pulse method. At a given control amplitude, this method allows us to move the spiral wave core faster than by using the single-pulse method. A more detailed comparison between both methods is given at the end of this chapter.

Primarily the single-pulse method is introduced and studied in the next section. A theoretical description of the core moving under this feedback is elaborated, followed by a numerical and experimental verification of the findings.

7.2 Theoretical description of spiral waves under detector–line feedback

As mentioned above, we studied a feedback method which uses a line (straight or curved) detector. Each time a wave front is tangent to the detector, a short pulse with a fixed duration is generated. In our experiments the pulse is a light pulse which changes the excitability of the medium, modifies the unperturbed trajectory of the spiral tip, and induces a shift of the spiral core. Due to the rotation of the spiral, a periodic (resonant) sequence of such pulses is generated and the individual shifts accumulate over time, resulting in a spiral wave drift. The resulting feedback signal is depicted in Figure 7.2. In our experiments the feedback signal is the light intensity. So I_0 is the background illumination and A is the additional intensity of the light pulse. The duration of the light pulse is fixed, but the interval between two pulses depends on the spiral wave and its motion. Normally these intervals are very uniform.

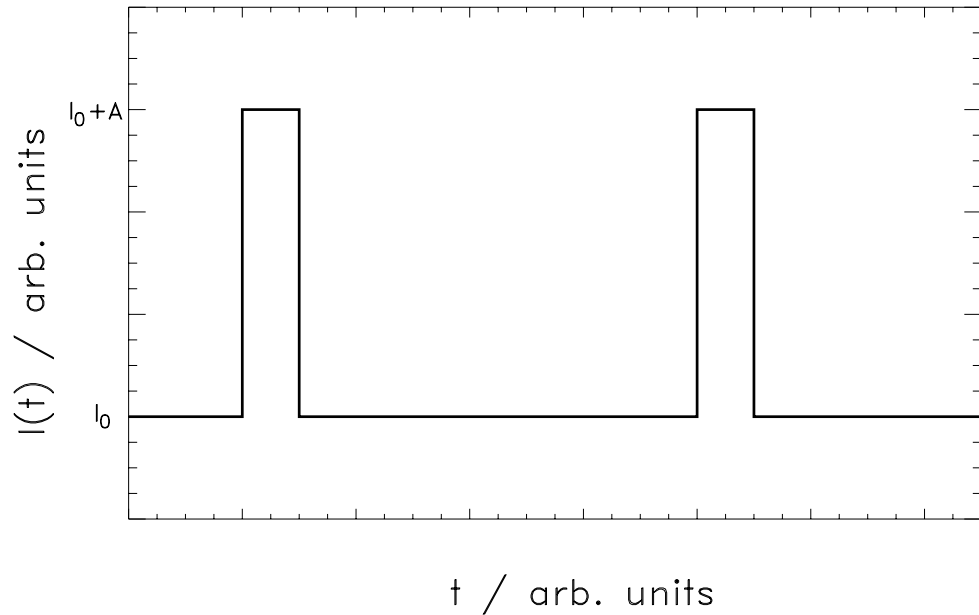


Figure 7.2: Feedback signal in relation to the time.

7.2.1 Single–pulse feedback

Our aim is now to elaborate a theoretical description of the core moving without restriction to a special system. For the description, we will use only general characteristics of spiral waves.

A very important property of a spiral wave is that its rotation frequency and shape do not depend on how this spiral has been created. The shape of a rigidly rotating spiral can be rather well approximated by an Archimedean spiral as suggested by A. Winfree (Winfree 1972). Thus, in a polar coordinate system (r, Θ) the spiral shape is given as

$$\Theta(r, t) = \Theta_0 - \frac{2\pi}{\lambda_0} r + \omega_0 t, \quad (7.1)$$

where Θ_0 , λ_0 and ω_0 determine the initial orientation, the angular velocity and the wavelength of the spiral, respectively. Recent computations performed with the Oregonator model (Karma & Zykov 1999) and experiments with the BZ reaction (Zykov, Kheowan, Rangsiman & Müller 2002) also confirm that an Archimedean

spiral provides a suitable approximation of the wave front except for a relatively small region of radius $r_A \ll \lambda_0$ near the rotation center. Moreover, even the shape of a slightly meandering spiral waves exhibits only small oscillations near an Archimedean form and the amplitude of these oscillations vanishes very quickly with r (Barkley et al. 1990). Therefore the Archimedean spiral approximation is used below to obtain the drift velocity field which determines the feedback-mediated dynamics of a spiral wave near a straight line detector.

Figure 7.3 illustrates an Archimedean spiral rotating around the point (x_i, y_i) . The straight line detector is located along the line $x = 0$. Each time a spiral wave front touches the detector tangentially, a short control pulse of amplitude A is applied globally to the whole medium immediately or with a time delay τ .

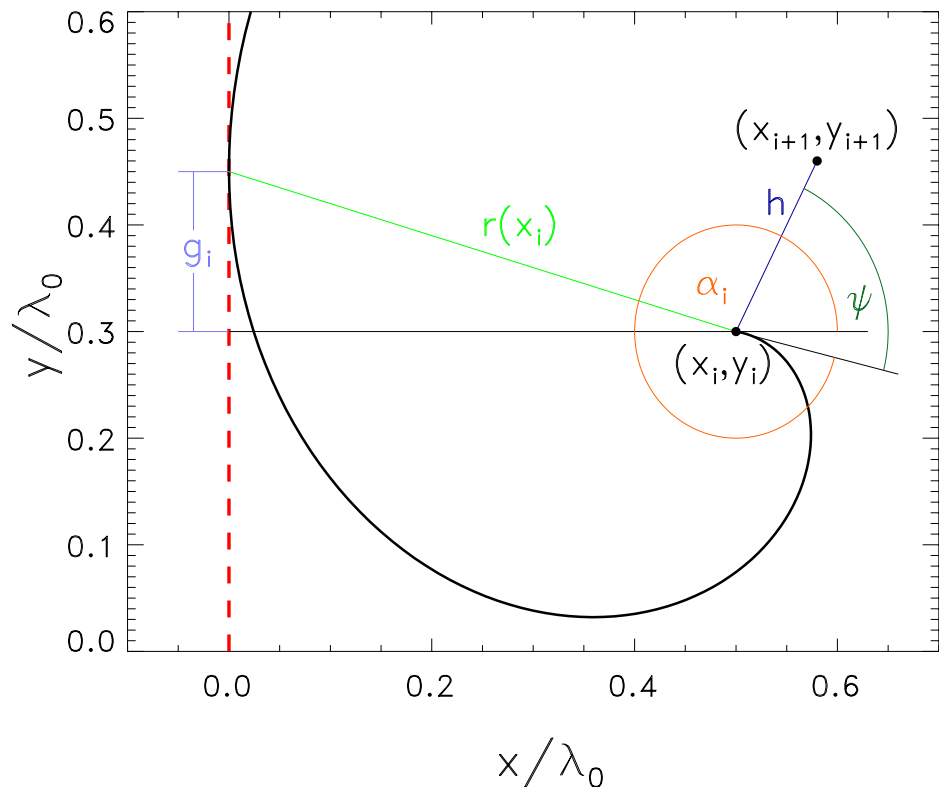


Figure 7.3: Archimedean spiral (thick black line) at the moment when it touches the line detector (dashed red line). Figure taken from (Schlesner, Zykov, Brandstädter, Gerdes & Engel 2008).

The perturbation leads to a shift of the core center. Its new location is specified

as

$$x_{i+1} = x_i + h \cos(\gamma_i) \quad (7.2)$$

$$y_{i+1} = y_i + h \sin(\gamma_i), \quad (7.3)$$

where h is the magnitude of the displacement and the angle γ_i specifies its direction.

Due to rotational symmetry, the direction of the shift induced depends on the spiral orientation at the moment, when the pulse is applied. The spiral orientation is specified by the angle α_i plus an additional angle $\omega_0\tau$, which results from spiral rotation with a velocity ω_0 during the time delay τ . The angle ψ between the orientation of the spiral wave and the direction of the induced displacement is a characteristic parameter which depends on both the excitability of the medium and the perturbation applied (Karma & Zykov 1999). Therefore the angle γ_i in Equations (7.2) and (7.3) reads

$$\gamma_i = \alpha_i + \psi + \omega_0\tau, \quad (7.4)$$

A pure geometrical consideration shows that the angle α_i can be expressed as

$$\alpha_i = \pi + \frac{2\pi}{\lambda_0} r(x_{i-k}) - \arctan\left(\frac{g_{i-k}}{x_{i-k}}\right), \quad (7.5)$$

where

$$r(x) = x \sqrt{0.5 + \sqrt{0.25 + \left(\frac{\lambda_0}{2\pi x}\right)^2}}, \quad (7.6)$$

and

$$g_i = \frac{\lambda_0 x_i}{2\pi r(x_i)}. \quad (7.7)$$

The integer k depends on the total delay time τ_Σ in the feedback loop. One factor of the total delay is the time delay τ in the feedback loop while another one depends on the spiral location and can be calculated as $\alpha(x_i)/\omega_0$ (Zykov et al. 2002).

If we assume that the perturbation pulses produce negligibly small changes in the angular velocity and the spiral shape, the system of Equations (7.2)-(7.7) represents

an iterated map describing the dynamics of the core center. The drift velocity field corresponding to the iterated map (7.2)-(7.7) is shown in Figure 7.4.

It is important to mention that according to Equations (7.4)-(7.7) the direction of the displacement γ_i depends only on the distance between the line detector and the spiral core center x_i and does not depend on the coordinate y_i . This is consistent with the attractor structure observed experimentally and shown later in Figure 7.15.

Iterated map for the limit $x_i \gg \lambda_0$

If the spiral core is located relatively far away from the detector ($x_i \gg \lambda_0$), then due to $r(x_i) \approx x_i$ and $\arctan\left(\frac{\lambda_0}{2\pi x_{i-k}}\right) \approx 0$ the iterated map (7.2)-(7.7) can be simplified to the following form

$$x_{i+1} = x_i + h \cos\left(\omega_0\tau + \pi + \frac{2\pi}{\lambda_0}x_{i-k} + \psi\right), \quad (7.8)$$

$$y_{i+1} = y_i + h \sin\left(\omega_0\tau + \pi + \frac{2\pi}{\lambda_0}x_{i-k} + \psi\right). \quad (7.9)$$

The first equation of this map is independent of the second one and exhibits steady state x_s satisfying the simple condition

$$x_s = x_s + h \cos\left(\omega_0\tau + \pi + \frac{2\pi}{\lambda_0}x_s + \psi\right) \quad (7.10)$$

$$\Leftrightarrow 0 = \cos\left(\omega_0\tau + \pi + \frac{2\pi}{\lambda_0}x_s + \psi\right). \quad (7.11)$$

This condition can be transformed into an explicit analytic expression for x_s

$$\left(m + \frac{1}{2}\right)\pi = \omega_0\tau + \pi + 2\pi\frac{x_s}{\lambda_0} + \psi \quad (7.12)$$

$$\Leftrightarrow \frac{x_s}{\lambda_0} = \frac{m}{2} - \frac{1}{4} - \underbrace{\frac{\omega_0\tau}{2\pi}}_{=\frac{\tau}{T_0}} - \frac{\psi}{2\pi}, \quad (7.13)$$

where m is a positive integer and $T_0 = 2\pi/\omega_0$ is the rotation period of the spiral.

This steady state corresponds to a resonance attractor, which is a line parallel to the straight line detector. In accordance with Equation (7.9), each pulse shifts the spiral center along this line by a distance $\Delta y = h$.

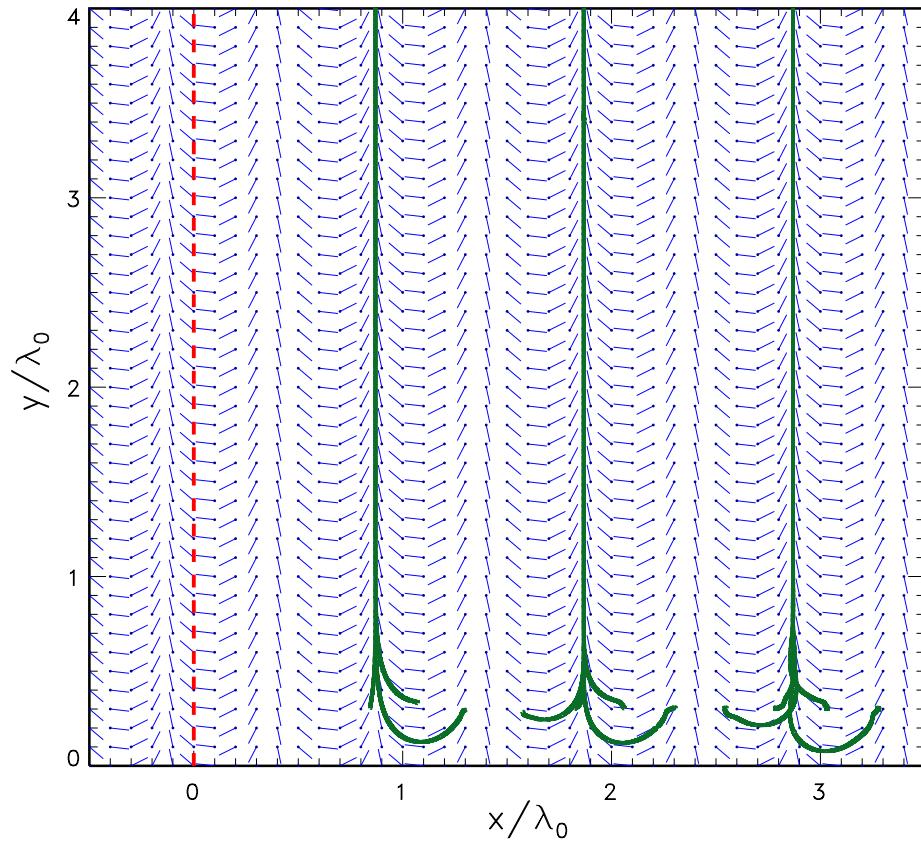


Figure 7.4: Velocity field of spiral wave drift (blue bars) near a line detector (dashed red line) calculated from the iterated map (7.2)-(7.7) with $\tau = 0$ and $\psi = 2.39$. Solid lines show trajectories of spiral core center obtained from numerical simulations with the Oregonator model (2.1) and (2.2) with parameter set O3. Figure taken from (Schlesner, Zykov, Brandstädter, Gerdes & Engel 2008).

To study the stability of the resonance attractor we use the ansatz $x_i = x_s + \delta x_i$ and analyze the development over time of the deviation δx from the steady state x_s :

$$x_s + \delta x_{i+1} = x_s + \delta x_i + f(x_{i-k}). \quad (7.14)$$

This leads to

$$\delta x_{i+1} - \delta x_i = f(x_{i-k}) \approx \underbrace{f(x)|_{x=x_s}}_{=0} + f'(x)|_{x=x_s} \delta x_{i-k} \quad (7.15)$$

$$= -h \sin \left(\omega_0 \tau + \pi + 2\pi \frac{x_s}{\lambda_0} + \psi \right) \frac{2\pi}{\lambda_0} \delta x_{i-k} \quad (7.16)$$

$$= -\frac{2\pi h}{\lambda_0} \sin \left(\left(m + \frac{1}{2} \right) \pi \right) \delta x_{i-k} \quad (7.17)$$

$$= -\frac{2\pi h}{\lambda_0} (-1)^m \delta x_{i-k} \quad (7.18)$$

When that δx_{i+1} , δx_i and δx_{i-k} are all positive or all negative, the term $-\frac{2\pi h}{\lambda_0} (-1)^m$ determines whether the deviation δx grows or shrinks. If m is even, this term is negative, which means that the deviation shrinks, while where m is odd, the steady state x_s is unstable.

However, especially for greater values of k , δx_{i-k} can be located on the other side of the attractor. In this case and when m is even, the attractor still attracts the spiral wave tip but it is also possible that the attractor is no longer stable and that the tip oscillates around x_s . This case is shown later, after the iterated map for the general case is introduced.

Iterated map for the general case

In the general case of an arbitrary value of x_i , one can obtain the iterated map

$$\begin{aligned} x_{i+1} &= x_i + h \cos(\gamma_i) \\ &= x_i - h \cos \left[\omega_0 \tau + \frac{2\pi}{\lambda_0} r(x_{i-k}) + \psi - \arctan \left(\frac{g_{i-k}}{x_{i-k}} \right) \right] \end{aligned} \quad (7.19)$$

$$\begin{aligned} y_{i+1} &= y_i + h \sin(\gamma_i) \\ &= y_i - h \sin \left[\omega_0 \tau + \frac{2\pi}{\lambda_0} r(x_{i-k}) + \psi - \arctan \left(\frac{g_{i-k}}{x_{i-k}} \right) \right] \end{aligned} \quad (7.20)$$

from Equations (7.2)-(7.7). This yields to the implicit expression for the steady state values x_s

$$0 = \cos \left[\omega_0 \tau + \frac{2\pi}{\lambda_0} r(x_s) + \psi - \arctan \left(\frac{g_s}{x_s} \right) \right] \quad (7.21)$$

$$\Leftrightarrow \left(m + \frac{1}{2} \right) \pi = \omega_0 \tau + \frac{2\pi}{\lambda_0} r(x_s) + \psi - \arctan \left(\frac{g_s}{x_s} \right), \quad (7.22)$$

$$\Leftrightarrow 0 = \frac{m}{2} + \frac{1}{4} - \underbrace{\frac{\omega_0 \tau}{2\pi}}_{\frac{\tau}{T_0}} - \frac{r(x_s)}{\lambda_0} - \frac{\psi}{2\pi} + \arctan \left(\frac{g_s}{x_s} \right) \quad (7.23)$$

where $r(x_s)$ is determined by Equation(7.6). Note that this expression can only be applied when the Archimedean approximation is valid, i.e. $x_i > r_A$. Within this range of x_i the difference between x_s obtained numerically from Equation (7.22) and from the approximate Equation(7.13) is rather small.

By using

$$f(x_{i-k}) = -h \cos \left[\omega_0 \tau + \frac{2\pi}{\lambda_0} r(x_{i-k}) + \psi - \arctan \left(\frac{\lambda_0}{2\pi r(x_{i-k})} \right) \right] \quad (7.24)$$

the iterated map for x_i , (7.19) can be written as

$$x_{i+1} = x_i + f(x_{i-k}). \quad (7.25)$$

To study the stability of steady states x_s , we again use the ansatz $x_i = x_s + \delta x_i$, which leads to

$$\delta x_{i+1} = \delta x_i + f(x_s + \delta x_{i-k}). \quad (7.26)$$

With the Taylor–expansion around x_s and neglecting terms of an order higher than

one, we obtain

$$\delta x_{i+1} - \delta x_i \approx \underbrace{f(x_s)}_{=0} + f'(x)|_{x=x_s} \delta x_{i-k} \quad (7.27)$$

$$= \frac{2\pi h}{\lambda_0} \underbrace{\sin\left(\omega_0 \tau + \frac{2\pi}{\lambda_0} r(x_s) + \psi - \arctan\left(\frac{\lambda_0}{2\pi r(x_s)}\right)\right)}_{=\sin\left((m+\frac{1}{2})\pi\right)=(-1)^m} \quad (7.28)$$

$$\cdot \underbrace{\left(1 + \frac{1}{4\pi^2 \frac{r(x_s)^2}{\lambda_0^2} + 1}\right)}_{\approx 1 \text{ for } r(x) \gg \lambda_0} \frac{\partial r}{\partial x} \Big|_{x=x_s} \delta x_{i-k} \quad (7.29)$$

$$= \underbrace{(-1)^m \frac{2\pi h}{\lambda_0} \frac{\partial r}{\partial x} \Big|_{x=x_s}}_{=: -H} \delta x_{i-k}. \quad (7.30)$$

So by performing linear stability analysis of the steady states specified by Equation (7.13), we get the iterated map for the deviations δx_i

$$\delta x_{i+1} - \delta x_i + H \delta x_{i-k} = 0. \quad (7.31)$$

In general, the value H depends on the spiral location. However, under the approximation $r(x_i) \approx x_i$ this value reads

$$H = \frac{2\pi h}{\lambda_0} (-1)^m. \quad (7.32)$$

To check the validity of this approximation we calculated $r'(x)$:

$$r'(x) = \sqrt{\frac{1}{2} + \sqrt{\frac{1}{4} + \left(\frac{\lambda_0}{2\pi x}\right)^2}} \quad (7.33)$$

$$- \frac{\lambda_0^2}{8\pi^2 x^2} \left(\frac{1}{2} + \sqrt{\frac{1}{4} + \left(\frac{\lambda_0}{2\pi x}\right)^2}\right)^{-\frac{1}{2}} \left(\frac{1}{4} + \left(\frac{\lambda_0}{2\pi x}\right)^2\right)^{-\frac{1}{2}} \quad (7.34)$$

and studied r' in dependence on x/λ_0 . In Figure 7.5 r and r' are plotted in relation to x . Since r deviates from x and r' from 1 significantly only for small values of x ($x \ll \lambda_0$), the approximation made above is valid almost everywhere, except when

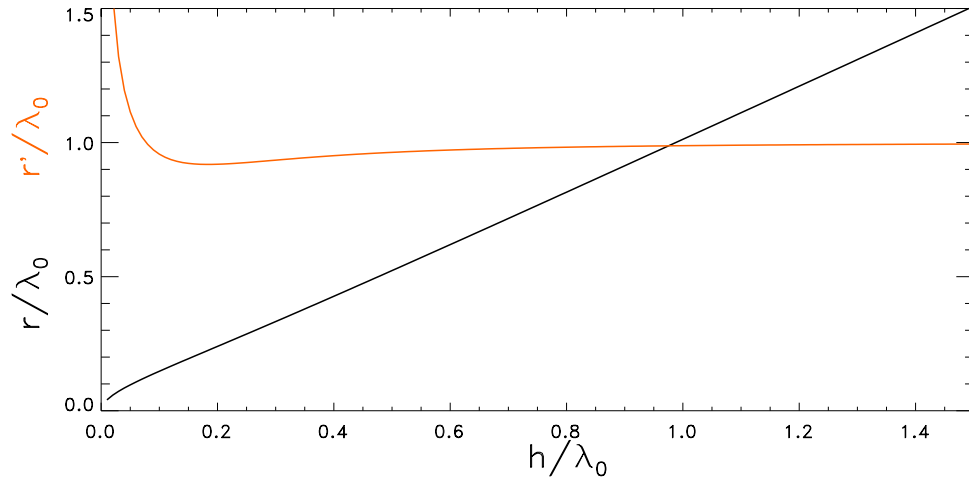


Figure 7.5: r and r' in dependence on x . Only for small values of x ($x \ll \lambda_0$), r deviates from x and r' from 1.

the spiral tip is located in the vicinity of the detector line (i.e. if the distance to the detector is less than one wavelength λ_0).

Substitution of the ansatz $\delta x_i = \lambda^i$ into Equation (7.31) yields the characteristic equation for the eigenvalues

$$\lambda^{k+1} - \lambda^k + H = 0. \quad (7.35)$$

A steady state of the iterated map (7.8) is stable under the condition $|\lambda| < 1$. Generally speaking, the characteristic Equation (7.35) has $k + 1$ roots, which can be found numerically for a given H . For $H = 0$ there are k roots $\lambda = 0$ and one root is located at $\lambda = 1$. For $H < 0$ this root is located outside the unit circle, indicating an instability. With growing H this root moves inside the unit circle. At first, the other roots remain in the vicinity of the point $\lambda = 0$. However, under critical conditions two complex conjugated roots cross the unit circle, resulting in the Neimark bifurcation.

The critical value H_{cr} of the dimensionless shift H at the Neimark bifurcation can be obtained analytically. To this end, one should take into account that at the bifurcation point the eigenvalue λ can be written as

$$\lambda = \cos \beta + i \sin \beta. \quad (7.36)$$

From Equation (7.35) we obtain two equations for the real and the imaginary parts

$$2 \cos \left(\frac{2k+1}{2} \beta \right) \sin \left(\frac{\beta}{2} \right) = 0, \quad (7.37)$$

$$-2 \sin \left(\frac{2k+1}{2} \beta \right) \sin \left(\frac{\beta}{2} \right) + H_{cr} = 0. \quad (7.38)$$

Positive values of H_{cr} correspond to the case $\cos \left(\frac{2k+1}{2} \beta \right) = 0$. Substitution of this condition into Equation (7.38) yields

$$H_{cr} = 2 \sin \left[\frac{\pi (4l+1)}{2(2k+1)} \right], \quad (7.39)$$

$$\beta = \frac{\pi (4l+1)}{2k+1}. \quad (7.40)$$

The integer l specifies the number of the Neimark bifurcation starting with $l = 0$ for the first bifurcation.

The expression obtained for H_{cr} allows us to estimate critical values for the magnitude h of the displacement induced by a single pulse. Approximate Equation (7.32) gives

$$\frac{h_{cr}(k)}{\lambda_0} \approx \frac{1}{\pi} \sin \left(\frac{\pi}{2(2k+1)} \right) \quad (7.41)$$

The exact implicit expression for value h_{cr} follows from Equations (7.22) and (7.4)-(7.7). It reads

$$\frac{h_{cr}(k)}{\lambda_0} \left[1 + \frac{1}{4\pi^2 \frac{r^2(x_s)}{\lambda_0^2} + 1} \right] \frac{\partial r}{\partial x} \Big|_{x=x_s} = \frac{1}{\pi} \sin \left(\frac{\pi}{2(2k+1)} \right). \quad (7.42)$$

For odd values of m the coefficient H determined by Equation (7.32) is negative. This corresponds to unstable steady states separating basins of attraction for stable steady states specified by even values of m (c.f. Figure 7.4). For $0 < h < h_{cr}(k)$ these steady states describe the spiral drift along straight lines parallel to the detector as shown in Figure 7.6 (compare Figure 7.15). However, the stability of this linear drift depends on k , which characterizes the total time delay τ_Σ . The value of k remains constant within the basin of attraction corresponding to an even value of

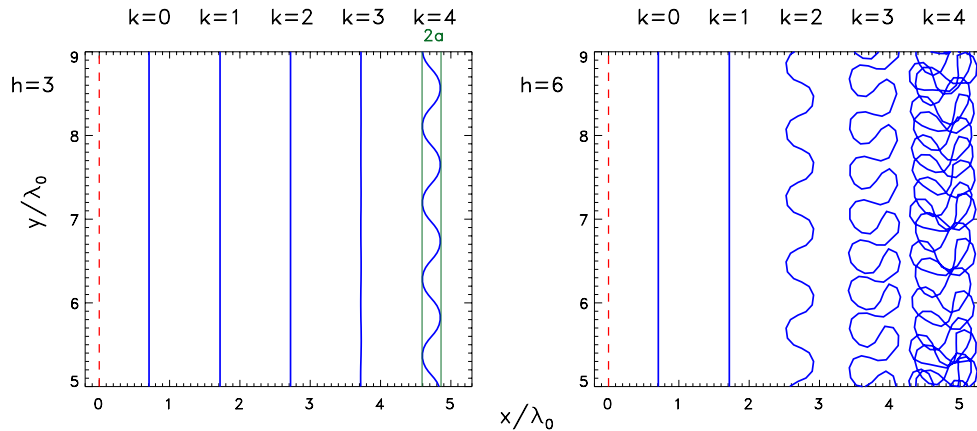


Figure 7.6: Trajectories of the spiral core (without transients) for different initial positions relative to the line detector (placed at $x = 0$) calculated from the iterated map (7.2)-(7.7). The shift per pulse h in the right figure was chosen twice as large as in the left one. Figures taken from (Schlesner, Zykov, Brandstädter, Gerdes & Engel 2008)

m. In accordance with Equation (7.13) the explicit expression for k reads

$$k = \left[\frac{\tau_\Sigma}{T_0} \right] = \left[\frac{\tau}{T_0} + \frac{x_i}{\lambda_0} + \frac{\psi}{2\pi} + \frac{1}{4} \right], \quad (7.43)$$

where $[Z]$ denotes the largest integer smaller than Z . For an arbitrarily chosen $h > 0$ the stability of a steady state is broken if k becomes larger than some critical value. This situation is illustrated in Figure 7.6. When $h = 3$ is fixed, the instability in the linear drift first appears for $k = 4$. For $h = 6$ the instability appears earlier, already at $k = 2$, and the trajectories of the spiral core become more and more complicated for increasing values of k .

The predicted instability restricts the average drift velocity of the spiral wave as illustrated in Figure 7.7. The linear increase of the drift velocity stops at the bifurcation point and is replaced by a fast drop in the drift velocity. The maximum drift velocity corresponds exactly to the bifurcation point determined by Equation (7.42). The approximate values of h_{cr} obtained from Equation (7.41) for different k correspond to the blue lines depicted in Figure 7.7. These analytical predictions are in good agreement with the numerical results obtained from the iterated map (7.2)-(7.7).

In Figure 7.6, the amplitude a of the deviation of the core center movement from

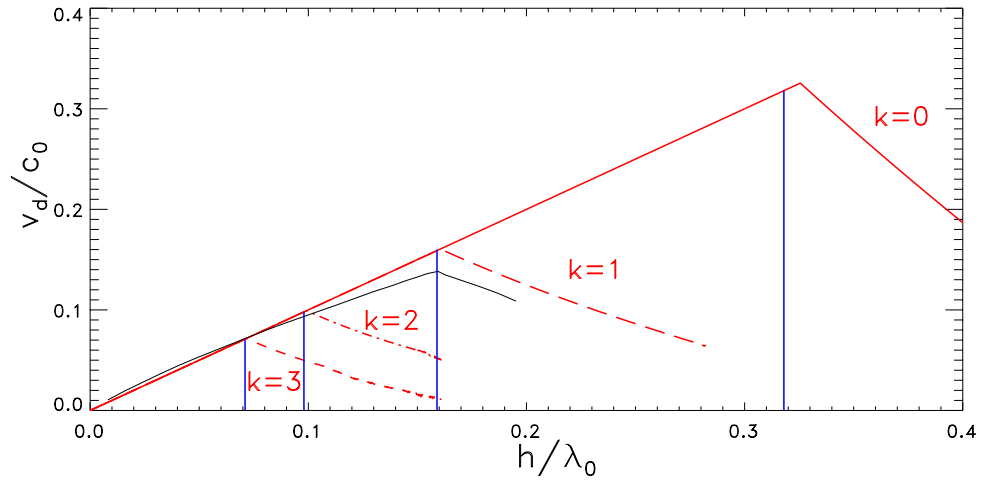


Figure 7.7: Average drift velocity in y -direction in dependence on the two bifurcation parameters shift per pulse h and on rank of the attractor k . Red curves represent numerical data obtained from the iterated map (7.2)-(7.7) for different values of k . Blue lines correspond to the approximated values of h_{cr} specified by Equation (7.41). Black curve shows numerical results obtained from the Oregonator model (2.1) and (2.2) with parameter set O3 for the attractor with $k = 1$. Figure taken from (Schlesner, Zykov, Brandstädter, Gerdes & Engel 2008)

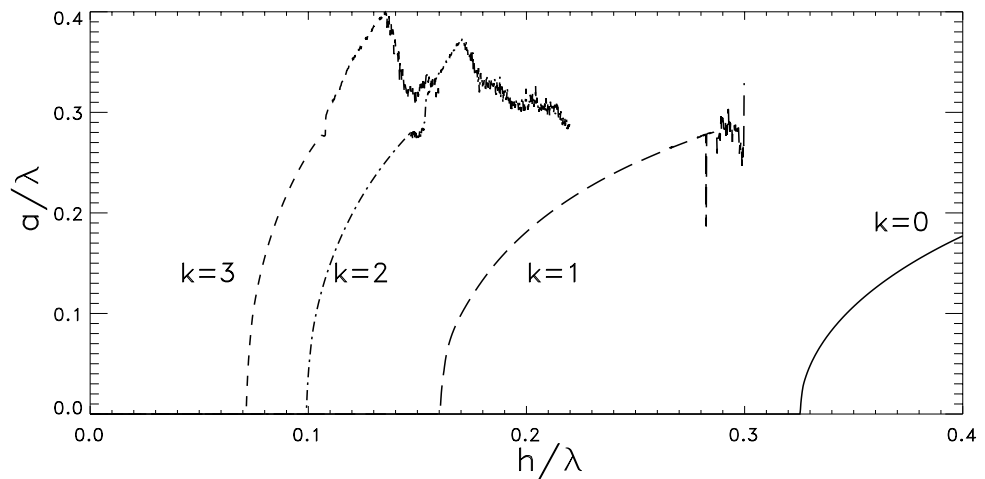


Figure 7.8: Amplitude a of the deviation of the core center movement from the steady state for different values of h calculated from the iterated map (7.2)-(7.7).

the steady state is depicted for $h = 3$ and $k = 4$. The distance between the two green lines is equal to $2a$. After the steady state becomes unstable, this amplitude a increases with increasing h . This dependency is shown in Figure 7.8 for different values of k , where the square root shape of this curve is easily recognizable.

7.2.2 Double–pulse feedback

To increase the drift velocity in the presence of feedback control, we proposed generating one additional negative pulse, delayed with respect to the positive one. In Figure 7.9 the dependence of time on the feedback parameter $I(t)$ is illustrated. First, a single positive pulse is generated as discussed above. Then a negative pulse is generated between two positive ones. For example for $p = 0.5$ a negative pulse is generated after a half of the rotation period of a spiral wave. This negative pulse causes a displacement of the core center in the opposite direction to the displacement induced by the positive pulse. However after half of the rotation period, the orientation of the spiral wave is turned by 180 degrees and thus, the negative pulse applied at this instant leads to a displacement in approximately the same direction as that induced by the previous positive pulse.

The iterated map for double-pulse feedback is similar to Equations (7.2) and (7.3), but includes additional terms describing the effect of the negative pulse

$$x_{i+1} = x_i + h \cos(\gamma_i) - h \cos(\omega_0\tau + \beta_i + \psi), \quad (7.44)$$

$$y_{i+1} = y_i + h \sin(\gamma_i) - h \sin(\omega_0\tau + \beta_i + \psi). \quad (7.45)$$

Here β_i is the angle of the spiral orientation at the instant when the negative pulse is applied. It is assumed that each negative pulse induces a displacement $-h$. Since a constant angular velocity of a spiral is assumed, the angle β_i is given by

$$\beta_i = \alpha_i + p(\alpha_i - \alpha_{i-1}) + 2\pi p. \quad (7.46)$$

Generally speaking, the value α_i is determined by Equation (7.4). To simplify the following analysis we consider the case $x_i \gg \lambda_0$ that gives $r(x_i) = x_i$ and corresponds to the iterated map Equations (7.8) and (7.9). Thus, Equation (7.44)

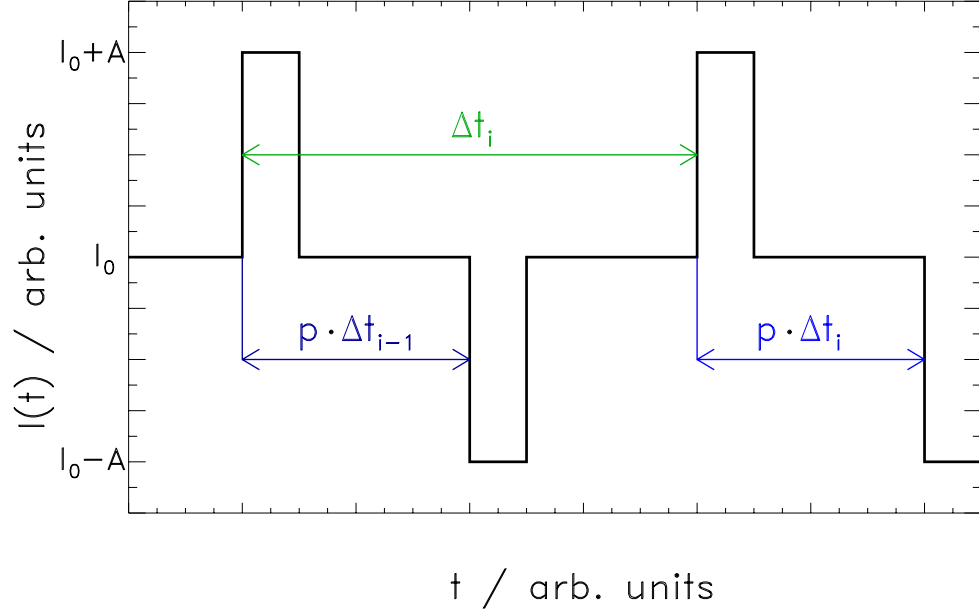


Figure 7.9: The time evolution of the control parameter $I(t)$ by applying double-pulse feedback described by the iterated map (7.44) and (7.45). Figure taken from (Schlesner, Zykov, Brandstädter, Gerdes & Engel 2008)

can be transformed into

$$\begin{aligned}
 x_{i+1} = & x_i - 2h \cos \left[\omega_0 \tau + \psi + \frac{2\pi}{\lambda_0} x_{i-k} + \frac{\pi p}{\lambda_0} (x_{i-k} - x_{i-k-1}) + \pi p \right] \\
 & \cdot \cos \left[\pi(0.5 - p) - \frac{\pi p}{\lambda_0} (x_{i-k} - x_{i-k-1}) \right]. \quad (7.47)
 \end{aligned}$$

The iterated map for the y -coordinate of the spiral core center is derived similarly and reads

$$\begin{aligned}
 y_{i+1} = & y_i - 2h \sin \left[\omega_0 \tau + \psi + \frac{2\pi}{\lambda_0} x_{i-k} + \frac{\pi p}{\lambda_0} (x_{i-k} - x_{i-k-1}) + \pi p \right] \\
 & \cdot \cos \left[\pi(0.5 - p) - \frac{\pi p}{\lambda_0} (x_{i-k} - x_{i-k-1}) \right]. \quad (7.48)
 \end{aligned}$$

As for single-pulse feedback the dynamics of the x coordinate do not depend on the dynamics of the y coordinate. Following Equation (7.47) the analytic expression

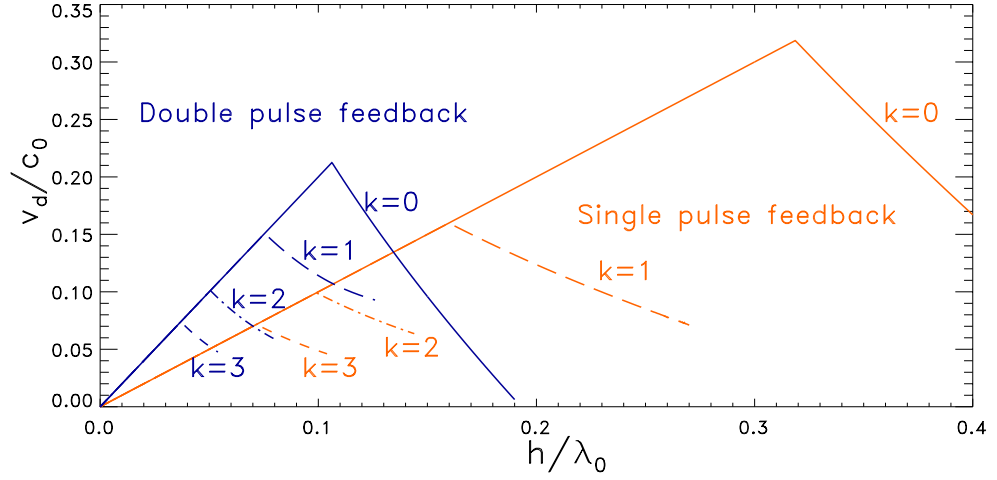


Figure 7.10: Average drift velocity of the spiral core center obtained by numerical simulations of the iterated map (7.47)-(7.48) by applying double-pulse feedback for different attractors (blue curves). The results obtained by application of single-pulse feedback are shown by red curves. Figure taken from (Schlesner, Zykov, Brandstädter, Gerdes & Engel 2008)

for the steady states x_s reads

$$\frac{x_s}{\lambda_0} = \frac{m}{2} - \frac{p}{2} - \frac{\tau}{T_0} - \frac{\psi}{2\pi}, \quad (7.49)$$

where m is a positive integer. This expression coincides with Equation (7.13) for $p = 0.5$. The steady states with even integer m correspond to resonant attractors, which are straight lines parallel to the detector. The steady states with odd integer m describe locations of the separatrices limiting the basins of attraction. During a stationary drift, each pulse shifts the spiral center along the attractor line by a distance Δy which can be determined from Equation (7.48) as

$$\Delta y = 2h \cos[\pi(0.5 - p)]. \quad (7.50)$$

Thus the maximum drift velocity is reached at $p = 0.5$.

A linear stability analysis of the steady states x_s with even integer m leads to the

following equation for the deviations $\delta x_i = x_i - x_s$

$$\delta x_{i+1} = \delta x_i - \frac{2\pi h}{\lambda_0} [(2+p)\delta x_{i-k} - p\delta x_{i-k-1}] \cos[\pi(0.5-p)]. \quad (7.51)$$

As mentioned above, the drift velocity achieves its maximum at $p = 0.5$. In this case the characteristic equation for the eigenvalues reads

$$\lambda^{k+2} - \lambda^{k-1} + \frac{5\pi h}{\lambda_0} \lambda - \frac{\pi h}{\lambda_0} = 0. \quad (7.52)$$

This equation has $k + 2$ roots, which can be found numerically for a given value h . For $k = 0$ the roots can be found analytically. This corresponds to the stability analysis of the attractor line closest to the detector. For small positive h , this attractor is stable but loses stability at

$$\frac{h_{cr}}{\lambda_0} = \frac{1}{3\pi}. \quad (7.53)$$

Comparison of this expression with Equation (7.41) shows that the drift instability appears earlier than for single–pulse feedback.

In Figure 7.10, the average drift velocity of the spiral core center in y –direction versus the absolute value of the displacement h is depicted. The blue curves correspond to double–pulse feedback and calculated from Equations (7.44) and (7.45). For comparison, the corresponding dependence for single–pulse feedback is shown by the red lines. It can be seen that for most of the attractors, the drift velocity induced by double pulses is larger than by single pulses. The only exception is in the case of $k = 0$. Here, under double–pulse feedback, the instability occurs at a control strength three time lower than under single–pulse feedback and the maximum drift velocity is smaller. Therefore, the described double–pulse algorithm increases the efficiency of the feedback control by application of small modulation pulses.

7.3 Numerical simulation of spiral core drift in reaction–diffusion systems

In this section our aim is to compare the results obtained from the iterated map with numerical simulations performed with reaction–diffusion models. Due to the

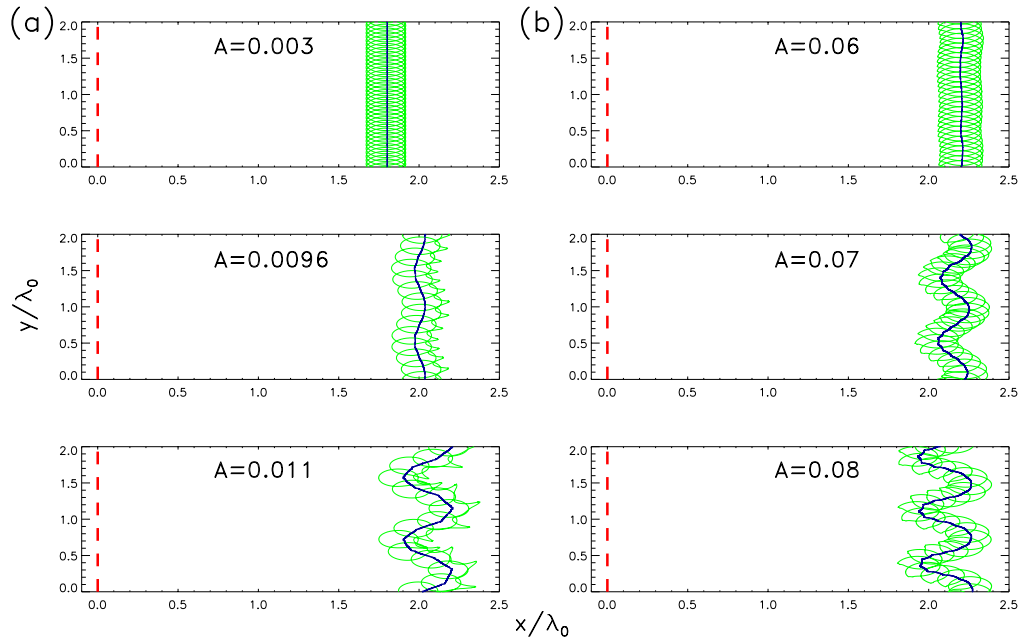


Figure 7.11: Spiral wave drift near a virtual straight line detector (dashed red line). Computations are performed (a) for the Oregonator model (2.1) and (2.2) with parameter set O3, and (b) for the FitzHugh-Nagumo model (2.5) and (2.6) with parameter set F2. Thin green curves show the spiral tip trajectories. Blue curves indicate pathways of the spiral core center. Figures taken from (Schlesner, Zykov, Brandstädter, Gerdes & Engel 2008)

fact that the experiments were performed with the light-sensitive BZ reaction, we used the Oregonator model (2.1) and (2.2) again but verified our results with the FHN model (2.5) and (2.6).

7.3.1 Spiral core drift in the Oregonator model

For the numerical simulations performed with the Oregonator model we use parameter set O3 and the control signal $I(t)$ introduced in the previous section as applied to ϕ : $\phi(t) = I(t)$. The autonomous system with $I_0 = 0.01$ has a steady state that is stable with respect to small perturbations. However, a supra-threshold perturbation, once locally applied, gives rise to a concentric wave propagating through the medium. A spiral wave rotating counterclockwise near the center of the simulated domain was created by a special choice of initial conditions. The spiral tip per-

formed a compound rotation (meandering motion) including at least two different frequencies. The oscillation period measured far enough from the symmetry center of the unperturbed tip trajectory was $T_\infty = 7.65$.

In accordance with the first feedback algorithm a short pulse increasing the value $I(t)$ of the amplitude A is generated each time the rotating spiral wave front is tangent to a straight line used as a detector. The duration of this pulse was fixed at 0.7 and is small in comparison to the rotation period. Each single pulse induces a displacement of the spiral core center with a magnitude h . Due to a permanent rotation of a spiral wave it is influenced by a sequence of the controlling pulses. Single shifts accumulate, resulting in a drift of the spiral wave core.

First of all, we performed computations with a relatively small amplitude of the applied pulses ($A = 0.002$) in order to check the applicability of the iterated map (7.2)-(7.7) to the Oregonator model. Several trajectories corresponding to different initial locations of the spiral center are shown in Figure 7.4. It can be seen that the iterated map computed with $\psi = 2.39$ quantitatively predicts the asymptotic values of the attractor distances from the detector line. Moreover, the transient parts of the drift pathways are in good agreement with the map predictions.

Figure 7.11(a) shows the spiral tip trajectory obtained numerically under this feedback control for the attractor characterized by $k = 1$. The stationary drift depicted in this figure is established after a short transience, which is not shown here. Thin green curves indicate the trajectories of the spiral wave tip. The time average of these trajectories corresponds to the paths of the core center and is shown by thick black curves. Until the amplitude A of the applied pulses is rather small ($A = 0.003$), the drift of the core center occurs along a straight line. For larger amplitude ($A = 0.0096$) the pathway of the core center oscillates near a straight line with relatively small amplitude a (c.f. Figure 7.6). These oscillations appear due to the instability predicted by the iterated map. Indeed, the magnitude h of the single shift of the core center is a monotonously growing function of the amplitude A . Therefore the instability should appear when $A > A_{cr}$. The instability becomes more pronounced with growing amplitude of the pulses. The pathway of the core center obtained for $A = 0.011$ deviates very strongly from a straight line, which decreases the average drift velocity in y direction. In Figure 7.3.1 the relation between the increase of the deviation a and the decrease of the average drift velocity in y direction

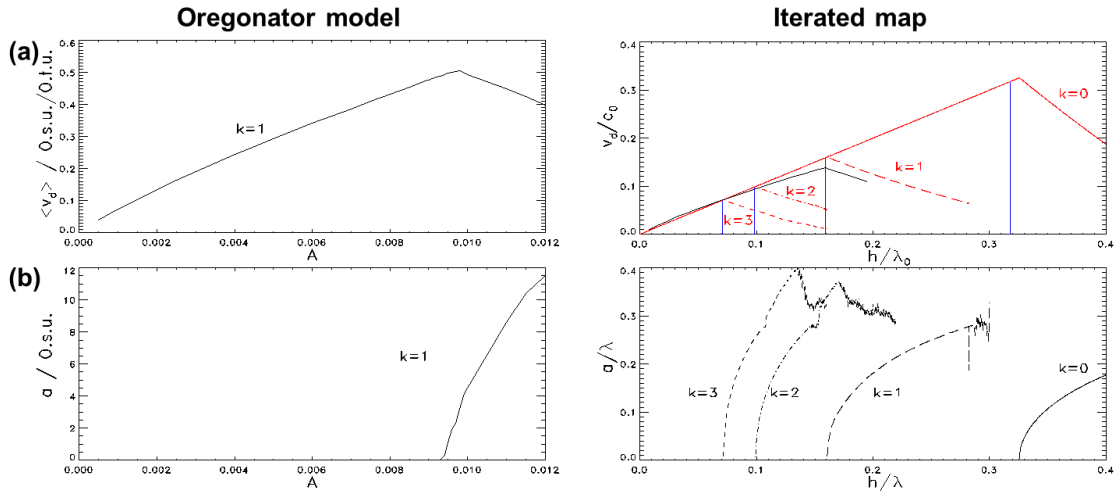


Figure 7.12: (a) Average drift velocity $\langle v_d \rangle$ in the y -direction obtained from the Oregonator model (2.1) and (2.2) with parameter set O3 for the attractor with $k = 1$ in dependence on the control amplitude A in comparison with the results from the iterated map. Right figure taken from (Schlesner, Zykov, Brandstatter, Gerdes & Engel 2008). (b) Related curve of the deviation amplitude a from the steady state. Before the bifurcation point A_{cr} the deviation vanishes and the average drift velocity growth proportional to the control amplitude A . At the bifurcation point the pathway of the core center starts to oscillate around the attractor and the deviation amplitude a growth in square-root-shape. Due to this the average drift velocity decreases with increasing control amplitude A .

$\langle v_d \rangle$ is depicted. Before the bifurcation point, the deviation amplitude a vanishes and the average drift velocity growth is proportional to the control amplitude A . However at the bifurcation point, the average drift velocity $\langle v_d \rangle$ starts to decrease and the deviation amplitude a simultaneously starts to grow with increasing control amplitude A in square root form. This is in very good qualitative agreement with the results obtained from the iterated map (please refer to Figure 7.8).

The average drift velocity induced by the applied feedback control is also shown in Figure 7.3.1 as a function of the magnitude h of a displacement induced by a single pulse. It is shown that this numerical data is in good quantitative agreement with the results obtained from the iterated map (7.2)-(7.7).

Now we have to distinguish between the single-pulse and the double-pulse feedback methods. From the results obtained from the iterated map, we expect that

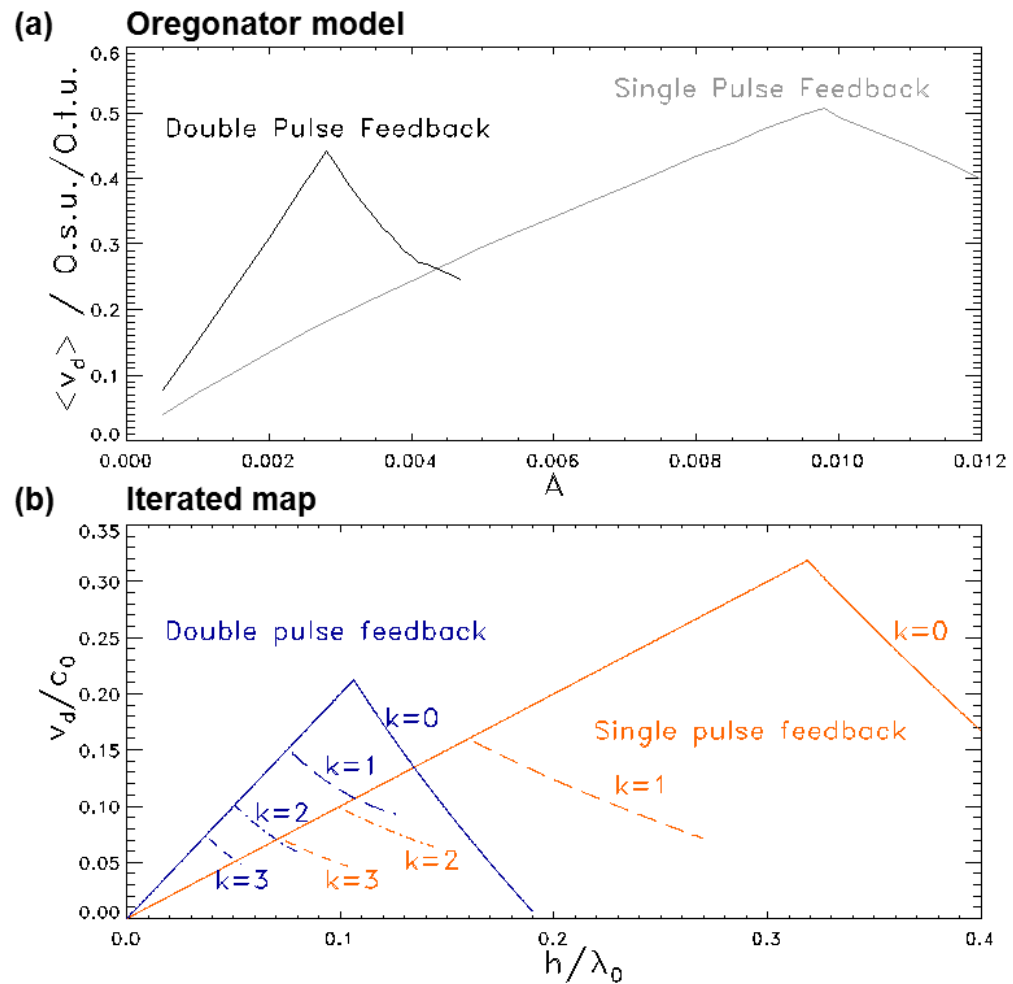


Figure 7.13: (a) Average drift velocity of the spiral core center observed in the Oregonator model (2.1) and (2.2) with parameter set O3. The grey line is obtained by applying the single-pulse and the black line by applying the double-pulse feedback method. (b) As a comparison, average drift velocity of the spiral core center obtained by numerical simulations of the iterated map. Figure taken from (Schlesner, Zykov, Brandstatter, Gerdes & Engel 2008).

by applying double–pulse instead of single–pulse feedback, the spiral core center moves faster parallel to the detector line, but also that the bifurcation point occurs earlier (please refer to Figure 7.10). In Figure 7.3.1, the average drift velocity of the spiral core center is depicted for single–pulse (grey line) and for double–pulse feedback (black line). By comparing these results with the results for the iterated map, which are shown in Figure 7.10, it is obvious that the results are very similar.

7.3.2 Spiral core drift in the FHN model

For the FHN model, the simulations are performed with parameter set F2 and $F(t) = I(t)$. In full agreement with the theoretical considerations above, the drift occurs along a straight line parallel to the detector if the amplitude A is smaller than some critical value. Such a drift is computed for $A = 0.06$ as shown in Figure 7.11 (b). The appearance of instability is illustrated by computations performed with $A = 0.07$. Here the pathway of the core center deviates considerably from a straight line. The amplitude of these deviations becomes larger when the pulse amplitude is increased to $A = 0.08$.

These computations demonstrate once again that the spiral wave location can be effectively controlled by the proposed feedback algorithm regardless of the kind of excitable medium model used for simulations.

It is important to mention here that the theory for the detector–line–feedback was only elaborated for rigidly rotating spiral waves. Now we will investigate if this feedback method can be successfully applied to meandering or hypermeandering spiral waves as well. In Figure 7.14 the trajectories of spiral wave tips for (a) a rigidly rotating, (b) a meandering and (c) a hypermeandering spiral wave under this feedback method are depicted. For the meandering spiral wave, the effect of the feedback method is comparable to the effect on rigidly rotating spiral waves except that the trajectory is not as regular as that for rigidly rotating spiral waves. The excellent conformity of the results obtained for rigidly rotating with meandering spiral waves is confirmed by all of the numerical simulations we performed with meandering spiral waves. As shown in Figure 7.14(c) the movement of the spiral wave tip for hypermeandering spiral waves is very unsteady. The movement alternates irregularly between a movement parallel to the detector line and persisting at the current location. So in this case, the average drift velocity in y –direction

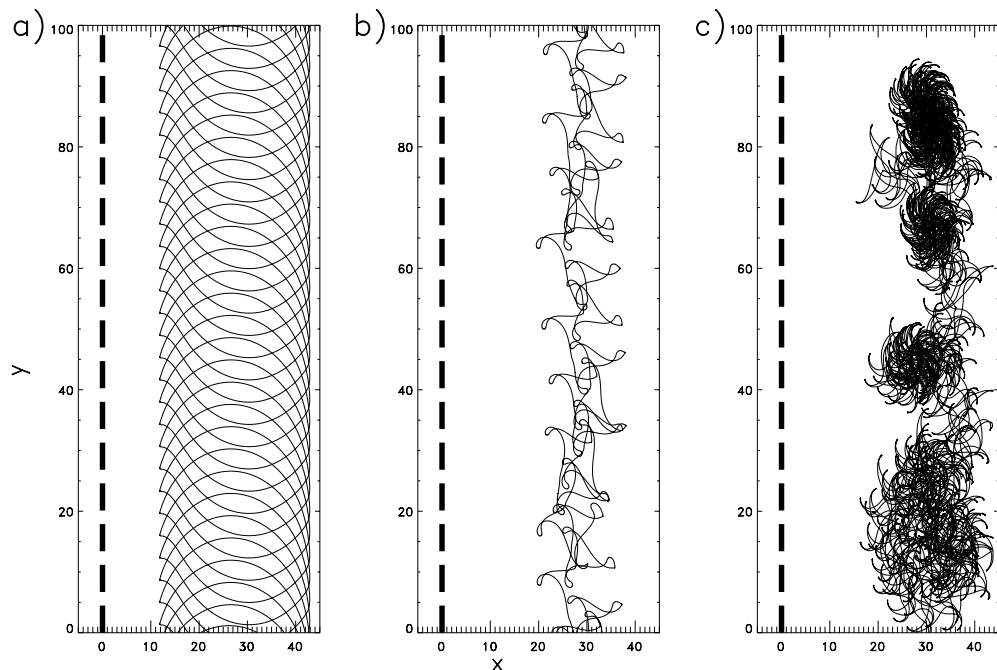


Figure 7.14: Trajectories of the spiral wave tip under double-pulse feedback obtained in the FHN model with parameter set F2 for a) a rigidly rotating, b) meandering and c) hypermeandering spiral wave. The thick dashed lines are the detector lines. Figure right taken from (Schlesner, Zykov & Engel 2008).

is significantly reduced by applying this method to hypermeandering spiral waves, but a movement in the expected direction is also induced.

7.4 Experimental observation of feedback induced drift

In this section we verify the results obtained from the iterated maps and the numerical simulation with experiments with the light-sensitive BZ reaction introduced in Chapter 4.

The dashed red line in Figure 7.15 represents the virtual detector used in the feedback algorithm under investigation. The duration of the light pulse is 2 s. Here, the application of this pulse changes the excitability of the medium, modifies the unperturbed trajectory of the spiral tip and induces a shift of the spiral core.

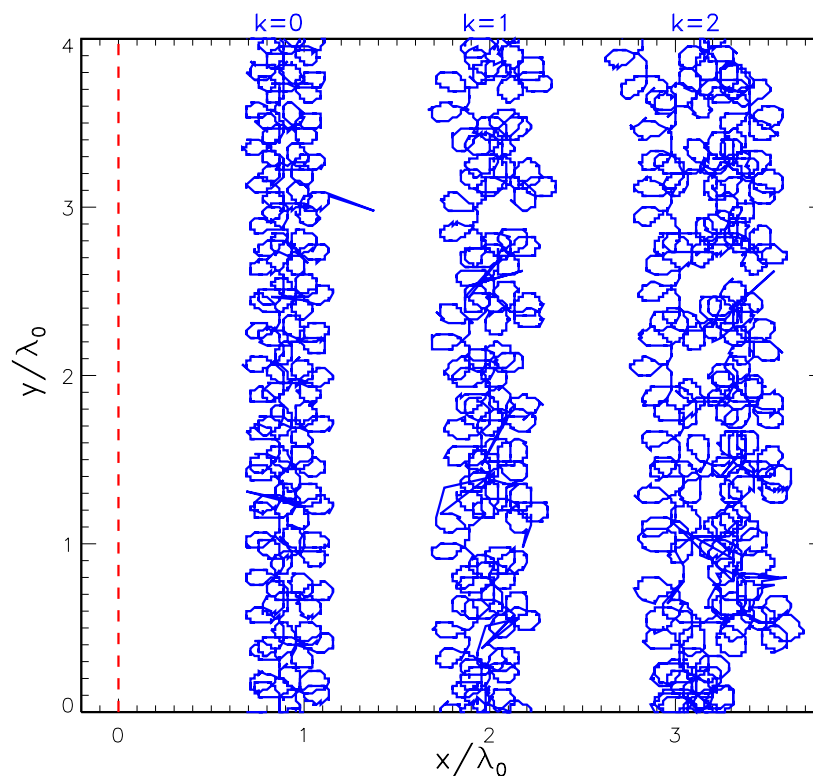


Figure 7.15: Spiral wave drift near a virtual straight line detector (dashed red line) observed in experiments with the light-sensitive BZ reaction by applying single-pulse feedback. Blue lines show trajectories of the spiral wave tip corresponding to three different initial locations of the spiral wave core. Figure taken from (Schlesner, Zykov, Brandstädter, Gerdes & Engel 2008).

Figure 7.15 shows three trajectories of the spiral tip observed in the case of a line detector. After a short transience (not shown here) the spiral core drifts parallel to the detector line up to the boundary of the reactor as expected from the results obtained from the iterated map and numerical simulations. Although the spiral wave tip describes a rather complicated meandering trajectory consisting of many loops, the average drift of the core center occurs along a straight line parallel to the detector. Small variations in the initial location of the spiral core would result in a slightly different transient process, but the drift of the core center effectively occurs along the same path. Not only the attractor for $k = 0$ but also the attractors for $k = 1$ and $k = 2$ are shown in Figure 7.15. The distance between neighboring paths

is roughly the wave length of the spiral. Thus, the induced drift allows us to push the spiral wave to the boundary of the medium along the shortest pathway. All these findings are in very good agreement with the predicted characteristics.

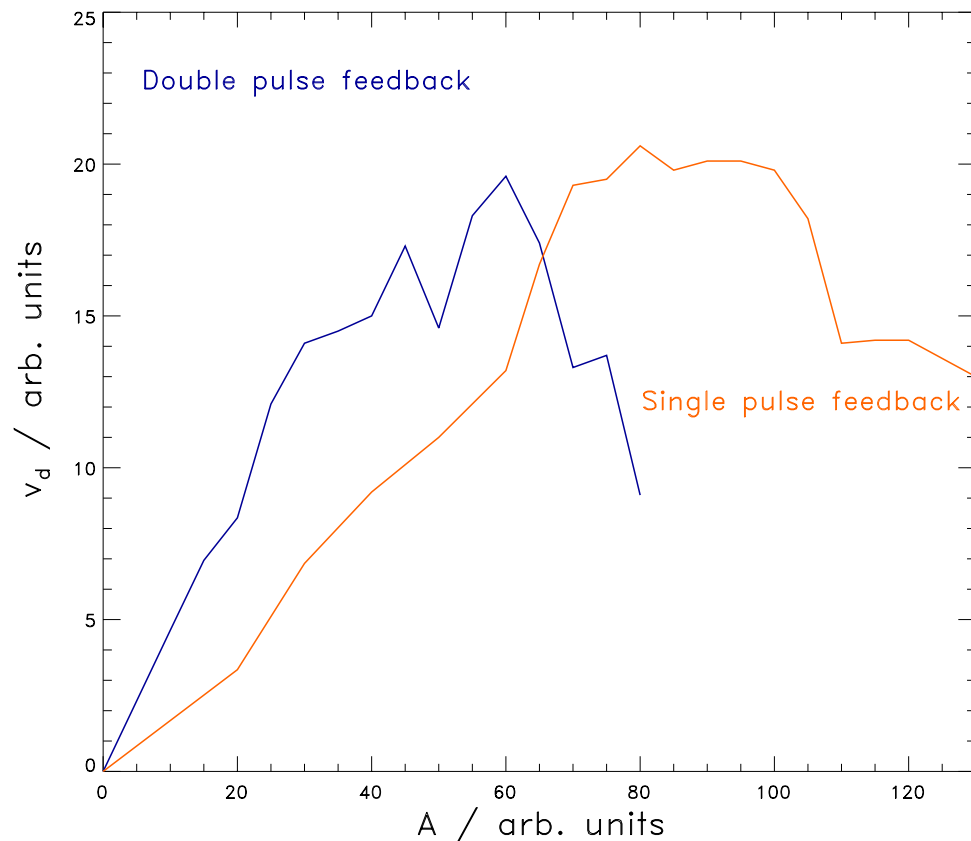


Figure 7.16: Average drift velocity of the spiral core center observed in experiments with the light-sensitive BZ reaction by applying double-pulse feedback (blue curve) and single-pulse feedback (orange curve). Figure taken from (Schlesner, Zykov, Brandstadter, Gerdes & Engel 2008).

In addition to the qualitative results shown in Figure 7.15, we measured the average drift velocity of the spiral core center as a function of the amplitude A of the applied light pulses. The results are shown in Figure 7.16. The two curves represent the average results over several experimental series. This averaged data allows us to conclude that the drift velocity can be increased by increasing the pulse amplitude. There is an instability which appears when the amplitude exceeds some critical value. This instability restricts the drift velocity. The double-pulse feedback

7.4. EXPERIMENTAL OBSERVATION OF FEEDBACK INDUCED DRIFT

algorithm allows us to increase the efficiency of the feedback control. Although the experiments were performed with hypermeandering spiral waves, all of these conclusions are in agreement with the theoretical predictions made above and with the numerical analysis of the reaction–diffusion models.

8 Summary

For our investigations regarding the dynamics and control of spiral waves we used different control schemes - external forcing and feedback-mediated control. The control methods, along with our results, are recapped in the next section. Since we developed an experimental setup with significant advantages in comparison to other setups, we sum up its main benefits in its own section at the end of this chapter.

8.1 Control of spiral wave dynamics

As our objective is to study spiral wave dynamics in general and not for a distinct system, we have proven whether or not the results obtained for a distinct system can be generalized. So, as an example, we verified our numerical results from the Oregonator model with results obtained from simulations with the FitzHugh-Nagumo model. In addition we checked the results theoretically, numerically and experimentally. Furthermore, especially for our theoretical investigations we often used models based only on the general characteristics of spiral waves (like the Archimedean shape of spiral waves) without the effect or influence of a distinct system.

8.1.1 External forcing by traveling wave modulation

Studies of the dynamics of rigidly rotating spiral waves under traveling wave modulation have shown a drift of the core center dependent on the ratio of T_m/T_0 (Zykov et al. 2006), where T_m is the period of the light modulation and T_0 the period of the rigidly rotating spiral wave. In contrast to normal synchronization, traveling wave modulation shows that frequency locking is not necessary for synchronized drift. This is caused by the motion of the spiral core, which induces a Doppler-shift of the modulation frequency. In addition to that, the synchronized drift does not only occur at a fixed value of modulation period T_m , but rather in a synchronization

range of the ratio T_m/T_0 around 1.0. As such, the drift direction strongly depends on this ratio.

Our experimental and numerical investigations of the dynamics of meandering spiral waves (in contrast to the rigidly rotating spiral waves mentioned above) are in very good qualitative agreement with each other and with the numerical and theoretical results for rigidly rotating spiral waves. When regarding meandering spiral waves, the period of rigid rotation T_0 has to be replaced by the period of rotation far from the core T_∞ . At some values of the ratio T_m/T_∞ there are deviations in the experimental results in comparison to the numerical results, which can be caused by synchronization effects with other intrinsic periods of the meandering spiral wave. However, our numerical simulations and experiments prove that the traveling wave modulation can be used as an effective tool to control the location even of meandering spiral waves in excitable media.

8.1.2 Feedback-mediated control

Control of spiral wave location by detector line feedback

Detector line feedback is a control method in which a short perturbation (such as a light pulse in our experiments) is generated each time a spiral wave front is tangent to a given curve or touches its open end. In general, given an unpinned spiral wave at a certain position in the medium, the proposed feedback scheme allows movement of the spiral wave core in a well-controlled manner along a chosen trajectory to any desired position, avoiding those areas where the spiral wave could be captured by defects or heterogeneities.

A theory of the presented feedback-induced dynamics of spiral waves has been elaborated. In a certain approximation, the partial differential equations can be reduced to ordinary differential equations for the velocity field of the feedback-induced drift. The obtained velocity fields predict the movement of the spiral core as observed experimentally and in numerical simulations.

We have observed good agreement between the theoretically calculated velocity field of resonant drift and the trajectories of the spiral center obtained numerically or observed experimentally. By linear stability analysis, the developed theory allows us to determine the critical feedback strength, above which the drift regime

becomes unstable. To increase the spiral core drift velocity of the feedback control, we proposed generating one additional negative pulse, delayed with respect to the positive one (e.g. in the middle of two positive pulses). Our theoretical, numerical and experimental results show that by applying the double-pulse feedback method, the spiral core cannot be moved faster, but rather more efficiently, i.e. with lower control forces.

The close agreement between the theoretical predictions and numerical or experimental data proves that the results obtained possess general characteristics and can be applied to the dynamics of spiral waves in quite different excitable media. Spatially uniform cardiac tissue is clearly highly idealized, as the spreading of waves in cardiac tissue is strongly influenced by the structure of the medium (such as its profile and its heterogeneity), the movement of the medium and 3d-effects. Although the proposed control algorithm can not be implemented in current implantable cardioverter defibrillator technology, we hope that our study will be useful for future anti-arrhythmic pacing devices.

Feedback-mediated stabilization of unstable rigid rotation

We have presented an example of the stabilization of a two-dimensional spatio-temporal pattern by global, non-invasive feedback control. Meandering and hypermeandering spiral waves are forced into the regime of rigid rotation, which still exists but is unstable in the absence of feedback. This enables the determination of the core radius and rotation frequency of unstable rigid rotation without explicit use of the model equations. This opens up new perspectives for corresponding experimental studies. It is important to note that from the stabilized two-dimensional spatio-temporal pattern, aside from the core radius and the rotation frequency, other characteristics can be obtained, for example, the spatial profile of the unstable wave or the spatial gradient close to the spiral core. We demonstrate that these methods could be used to track unstable solutions by simultaneously varying the bifurcation parameter. This information could be very helpful in testing the validity of various theoretical approaches to spiral wave dynamics (Kothe, Zykov & Engel 2009, Hakim & Karma 1999, Kessler et al. 1994, Margerit & Barkley 2002).

Two different non-invasive control methods, proportional feedback control (PFC) and time delay autosynchronization (TDAS), have been considered. While both

methods allow for the stabilization of the wave pattern in a broad range of parameters, a more detailed comparison reveals specific advantages and disadvantages of each method as discussed in the previous section. PFC requires the determination of some reference radius r_0 which is not as difficult as finding the appropriate delay time τ necessary for TDAS. Moreover, PFC works in a comparably larger range of the feedback strength K , and stabilizes the core center at the reference point. In comparison, TDAS is less sensitive to latency effects, as the control domain extends to larger latency times and leads to successful stabilization at smaller control forces.

The commonly accepted opinion is that the method of tip definition has no pronounced effect on results concerning spiral wave dynamics, for example, the bifurcation diagram of the rotation regimes (Jahnke & Winfree 1991). In the context of feedback-mediated stabilization, the situation turns out to be quite different. Sometimes stabilization fails when the tip definition is based on the slow inhibitor instead of the fast activator field. We showed that one possible reason for this is the influence of a control loop latency in the feedback loop. To overcome this difficulty we proposed an approximate method to reconstruct the activator field from the inhibitor field. This method works well for the Oregonator model of the light-sensitive BZ reaction where only the slow field is experimentally accessible.

8.2 Experimental setup

Since most experimental setups, that allow for the application of spatio-temporal control forces in light-sensitive Belousov-Zhabotinsky systems have major disadvantages, like inhomogeneous illumination, we have developed an experimental setup to perform our studies with spatio-temporally applied light intensity.

Our aim was not to improve an existing experimental setup, but rather to develop a setup using only components that are most suitable for the regarded application. In comparison with other setups, the main advantages of our experimental setup are

- **the non-stroboscopic separation of the control (actinic) and monitoring light:** To avoid the effects of the stroboscopic separation on the experimental results (like synchronization effects), we use polarization to separate both light channels. The negative effect of the polarizer application on

the maximal light intensity is small, as the control light is already polarized due to the use of a spatial light modulator (SLM).

- **the use of long lasting LEDs and appropriated optical systems:** Due to the fact that we choose an SLM as a visualization device instead of an integrated projection system (e.g. a video projector), we are also able to choose the light source and optical system. The blue LEDs used only emit light in the absorption band of the catalyst and the LEDs have a long lifetime with constant brightness. In addition, the small emitting area of the LED and the adapted optical system provide sharp and undistorted optical imaging.
- **the modular structure of the control software in LabView:** The software is built up modularly on two levels - the program code in LabView and the client-server-architecture (control program, camera server and display server). On the one hand, the modular structure of the program code facilitates the easy extension of the software so that new control or observation techniques can be implemented quickly. On the other hand, the modular client-server-architecture enables the easy integration of additional displays or cameras into the experimental setup.

Bibliography

- Agladze, K. I., Davydov, V. A. & Mikhailov, A. (1987), ‘Observation of a spiral wave resonance in an excitable distributed medium’, *JETP Lett.* **45**(12), 767–770.
- Allessie, M. A., Bonke, F. I. M. & Schopman, F. J. G. (1973), ‘Circus movement in rabbit atrial muscle as a mechanism of tachycardia’, *Circ. Res.* **33**, 54–62.
- Aranson, I. S., Aranson, L., Kramer, L. & Weber, A. (1992), ‘Stability limits of spirals and traveling waves in nonequilibrium media’, *Phys. Rev. A* **46**(6), R2992–R2995.
- Bánsági, T. & Steinbock, O. (2006), ‘Nucleation and collapse of scroll rings in excitable media’, *Phys. Rev. Lett.* **97**, 198301.
URL: <http://link.aps.org/doi/10.1103/PhysRevLett.97.198301>
- Barkley, D. (1992), ‘Linear stability analysis of rotating spiral waves in excitable media’, *Phys. Rev. Lett.* **68**(13), 2090–2093.
- Barkley, D. (1994), ‘Euclidean symmetry and the dynamics of rotating spiral waves’, *Phys. Rev. Lett.* **72**(1), 164–167.
- Barkley, D., Kness, M. & Tuckerman, L. S. (1990), ‘Spiral-wave dynamics in a simple model of excitable media: The transition from simple to compound rotation’, *Phys. Rev. A* **42**(4), 2489–2492.
- Beck, O., Amann, A., Schöll, E., Socolar, J. E. S. & Just, W. (2002), ‘Comparison of time-delayed feedback schemes for spatio-temporal control of chaos in a reaction-diffusion system with global coupling’, *Phys. Rev. E* **66**(1), 016213.
- Biktashev, V. N. & Holden, A. V. (1994), ‘Design principles of a low voltage cardiac defibrillator based on the effect of feedback resonant drift’, *J. Theor. Biol.* **169**(2), 101–112.

- Bleich, M. E. & Socolar, J. E. S. (1996), ‘Controlling spatiotemporal dynamics with time-delay feedback’, *Phys. Rev. E* **54**(1), R17–R20.
- Brandtstädter, H., Braune, M., Schebesch, I. & Engel, H. (2000), ‘Experimental study of the dynamics of spiral pairs in light-sensitive belousov-zhabotinskii media using an open-gel reactor’, *Chem. Phys. Lett.* **323**, 145–154.
- Braune, M. & Engel, H. (1993), ‘Compound rotation of spiral waves in active media with periodically modulated excitability’, *Chem. Phys. Lett.* **211**(6), 534–540.
- Braune, M. & Engel, H. (2000), ‘Feedback-controlled forcing of meandering spiral waves in an open gel reactor’, *Phys. Rev. E* **62**(5), 5986–5988.
- Christini, D. J. & Glass, L. (2002), ‘Introduction: Mapping and control of complex cardiac arrhythmias’, *Chaos* **12**(3), 732.
- Davidenko, J. M., Pertsov, A. M., Salomonsz, R., Baxter, W. & Jalife, J. (1992), ‘Stationary and drifting spiral waves of excitation in isolated cardiac muscle’, *Nature* **355**, 349–351.
- Davydov, V. A., Zykov, V. S. & Mikhailov, A. S. (1991), ‘Kinematics of autowave patterns in excitable media’, *Sov. Phys. Usp.* **161**, 665–684.
- Fast, V. G. & Pertsov, A. M. (1992), ‘Shift and termination of functional reentry in isolated ventricular preparations with quinine-induced inhomogeneity in refractory period’, *J. Cardiovasc. Electrophysiol* **3**, 255–265.
- Fiedler, B., Sandstede, B., Scheel, A. & Wulff, C. (1996), ‘Bifurcation from relative equilibria of noncompact group actions: Skew products, meanders, and drifts’, *Doc.Math.J.DMV* **1**, 479–505.
- Field, R. J. & Burger, M. (1985), *Oscillations and traveling waves in chemical systems*, Wiley New York.
- FitzHugh, R. (1961), ‘Impulses and physiological states in theoretical models of nerve membrane’, *Biophys. J.* **1**, 445–466.
- Franceschini, G., Bose, S. & Schöll, E. (1999), ‘Control of chaotic spatiotemporal spiking by time-delay autosynchronisation’, *Phys. Rev. E* **60**(5), 5426–5434.

- Gerisch, G. (1971), ‘Periodische signale steuern die musterbildung in zellverbänden’, *Naturwissenschaften* **58**(9), 430–438.
- Golubitsky, M., LeBlanc, V. G. & Melbourne, I. (1997), ‘Meandering of the spiral tip: An alternative approach’, *J. Nonlinear Sci.* **7**(6), 557.
- Gorelova, N. A. & Bures, J. (1983), ‘Spiral waves of spreading depression in the isolated chicken retina.’, *J. Neurobiol.* **14**, 353–363.
- Grill, S., Zykov, V. S. & Müller, S. C. (1995), ‘Feedback-controlled dynamics of meandering spiral waves’, *Phys. Rev. Lett.* **75**(18), 3368–3371.
- Hakim, V. & Karma, A. (1999), ‘Theory of spiral wave dynamics in weakly excitable media: Asymptotic reduction to a kinematic model and applications’, *Phys. Rev. E* **60**(5), 5073–5105.
- Hermerschmidt, A., Quiram, S., Kallmeyer, F. & Eichler, H. J. (2007), ‘Determination of the jones matrix of an lc cell and derivation of the physical parameters of the lc molecules’, *Proc. SPIE* p. 6587.
- Hövel, P. & Socolar, J. E. S. (2003), ‘Stability domains for time-delay feedback control with latency’, *Phys. Rev. E* **68**(3), 036206.
- Jahnke, W., Skaggs, W. E. & Winfree, A. T. (1989), ‘Chemical vortex dynamics in the belousov–zhabotinskii reaction and in the two-variable oregonator model’, *J. Phys. Chem.* **93**(2), 740–749.
- Jahnke, W. & Winfree, A. T. (1991), ‘Spiral wave behaviors’, *Int. J. Bifur. Chaos* **1**(2), 455.
- Jakubith, S., Rotermund, H. H., Engel, W., von Oertzen, A. & Ertl, G. (1990), ‘Spatiotemporal concentration patterns in a surface reaction: Propagating and standing waves, rotating spirals, and turbulence’, *Phys. Rev. Lett.* **65**(24), 3013–3016.
- Jiménez, Z. A. & Steinbock, O. (2012), ‘Scroll wave filaments self-wrap around unexcitable heterogeneities’, *Phys. Rev. E* **86**, 036205.
URL: <http://link.aps.org/doi/10.1103/PhysRevE.86.036205>

- Just, W., Bernard, T., Ostheimer, M., Reibold, E. & Benner, H. (1997), ‘Mechanism of time-delayed feedback control’, *Phys. Rev. Lett.* **78**(2), 203–206.
- Just, W., Reckwerth, D., Möckel, J., Reibold, E. & Benner, H. (1998), ‘Delayed feedback control of periodic orbits in autonomous systems’, *Phys. Rev. Lett.* **81**(3), 562–565.
- Just, W., Reckwerth, D., Reibold, E. & Benner, H. (1999), ‘Influence of control loop latency on time-delayed feedback control’, *Phys. Rev. E* **59**(3), 2826–2829.
- Kádár, S., Wang, J. & Showalter, K. (1998), ‘Noise-supported travelling waves in sub-excitable media’, *Nature* **391**, 770.
- Kapral, R. & Showalter, K. (1995), *Chemical Waves and Patterns*, Kluwer Academic Publishers, Dordrecht.
- Karma, A. & Zykov, V. S. (1999), ‘Structure of the resonance attractor for spiral waves in excitable media’, *Phys. Rev. Lett.* **83**(12), 2453–2456.
- Keener, J. P. & Tyson, J. J. (1986), ‘Spiral waves in the belousov-zhabotinskii reaction’, *Physica D* **21**(2–3), 307–324.
- Kessler, D. A., Levine, H. & Reynolds, W. N. (1994), ‘Theory of the spiral core in excitable media’, *Physica D* **70**(1-2), 115–139.
- Kittel, A., Parisi, J. & Pyragas, K. (1995), ‘Delayed feedback control of chaos by self-adapted delay time’, *Phys. Lett. A* **198**(5–6), 433–436.
- Kothe, A., Zykov, V. S. & Engel, H. (2009), ‘Second universal limit of wave segment propagation in excitable media’, *Phys. Rev. Lett.* **103**, 154102.
- Krug, H.-J., Pohlmann, L. & Kuhnert, L. (1990), ‘Analysis of the modified complete Oregonator accounting for oxygen sensitivity and photosensitivity of Belousov–Zhabotinsky systems’, *J. Phys. Chem.* **94**, 4862–4866.
- Lechleiter, J., Girard, S., Peralta, E. & Clapham, D. (1991), ‘Spiral calcium wave propagation and annihilation in xenopus laevis oocytes’, *Science* **252**(5002), 123–126.

- Li, G., Ouyang, Q., Petrov, V. & Swinney, H. L. (1996), ‘Transition from simple rotating chemical spirals to meandering and traveling spirals’, *Phys. Rev. Lett.* **77**, 2105–2108.
- Löber, J. & Engel, H. (2013), ‘Analytical approximations for spiral waves’, *Chaos* **23**, 043135.
- Lüthje, O., Wolff, S. & Pfister, G. (2001), ‘Control of chaotic taylor-couette flow with time-delayed feedback’, *Phys. Rev. Lett.* **86**(9), 1745–17748.
- Mantel, R.-M. & Barkley, D. (1996), ‘Periodic forcing of spiral waves in excitable media’, *Phys. Rev. E* **54**(5), 4791–4802.
- Margerit, D. & Barkley, D. (2002), ‘Cookbook asymptotics for spiral and scroll waves in excitable media’, *Chaos* **12**(3), 636–.
- Markus, M., Nagy-Ungvarai, Z. & Hess, B. (1992), ‘Phototaxis of spiral waves’, *Science* **257**(5067), 225–227.
- Martins-Ferreira, H., Castro, G. D. O., Struchiner, C. J. & Rodrigues, P. S. (1974), ‘Circling spreading deprssion in isolated chick retina’, *J. Neurophysiol.* **37**(2), 773–784.
- Maselko, J. & Showalter, K. (1989), ‘Chemical waves on spherical surfaces’, *Nature* **339**, 609–611.
- McWilliam, J. A. (1887), ‘Fibrillar contraction of the heart’, *J. Physiol.* **8**, 296–310.
- Mihaliuk, E., Sakurai, T., Chirila, F. & Showalter, K. (2002*a*), ‘Experimental and theoretical studies of feedback stabilization of propagating wave segments’, *Faraday Disc.* **120**, 383–394.
- Mihaliuk, E., Sakurai, T., Chirila, F. & Showalter, K. (2002*b*), ‘Feedback stabilization of unstable propagating waves’, *Phys. Rev. E* **65**(6), 065602.
- Mikhailov, A. S., Davydov, V. A. & Zykov, V. S. (1994), ‘Complex dynamics of spiral waves and motion of curves’, *Physica D* **70**(1), 1–39.
- Mikhailov, A. S. & Showalter, K. (2006), ‘Control of waves, patterns and turbulence in chemical systems’, *Phys. Rep.* **425**, 79–194.

- Müller, S. C., Plessner, T. & Hess, B. (1987), ‘Two-dimensional spectrophotometry of spiral wave propagation in the belousov-zhabotinskii reaction i. experiments and digital data representation’, *Physica D* **24**, 71–86.
- Nagumo, J., Arimoto, S. & Yoshizawa., S. (1962), ‘An active pulse transmission line simulating nerve axon.’, *Proc. IRE* **50**, 2061.
- Nakouzi, E., Jiménez, Z. A., Biktashev, V. N. & Steinbock, O. (2014), ‘Analysis of anchor-size effects on pinned scroll waves and measurement of filament rigidity’, *Phys. Rev. E* **89**, 042902.
- Ning-Jie, W., Jun, M., Jing-an, C. & He-Ping, Y. (2008), ‘Dynamics of vortex-wave under a travelling-wave modulation’, *Chin. Phys. Lett.* **25**(12), 4207–4210.
- Panfilov, A. V., Müller, S. C., Zykov, V. S. & Keener, J. P. (2000), ‘Elimination of spiral waves in cardiac tissue by multiple electrical shocks’, *Phys. Rev. E* **61**(4), 4644–4647.
- Paulau, P. V., Löber, J. & Engel, H. (2013), ‘Stabilization of a scroll ring by a cylindrical neumann boundary’, *Phys. Rev. E* **88**, 062917.
- Plessner, T. & Müller, K.-H. (1995), ‘Fourier analysis of the complex motion of spiral tips in excitable media’, *Int. J. Bifurc. and Chaos* **5**(4), 1071–1084.
- Pyragas, K. (1992), ‘Continuous control of chaos by self-controlling feedback’, *Phys. Lett. A* **170**(6), 421–428.
- Reményi, J., Várhegyi, P., Domján, L., Koppa, P. & oke Lőrincz, E. (2003), ‘Amplitude, phase, and hybrid ternary modulation modes of a twisted-nematic liquid-crystal display at 400 nm’, *Appl. Opt.* **42**(17), 3428–3434.
- Rüdiger, S., Miguez, D., Munuzuri, A., Sagues, F. & Casademunt, J. (2003), ‘Dynamics of turing patterns under spatiotemporal forcing’, *Phys. Rev. Lett.* **90**(12), 128301.
- Rüdiger, S., Nicola, E. M., Casademunt, J. & Kramer, L. (2007), ‘Theory of pattern forming systems under traveling-wave forcing’, *Phys. Rep.* **447**, 73–111.

- Sandstede, B., Scheel, A. & Wulff, C. (1997), ‘Dynamics of spiral waves on unbounded domains using center-manifold reductions’, *J. Differ. Equ.* **141**(1), 122–149.
- Sandstede, B., Scheel, A. & Wulff, C. (1999), ‘Bifurcations and dynamics of spiral waves’, *J. Nonlinear Sci.* **9**(4), 439–478.
- Schebesch, I. (1999), Wellenausbreitung unter Variation der Anregungsschwelle des Mediums, PhD thesis, TU Berlin.
- Schlesner, J., Zykov, V. & Engel, H. (2008), *Handbook of Chaos Control: Feedback-mediated control of hypermeandering spiral waves*, Wiley New York.
- Schlesner, J., Zykov, V., Engel, H. & Schöll, E. (2006), ‘Stabilization of unstable rigid rotation of spiral waves in excitable media’, *Phys. Rev. E* **74**, 046215.
- Schlesner, J., Zykov, V. S., Brandstädter, H., Gerdes, I. & Engel, H. (2008), ‘Efficient control of spiral wave location in an excitable medium with localized heterogeneities’, *New Journal of Physics* **20**, 015003.
- Schütze, J., Steinbock, O. & Müller, S. C. (1992), ‘Forced vortex interaction and annihilation in an active medium’, *Nature* **356**, 45–47.
- Sendina-Nadal, I., Alonso, S., Pérez-Munuzuri, V., Gómez-Gesteira, M., Pérez-Villar, V., Ramírez-Piscina, L., Casademunt, J., Sancho, J. M. & Sagués, F. (2000), ‘Brownian motion of spiral waves driven by spatiotemporal structured noise’, *Phys. Rev. Lett* **84**(12), 2734–2737.
- Siegert, F. & Weijer, C. (1989), ‘Digital image processing of optical density wave propagation in dictyostelium discoideum and analysis of the effects of caffeine and ammonia’, *J. Cell. Sci.* **93**, 325–335.
- Skinner, G. S. & Swinney, H. L. (1991), ‘Periodic to quasiperiodic transition of chemical spiral rotation’, *Physica D* **48**(1), 1–16.
- Socolar, J. E. S., Sukow, D. W. & Gauthier, D. J. (1994), ‘Stabilizing unstable periodic orbits in fast dynamical systems’, *Phys. Rev. E* **50**(4), 3245–3248.

- Steinbock, O., Zykov, V. & Müller, S. C. (1993), ‘Control of spiral-wave dynamics in active media by periodic modulation of excitability’, *Nature* **366**, 322–324.
- Toiya, M., Vanag, V. K. & Epstein, I. R. (2008), ‘Diffusively coupled chemical oscillators in a microfluidic assembly’, *Angew. Chem. Int. Ed.* **47**, 7753–7755.
- Totz, J. F., Engel, H. & Steinbock, O. (2014), ‘Spatial Confinement Causes Lifetime Enhancement and Expansion of Vortex Rings with Positive Filament Tension’, *ArXiv e-prints* .
- Vanag, V. K., Yang, L., Dolnik, M., Zhabotinsky, A. M. & Epstein, I. R. (2000), ‘Oscillator cluster patterns in a homogeneous chemical system with global feedback’, *Nature* **406**, 389–391.
- Vinson, M., Mironov, S., Mulvey, S. & Pertsov, A. (1997), ‘Control of spatial orientation and lifetime of scroll rings in excitable media’, *Nature* **386**, 477–480.
- Wheeler, P. & Barkley, D. (2006), ‘Computation of spiral spectra’, *SIAM J. Appl. Dyn. Sys.* **5**(1), 157–177.
- Winfree, A. T. (1972), ‘Spiral waves of chemical activity’, *Science* **175**(4022), 634–636.
- Winfree, A. T. (1991), ‘Varieties of spiral wave behavior: An experimentalist’s approach to the theory of excitable media’, *Chaos* **1**(3), 303–334.
- Wu, N., Gao, H., Ma, J. & Ying, H. (2012), ‘Adjustment of spiral wave drift by a travelling wave perturbation’, *Nonlinear Dyn* **67**, 159–164.
- Wu, N. J., Gao, H. J. & Ying, H. P. (2013), ‘Design of the spiral drift by distributing a feedback-related excitability over a small dynamic region’, *EPL* **102**, 40002.
- Zaikin, A. N. & Zhabotinsky, A. M. (1970), ‘Concentration wave propagation in two-dimensional liquid-phase self-oscillating system’, *Nature* **225**, 535–537.
- Zhabotinsky, A. M. & Zaikin, A. N. (1973), ‘Autowave processes in a distributed chemical system.’, *J. Theor. Biol.* **40**, 45–61.
- Zhang, H. & Patel, N. (1995), ‘Spiral wave breakdown in an excitable medium model of cardiac tissue’, *Chaos, Solitons, and Fractals* **5**, 635–639.

- Zykov, S., Zykov, V. S. & Davydov, V. (2006), ‘Spiral wave dynamics under traveling-wave modulation of excitable media’, *Europhys. Lett.* **73**(3), 335–341.
- Zykov, V. S., Bordiougov, G., Brandtstädter, H., Gerdes, I. & Engel, H. (2003), ‘Periodic forcing and feedback control of nonlinear lumped oscillators and meandering spiral waves’, *Phys. Rev. E* **68**, 016214.
- Zykov, V. S., Bordiougov, G., Brandtstädter, H., Gerdes, I. & Engel, H. (2004), ‘Global control of spiralwave dynamics in an excitable domain of circular and elliptical shape’, *Phys. Rev. Lett.* **92**(1), 018304.
- Zykov, V. S. & Engel, H. (2004), ‘Feedback-mediated control of spiral waves’, *Physica D* **199**, 243–263.
- Zykov, V. S., Kheowan, O.-U., Rangsiman, O. & Müller, S. C. (2002), ‘Instabilities of the resonance attractor for spiral waves in an excitable medium’, *Phys. Rev. E* **65**(2), 026206.
- Zykov, V. S., Mikhailov, A. S. & Müller, S. C. (1997), ‘Controlling spiral waves in confined geometries by global feedback’, *Phys. Rev. Lett.* **78**(17), 3398–3401.

Acknowledgements

First of all I would like to thank my supervisor, Prof. Dr. Harald Engel, for giving me the opportunity to work in the interesting field of spiral wave dynamics. Aside from his guidance and continuous support I would especially like to mention his ability to find the right balance between patience on the one hand and on the other, accurate pressure at the right moment. Without this, I probably wouldn't have finished this thesis.

Furthermore I would like to thank all of the current and former members of Prof. Dr. Harald Engel's research group '*Nonlinear Dynamics and Pattern Formation*'. Special thanks go to Dr. Vladimir Zykov for his support, especially in answering my questions regarding the theory of spiral wave dynamics and the vivid collaboration; Ingeborg Gerdes for her willingness to perform a huge part of the experiments; Dr. Hermann Brandtstädter for fruitful discussions regarding the Belousov-Zhabotinsky reaction; Peter Kolski and Anton Smessart for the implementation of the control software for the experiments.

I thank Prof. Dr. Lutz Schimansky-Geier for assessing this thesis within a very short time so that I was able to stick to the date for the defense of this thesis and Prof. Dr. Dieter Breitschwerdt for chairing my thesis committee.

I am very grateful to my wife Susann Schlesner for her constant support and understanding, even in situations where it was quite hard for her. Moreover, I would like to thank my parents, Helga and Manfred Schlesner, for their support and encouragement – not only during my work on this thesis, but in each phase of my life.

I would also like to thank my English teacher Trevor Pichanick for reading and correcting the entire thesis.

This work was supported by Deutsche Forschungsgemeinschaft in the framework of the Sonderforschungsbereich 555 '*Complex Nonlinear Processes*'.